Springer Theses
Recognizing Outstanding Ph.D. Research

Yuki Shiomi

Anomalous and Topological Hall Effects in Itinerant Magnets

Springer

Springer Theses

Recognizing Outstanding Ph.D. Research

For further volumes:
http://www.springer.com/series/8790

Aims and Scope

The series "Springer Theses" brings together a selection of the very best Ph.D. theses from around the world and across the physical sciences. Nominated and endorsed by two recognized specialists, each published volume has been selected for its scientific excellence and the high impact of its contents for the pertinent field of research. For greater accessibility to non-specialists, the published versions include an extended introduction, as well as a foreword by the student's supervisor explaining the special relevance of the work for the field. As a whole, the series will provide a valuable resource both for newcomers to the research fields described, and for other scientists seeking detailed background information on special questions. Finally, it provides an accredited documentation of the valuable contributions made by today's younger generation of scientists.

Theses are accepted into the series by invited nomination only and must fulfill all of the following criteria

- They must be written in good English.
- The topic should fall within the confines of Chemistry, Physics, Earth Sciences, Engineering and related interdisciplinary fields such as Materials, Nanoscience, Chemical Engineering, Complex Systems and Biophysics.
- The work reported in the thesis must represent a significant scientific advance.
- If the thesis includes previously published material, permission to reproduce this must be gained from the respective copyright holder.
- They must have been examined and passed during the 12 months prior to nomination.
- Each thesis should include a foreword by the supervisor outlining the significance of its content.
- The theses should have a clearly defined structure including an introduction accessible to scientists not expert in that particular field.

Yuki Shiomi

Anomalous and Topological Hall Effects in Itinerant Magnets

Doctoral Thesis accepted by
the University of Tokyo, Tokyo, Japan

Springer

Author
Dr. Yuki Shiomi
Department of Applied Physics
The University of Tokyo
Tokyo
Japan

Supervisor
Prof. Yoshinori Tokura
Department of Applied Physics
The University of Tokyo
Tokyo
Japan

ISSN 2190-5053 ISSN 2190-5061 (electronic)
ISBN 978-4-431-54360-2 ISBN 978-4-431-54361-9 (eBook)
DOI 10.1007/978-4-431-54361-9
Springer Tokyo Heidelberg New York Dordrecht London

Library of Congress Control Number: 2013934539

Printed on acid-free paper

Springer is part of Springer Science+Business Media (www.springer.com)

Parts of this thesis have been published in the following journal articles:

1. Section 1 of Chapter 3: "Lorenz Number Determination of the Dissipationless Nature of the Anomalous Hall Effect in Itinerant Ferromagnets" Y. Onose, Y. Shiomi, and Y. Tokura, Phys. Rev. Lett. **100**, 016601 (2008).

2. Section 1 of Chapter 4: "Extrinsic anomalous Hall effect in charge and heat transport in pure iron, $Fe_{0.997}Si_{0.003}$, and $Fe_{0.97}Co_{0.03}$" Y. Shiomi, Y. Onose and Y. Tokura, Phys. Rev. **B 79**, 100404(R) (2009).

3. Section 2 of Chapter 3: "Effect of scattering on intrinsic anomalous Hall effect investigated by Lorenz ratio" (Editor's suggestion), Y. Shiomi, Y. Onose and Y. Tokura, Phys. Rev. **B 81**, 054414 (2010).

4. Section 1 of Chapter 5: "Hall effect of spin-chirality origin in a triangular-lattice helimagnet $Fe_{1.3}Sb$", Y. Shiomi, M. Mochizuki, Y. Kaneko and Y. Tokura, Phys. Rev. Lett. **108**, 056601 (2012).

5. Section 2 of Chapter 5: "Emergence of topological Hall effect from fanlike spin structure as modified by Dzyaloshinsky-Moriya interaction in MnP" (Editor's suggestion), Y. Shiomi, S. Iguchi, and Y. Tokura, Phys. Rev. **B 86**, 180404(R) (2012).

Supervisor's Foreword

The anomalous Hall effect, i.e., the transverse response of current by internal magnetization, was discovered by Edwin Hall in 1881, soon after his discovery of the normal Hall effect induced by a magnetic field. Nevertheless, an accurate theoretical understanding in terms of topology in the momentum space or real space has been attained only in recent years. This new stage in condensed-matter physics is now going to provide a more fertile ground for materials science and spintronic technology than what was anticipated previously. This book summarizes the Ph.D. thesis work by Yuki Shiomi on anomalous and topological Hall effects in itinerant magnets. Versatile new Hall phenomena and the interpretations in terms of modernized theoretical models are described here as precious fruits of his diligent study for six years in our laboratory.

One of the highlights described in this book is the study of the Hall effects induced by a heat current, i.e., the Righi-Leduc and Nernst-Ettingshausen effects. Dr. Shiomi has revealed unique properties of the anomalous and topological Hall effects by combining the measurements with electrical and heat currents. I hope that the contents of this book are useful as well as stimulating for researchers and students who are interested in magnetotransport properties of itinerant magnets.

Tokyo, December 2012 Yoshinori Tokura

Acknowledgments

The present work is a result of my six years of research in the Department of Applied Physics of The University of Tokyo. All of that time I was in a wonderful research environment. I owe a sincere debt of gratitude to many people, especially to Prof. Yoshinori Tokura, Prof. Yoshinori Onose, Prof. Satoshi Iguchi, Dr. Yasujiro Taguchi, Prof. Shintaro Ishiwata, Dr. Yoshio Kaneko, Prof. Masahito Mochizuki, Dr. Shin Miyahara, Dr. Hideaki Sakai, Dr. Takeshi Suzuki, Ms. Akiko Kikkawa, Dr. Jun Fujioka, Dr. Shinichiro Seki, Dr. Masaki Uchida, Mr. Shinichi Kumakura, Mr. Toshiya Ideue, Mr. Naoya Kanazawa, and Mr. Kiyou Shibata, for fruitful discussions and constant support for experiments. I appreciate the helpful comments from Prof. Naoto Nagaosa, Dr. Shigeki Onoda, Prof. Masashi Kawasaki, Prof. Yasuo Endo, Prof. Jun Akimitsu, Prof. Atsutaka Maeda, and Prof. Yukitoshi Motome. Finally, I would like to thank my parents and sister for their kind encouragement.

Contents

Chapter 1
Introduction

Abstract This book presents some results on anomalous Hall effect in itinerant ferromagnets and on topological Hall effect in itinerant helimagnets. In this first chapter, we explain basic concepts and former research which are necessary to understand the following chapters. First, I introduce a brief history of the two effects, and then move on to the detailed explanation on them. At last, the purpose of this book will be described.

Keywords Anomalous Hall effect · Topological Hall effect · Berry phase of electrons · Extrinsic mechanism · Scalar spin chirality

1.1 A Brief History of Anomalous and Topological Hall Effects

In 1879, Edwin Herbert Hall discovered what is now universally known as the Hall effect [1]. Hall found that a magnetic field (H) applied to a metallic wire "presses" the electricity toward one side of the wire [2]. The transverse electric field that he discovered (E_y) was proportional to the product of the primary current density (j) and the magnetic flux (B) normal to the plane containing j and E_H. For a set of rectangular coordinate axes with E_H along the y-direction, we can write

$$E_H = Rj_x B_z, \tag{1.1}$$

where R is called the Hall coefficient. Since the transverse force $-eE_H$ acting on any electron equals the Lorentz force $-ev_x B_z$, we obtain the well-known relation $R = 1/n_c(-e)$, where n_c is the density of carriers.

One year later, he reported that the Hall effect was about ten times larger in iron foil than that of gold or silver [3]. This stronger effect in ferromagnetic conductors came to be known as the anomalous Hall effect (AHE). In his third publication [4], he studied nickel and cobalt. He describes a general characteristic of Hall effect in

Y. Shiomi, *Anomalous and Topological Hall Effects in Itinerant Magnets*,
Springer Theses, DOI: 10.1007/978-4-431-54361-9_1, © Springer Japan 2013

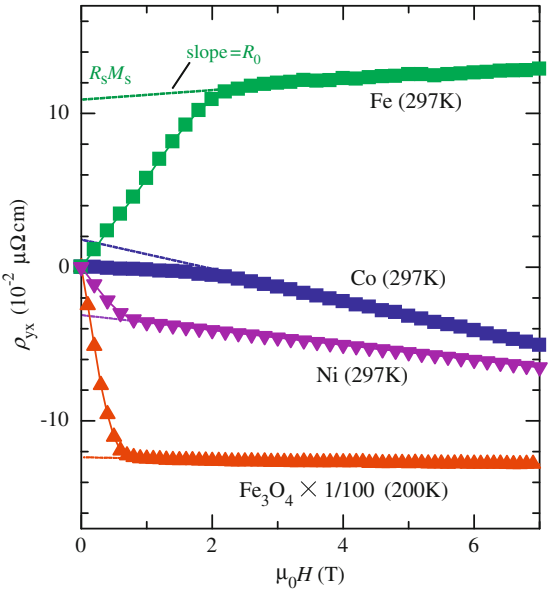

Fig. 1.1 Graphical determination of the two Hall coefficients R_0 and R_s of ferromagnets

ferromagnets: the Hall voltage is not proportional to B. In Fig. 1.1, we show the Hall resistivity $\rho_{yx} = E_H/j_x$ for some ferromagnets.

In 1929, Smith and Sears proposed the relation for the Hall effect observed in the ferromagnets [5]:

$$\rho_{yx} = R_0(\mu_0 H) + R_s M. \tag{1.2}$$

The anomalous Hall coefficient R_s is usually at least one order of magnitude larger than the normal Hall coefficient R_0. The R_0 and R_s values are determined respectively by the slope of ρ_{yx} versus H above ferromagnetic saturation and by the extrapolated value of ρ_{yx} to zero field (Fig. 1.1).

To understand the microscopic origin of AHE has been an enigmatic problem that has resisted theoretical and experimental assaults for almost a century [6]. Since AHE depends on the magnetization (M), i.e. electron spin, and since this spin must influence transport process, the spin-orbit interaction should be involved. The microscopic origins of AHE fall into two classes by the difference in the types of spin-orbit coupling (Fig. 1.2). In a band model (intrinsic model), the coupling is the intrinsic interaction between an itinerant electron's spin $\boldsymbol{s}$ and its angular momentum $\boldsymbol{L}$. On the other hand, in a localized model (extrinsic model), it is the extrinsic interaction between an ion's total angular momentum $\boldsymbol{\sigma}$ and the scattered electron's orbital momentum $\boldsymbol{L}$. Which mechanism makes a major contribution to AHE has been a controversial subject. Up to around 2000, many researchers believed that AHE is mainly caused by the extrinsic mechanisms, since electron scattering would be important in transport phenomena in metallic system.

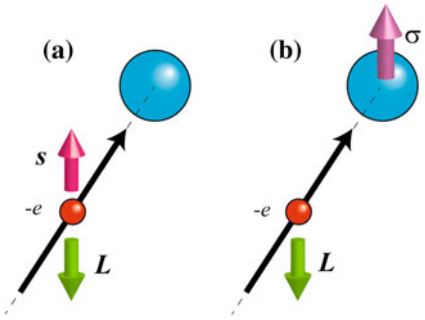

Fig. 1.2 Two types of spin-orbit coupling for an electron of charge $-e$ scattered by an ion of charge ze. **a** Intrinsic mechanism $\boldsymbol{s} \cdot \boldsymbol{L}$. **b** Extrinsic mechanism $\boldsymbol{\sigma} \cdot \boldsymbol{L}$

In the 1980s, the quantum Hall effect was discovered in semiconductor heterostructures [7]. Both the integer and fractional quantum Hall effects can be explained in terms of the topological properties of the electronic wave functions. This concept based on topology began to have a great impact on the controversy on the origin of AHE starting around 1998 [6]. The intrinsic mechanism was reconstructed by the concept of Berry phase. Actualy, the intrinsic contribution can be regarded as an "unquantized" version of the quantum Hall effect [8]. Many recent studies, both theoretical and experimental, have shown the prevailing contribution of the intrinsic mechanism to AHE in ferromagnetic conductors. The excellent agreement between theory and experiments has been demonstrated, for example, in Fe [9] and $SrRuO_3$ [10], which may leave little room for the skew-scattering and side-jump mechanisms.

An important implication by the Berrry-phase scenario is that the anomalous Hall current is dissipationless. Experimentally, the Hall effect measurement in $CuCr_2Se_{4-x}Br_x$ supports this prediction [11]. When x is varied without degrading M, the resistivity changes by several decades but the Hall current divided by the applied electric field (normalized per carrier) remains unchanged throughout [11].

The Berry curvature associated with noncoplanar spin configurations, the scalar spin chirality, was first considered in theories of high-temperature superconductors [12] but became widely known in the context of the Hall effect after 1999 [13]. The spatial variation in local spin textures, which is sometimes driven thermally, by geometrical frustration or by Dzyaloshinsky-Moriya interaction, gives rise to the Berry curvature proportional to the scalar spin chirality $\chi_{ijk} = \boldsymbol{S}_i \cdot (\boldsymbol{S}_j \times \boldsymbol{S}_k)$. The scalar spin chirality is odd under time reversal and even under spatial inversion. Thus, when the spin configuration is noncoplanar, the scalar spin chirality becomes nonzero and could give rise to the Hall effect [13]. Unlike the AHE, this mechanism does not always require the spin-orbit coupling. The Hall effect of this mechanism is sometimes called "topological Hall effect" (THE) in distinction from AHE. Now, they have known several examples in which THE occurs.

While the recent success in the application of Berry-phase scenario to Hall effect is brilliant, it has been pointed out that the extrinsic mechanism is also important in some cases [14, 15]. Especially for the highly conductive metals, it has been shown

theoretically [14] as well as experimentally [16] that the skew-scattering mechanism makes a major contribution compared to the intrinsic one. On the other hand, the side-jump mechanism is still surrounded by a mystery. Although the separation of the side-jump term from the intrinsic one by dc Hall measurement is almost impossible [6], a theory has suggested its finite contribution by calculation for simple models [15], which is not, however, immediately linked to real materials.

1.2 Anomalous Hall Effect in Itinerant Ferromagnets

At the early stages of research, it was already recognized by many experiments that the anomalous Hall resistivity (ρ_{yx}^{A}) depends on the longitudinal resistivity (ρ_{xx}) such as $\rho_{yx}^{A} \propto (\rho_{xx})^{n}$. This gave the impression that AHE is somehow connected with electron scattering.

Up to now, three mechanisms of AHE have been recognized. Two of three contributions arise due to scattering (extrinsic mechanism): (i) the skew scattering that refers to the asymmetric scattering amplitude with respect to the scattering angle between the incoming and outgoing electron waves and (ii) the side jump which is a sudden shift of the electron coordinates during scattering. The other is intrinsic mechanism, which is intrinsically independent of the scattering and comes from the Berry phase of Bloch electrons.

The anomalous Hall conductivity from these contributions are expressed by

$$\sigma_{xy}^{A} = \sigma_{xy}^{\mathrm{int}} + \sigma_{xy}^{\mathrm{skew}} + \sigma_{xy}^{\mathrm{side-jump}}, \tag{1.3}$$

where $\sigma_{xy}^{\mathrm{int}}$ is the intrinsic contribution which is independent of the relaxation time τ, $\sigma_{xy}^{\mathrm{skew}}$ is the skew scattering contribution which is proportional to τ, and $\sigma_{xy}^{\mathrm{side-jump}}$ is the side jump contribution which is independent of τ.

An important question is how to identify the dominant contribution to AHE among these mechanisms. A theory was developed by Luttinger [17] in 1958, assuming elastic scattering by impurities. If n is obtained to be larger than 1, the theory must go beyond a classical Boltzmann equation. In a quantum transport equation, the classical electron distribution f_k in the $\boldsymbol{k}$-space is replaced by a density matrix $f_{kk'}$. The calculated Hall resistivity is expressed as [17]

$$\rho_{yx}^{A} = a\rho_{xx} + b\rho_{xx}^{2}, \tag{1.4}$$

where a and b are constants. The first term is classical (skew scattering), but the second one is considered to be a quantum effect such as the intrinsic mechanism or side jump.

A unified theory without side-jump contribution was recently presented [14, 18] in terms of a fully quantum-mechanical transport theory for multiband systems with the self-consistent T-matrix approximation. They clarified that a crossover occurs as

a function of the scattering strength ($\hbar/\tau$) from a region where the skew-scattering mechanism is predominant to that where the intrinsic one becomes primary. (i) In the superclean case with the relaxation rate $\hbar/\tau \lesssim u_{imp} E_{SO} D$, the skew scattering yields a dominant contribution that is inversely proportional to n_{imp}, where u_{imp} is the impurity potential strength and D is the density of states. With increasing $\hbar/\tau$, this extrinsic skew-scattering contribution rapidly decays. (ii) In the moderately dirty regime $u_{imp} E_{SO} D \lesssim \hbar/\tau \lesssim E_F$, the Hall conductivity becomes insensitive to the scattering strength because of the intrinsic dissipationless contribution. Further increasing $\hbar/\tau$ ($2\varepsilon_F \lesssim \hbar/\tau$), another crossover occurs to (iii) the scaling regime of $\sigma_{xy}^A \propto \sigma_{xx}^{1.6}$, where the Hall conductivity decays with the disorder due to the influence of finite-lifetime disorder broadening on $\sigma_{xy}^{\rm int}$. Very recent work [19] has also predicted $\sigma_{xy}^A \sim \sigma_{xx}^{\gamma}$ ($1.33 \leq \gamma \leq 1.76$) in the insulating regime by the phonon-assisted hopping mechanism and percolation theory. This region is sometimes referred to as the "incoherent regime". It is important to note here that the above theory is based on elastic scattering and cannot apply to temperature dependence of σ_{xy}^A. The three distinct regimes have been confirned by many experiments [11, 16, 20–34] as shown in Fig. 1.3. Because of the well correspondence between the theory and experiments,

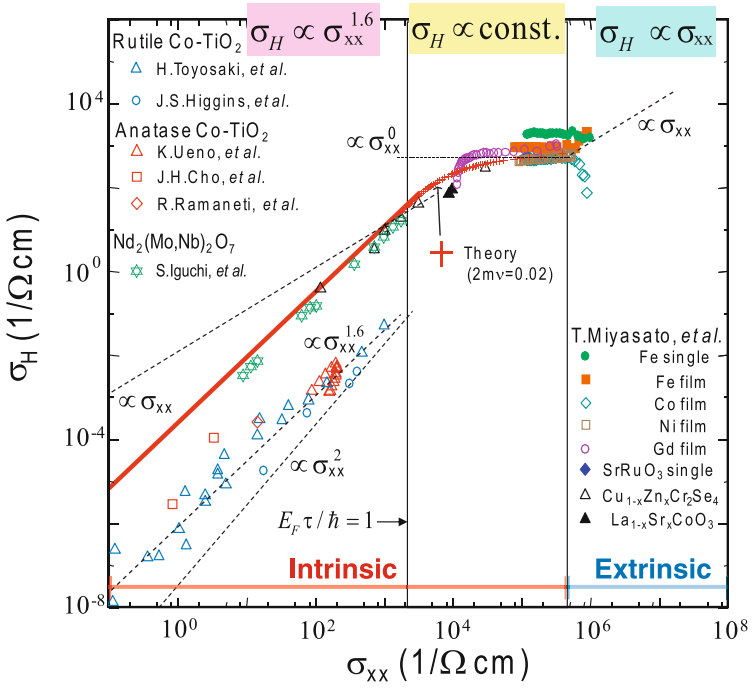

Fig. 1.3 The scaling law between σ_{xx} and σ_{xy}^A [18], in which the experimental results were taken from [16, 20–25]. The *dashed lines* are guides for the eyes. Reproduced with permission from American Physical Society

the side-jump contribution has been considered to be much smaller than intrinsic one [14], while a recent theoretical study has pointed out a possibility of its unignorable contribution [15].

1.2.1 Intrinsic Mechanism

The contribution of the intrinsic mechanism to the AHE was first derived by Karplus and Luttinger [35]. They showed that when an external electric field is applied to a solid, electrons acquire an additional contribution to their group velocity. This "anomalous velocity" was perpendicular to the electric field and therefore could contribute to Hall effect. In the case of ferromagnetic conductors, the sum of the anomalous velocity over all occupied band states can be non-zero. The contribution to the Hall effect depends only on the band structure and is largely independent of scattering. The intrinsic AHE yields a contribution to $\rho_{yx} \simeq \sigma_{xy}/\sigma_{xx}^2 \propto \rho_{xx}^2$.

The topological nature of the intrinsic mechanism has been appreciated recently [36, 37]. The intrinsic contribution to the Hall conductivity can be calculated from the Kubo formula [6]:

$$\sigma_{xy}^A = e^2\hbar \sum_{n\neq n'} \int \frac{d\boldsymbol{k}}{(2\pi)^2} [f(\varepsilon_n(\boldsymbol{k})) - f(\varepsilon_{n'}(\boldsymbol{k}))] \,\mathrm{Im} \frac{\langle n, \boldsymbol{k}|v_x(\boldsymbol{k})|n', \boldsymbol{k}\rangle \langle n', \boldsymbol{k}|v_y(\boldsymbol{k})|n, \boldsymbol{k}\rangle}{(\varepsilon_n(\boldsymbol{k}) - \varepsilon_{n'}(\boldsymbol{k}))^2}, \tag{1.5}$$

where the velocity operator $\boldsymbol{v}(\boldsymbol{k})$ is defined using $\boldsymbol{k}$-dependent Hamiltonian $[H(\boldsymbol{k})]$ by

$$\boldsymbol{v}(\boldsymbol{k}) = \frac{1}{i\hbar}[\boldsymbol{r}, H(\boldsymbol{k})] = \frac{1}{\hbar}\nabla_k H(\boldsymbol{k}). \tag{1.6}$$

Equation (1.5) reduces to the simple form in terms of the Berry curvarture of each occupied band:

$$\sigma_{xy}^A = -\frac{e^2}{\hbar} \sum_n \int \frac{d\boldsymbol{k}}{(2\pi)^3} f(\varepsilon_n(\boldsymbol{k})) b_n^z(\boldsymbol{k}), \tag{1.7}$$

where $\boldsymbol{a}_n(\boldsymbol{k})$ is the Berry-phase connection $\boldsymbol{a}_n(\boldsymbol{k}) = i\langle n, \boldsymbol{k}|\nabla_k|n, \boldsymbol{k}\rangle$, and $\boldsymbol{b}_n(\boldsymbol{k})$ is the Berry-phase curvature

$$\boldsymbol{b}_n(\boldsymbol{k}) = \nabla_k \times \boldsymbol{a}_n(\boldsymbol{k}) \tag{1.8}$$

corresponding to the states $\{|n, \boldsymbol{k}\rangle\}$. The same result can be obtained from the semi-classical theory of wave-packets dynamics. The change in the phase of Bloch state wavepackets caused by an applied electric field generates an additional contribution to the transverse velocity [38, 39].

The intrinsic contribution can be evaluated accurately by means of first-principles electronic structure theory. The Berry curvature was calculated for bcc Fe on the Fermi surface in (010) plane [9]. The Berry curvature shows a very large value at $\boldsymbol{k}$ points with the small energy gap, because it depends on the energy gap in

proportion to $1/\Delta\varepsilon_{nn'}^2$ (see Eq. 1.5). Thus, such $\boldsymbol{k}$ points account for most of the Hall conductivity. The obtained value of σ_{xy}^A is 751 $\Omega^{-1}\mathrm{cm}^{-1}$, which is in fair agreement with the experimental value (500–1000 $\Omega^{-1}\mathrm{cm}^{-1}$).

$\boldsymbol{b}_n(\boldsymbol{k})$ is regarded as "fictitious" magnetic flux acting on electrons with the state $|n, \boldsymbol{k}\rangle$. In the presence of an electric field, an electron can acquire an anomalous velocity proportional to the Berry curvature of the band [38, 39]. The formula for the velocity in a given state $\boldsymbol{k}$ becomes

$$\boldsymbol{v}_n(\boldsymbol{k}) = \frac{1}{\hbar}\frac{\partial\varepsilon_n(\boldsymbol{k})}{\partial\boldsymbol{k}} - \frac{e}{\hbar}\boldsymbol{E}\times\boldsymbol{b}_n(\boldsymbol{k}). \tag{1.9}$$

The second term, anomalous velocity, is always transverse to the electric field, which gives rise to the anomalous Hall current. The velocity formula reveals that the Berry curvature is also required for a complete description of the electron dynamics. However, the conventional formula without the anomalous velocity has succeeded in describing many electronic properties in the past. Actually, for crystals with simultaneous time-reversal and spatial inversion symmetry the Berry curvature vanishes identically throughout the Brillouin zone [6]. The velocity formula should be invariant under time-reversal and spatial inversion operations if the unperturbed system has these symmetries. Under time reversal, $\boldsymbol{v}_n(\boldsymbol{k})$ and $\boldsymbol{k}$ change sign while $\boldsymbol{E}$ is fixed, i.e.

$$\boldsymbol{b}_n(-\boldsymbol{k}) = -\boldsymbol{b}_n(\boldsymbol{k}). \tag{1.10}$$

Under spatial inversion, $\boldsymbol{v}_n$, $\boldsymbol{k}$, and $\boldsymbol{E}$ change sign, i.e.

$$\boldsymbol{b}_n(-\boldsymbol{k}) = \boldsymbol{b}_n(\boldsymbol{k}). \tag{1.11}$$

Therefore, in case that the time-reversal and spatial inversion symmetries are simultaneously are protected, the Berry curvature is zero. In the presence of the magnetic order, on the other hand, the time-reversal symmetry is broken and then the Berry curvature becomes nonzero as shown for ferromagnetic Fe [9]. In the presence of electromagnetic field (not only $\boldsymbol{E}$ but $\boldsymbol{B}$), the generalized equations of motions are summarized as follows [8]:

$$\dot{\boldsymbol{r}} = \frac{1}{\hbar}\frac{\partial\varepsilon_n(\boldsymbol{k})}{\partial\boldsymbol{k}} - \dot{\boldsymbol{k}}\times\boldsymbol{b}_n(\boldsymbol{k}) \tag{1.12}$$

$$\hbar\dot{\boldsymbol{k}} = e\frac{\partial\phi(\boldsymbol{r})}{\partial\boldsymbol{r}} - e\dot{\boldsymbol{r}}\times\boldsymbol{B}, \tag{1.13}$$

where $\phi(\boldsymbol{r})$ is a scalar potential ($\nabla_{\boldsymbol{r}}\phi(\boldsymbol{r}) = -\boldsymbol{E}$).

A topological number, the Chern number Ch_n for each band n, is linked with AHE. The Chern number for each band n in two-dimensional ferromagnet is defined by [37]

$$Ch_n = \sum_{\boldsymbol{k}\in 1\text{st BZ}} 2\pi[\boldsymbol{b}_n(\boldsymbol{k})]_z \tag{1.14}$$

or

$$Ch_n = \frac{1}{2\pi}\int_{1\text{st BZ}} d\boldsymbol{k}[\boldsymbol{b}_n(\boldsymbol{k})]_z. \tag{1.15}$$

For example, for 6 energy bands of t_{2g} orbitals [37], the Ch_n values are calculated to be -1, -2, 3, -4, 5, and -1 from the lowest to highest energy bands. Namely, the spin-orbit interaction gives the nontrivial topological structure to the Bloch bands in the ferromagnets, as in the case of the quantum Hall effect. At the band crossing point gapped by spin-ornit interaction, the Chern number is transferred by $\pm 1/2$, which generates the Hall conductivity $\pm e^2/2h$.

From another point of view, the band crossing points which largely contribute to AHE are regarded as monopoles in $\boldsymbol{k}$ space [10]. Consider the general case where two band Hamiltonian matrix $H(\boldsymbol{k})$ at $\boldsymbol{k}$ can be written as

$$H(\boldsymbol{k}) = \sum_{\mu=0,1,2,3} f_\mu(\boldsymbol{k})\sigma_\mu, \tag{1.16}$$

where $\sigma_{1,2,3}$ are the Pauli matrices and σ_0 is the unit matrix. Then we can consider the mapping from $\boldsymbol{k}$ to the vector

$$\boldsymbol{f}(\boldsymbol{k}) = (f_1(\boldsymbol{k}), f_2(\boldsymbol{k}), f_3(\boldsymbol{k})) = f(\boldsymbol{k})(\cos\varphi_f \sin\theta_f, \sin\varphi_f \sin\theta_f, \cos\theta_f). \tag{1.17}$$

Then $H(\boldsymbol{k})$ can be easily diagonalized to obtain the two eigenvalues $\varepsilon_\pm(\boldsymbol{k}) = f_0(\boldsymbol{k}) \pm f(\boldsymbol{k})$. In this case, the σ_{xy} is reduced to

$$\sigma_{xy}^{2-\text{bands}} = \frac{e^2}{8\pi h}\int dk_z d\Omega_f [f_{FD}(\varepsilon_-(\boldsymbol{k})) - f_{FD}(\varepsilon_+(\boldsymbol{k}))], \tag{1.18}$$

where $f_{FD}(\varepsilon)$ is the Fermi distribution function. Here $d\Omega_f$ is the $\boldsymbol{f}$-space solid angle, which is the integral of the gauge field

$$\boldsymbol{b}(\boldsymbol{f}) = \pm\frac{\boldsymbol{f}}{|\boldsymbol{f}|^3} \tag{1.19}$$

due to the monopole at $\boldsymbol{f} = \boldsymbol{0}$ over the infinitesimal surface in $\boldsymbol{f}$-space corresponding to the small square $dk_x dk_y$ in $\boldsymbol{k}$-space [10]. This gauge field strongly depends on $\boldsymbol{k}$ in the near degeneracy case, i.e. when $\boldsymbol{f}(\boldsymbol{k})$ is near the monopole.

1.2.2 Extrinsic Mechanism

Let us consider an electron wavepacket approaching a central scattering potential (Fig. 1.4). Before scattering, the center of mass of the packet moves in a straight line thorough the periodic crystal. After scattering, the wavepacket is broken into a set of

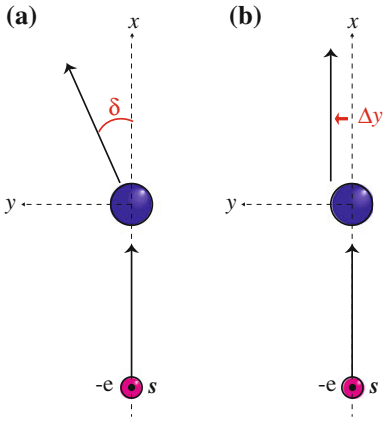

Fig. 1.4 The trajectory of a wavepacket for **a** skew scattering and **b** side jump. **a** After the scattering, the average trajectory of the electron is deflected by a spin-dependent angle δ. δ is typically of order 10^{-2} rad [44]. **b** The center of the wave-packet is displaced laterally during the scattering. The lateral displacement Δy is about 10^{-11} m

outgoing spherical waves. The motion of the center of mass again follows a straight line at a constant speed.

If the electron spin $\boldsymbol{s}$ is normal to the plane of the illustration, spin-orbit interaction removes any symmetry between right and left. As a result, the trajectory after scattering may well differ from the one before scattering.

For example, the new trajectory might be at an angle to the old one (Fig. 1.4a). This means that the electron acquires transverse momentum on scattering. The effect is called "skew scattering". It can be derived from a classical Boltzmann equation if the differential cross-section has a left-right asymmetry. However, it vanishes in the first Born approximation, i.e. for weak scatterers. To obtain the skew-scattering contribution, we proceed to second order approximation. In the relation of $\rho_{yx}^{A} \propto (\rho_{xx})^{n}$, it gives $n = 1$. Skew scattering was proposed by Smit [40, 41].

A second possibility is that the new trajectory might be displaced by a finite distance from the old trajectory (Fig. 1.4b). This transverse displacement Δy is called a "side jump" [42, 43]. The Δy was estimated to be $\sim 10^{-11} - 10^{-10}$ m, which may be large enough to yield AHE observed in ferromagnets. Surprisingly, the side-jump Δy per collision is found to be independent of the strength, range, or sign of the scattering potential. The side jump mechanism predicts $n = 2$ in $\rho_{yx}^{A} \propto (\rho_{xx})^{n}$. An intuitive picture of side-jump mechanism was presented in [44].

1.2.2.1 Remarks on Skew Scattering

The original theory by Smit [40, 41] considered free electrons and short-range potentials. A spin-orbit interaction is added to the scattering potential $V(\boldsymbol{r})$:

$$H_{SO} = -\lambda_{SO}(\boldsymbol{k} \times \boldsymbol{s}) \cdot \nabla V. \tag{1.20}$$

For $3d$ band electrons, the coupling parameter is taken as

$$\lambda_{SO}(\varepsilon_F) = A_{SO}\chi d^2 \sum_n \frac{|\text{matrix el.}|}{\varepsilon_n - \varepsilon_F} \tag{1.21}$$

(Fivaz effective spin-orbit hamiltonian), where d is the distance between nearest-neighbor atoms, and ε_n is the energy of a band state, $\chi \sim 0.1$ is overlap integral between nearest-neighbor atomic $3d$ states, and $A_{SO} = 0.1$ eV is the atomic spin-orbit parameter for $3d$ electrons. Since the sign of the skew-scattering contribution changes when that of the scattering potential is reversed, and since phonons can be represented by a potential of fluctuating sign, skew scattering by phonons is probably very small.

In 1972, Fert and Jaoul [45] proposed a different theory based on the Anderson model, where free (or s) electrons are scattered into other free-electron states through an intermediate resonant $3d$ state bound to the scattering potential. This s-d-s scattering model is very appropriate for dilute transition-metal impurities dissolved in a noble metal. It may even apply to dilute impurities in iron, nickel, and cobalt, since conduction by high-mobility $4s$ electrons is probably dominant. It cannot, by contrast, apply to weak scattering potentials, for which $3d$ resonances are absent.

In the case of localized $4f$ states in dilute rare-earth impurities dissolved in a noble metal, orbital angular momentum is not appreciably quenched. Skew scattering of such a case was studied by Fert and Friederich for rare-earth in silver and gold [46]. The Hall coefficient was composed of the normal Hall one and skew-scattering one which is proportional $1/T$. They fitted the Hall coefficient R to an expression of the form

$$R = R_0 + a\frac{\rho_0}{T}. \tag{1.22}$$

a characterizes the skew scattering by a rare-earth element. Fert and Friederich [46] investigated the variation of the skew scattering coefficient a through the rare-earth series in silver- and gold-based alloys. In both cases, the variation of a is almost consistent with the theoretical curve of the form

$$a = \alpha_1(2-g)gJ(J+1) + \alpha_2(g-1)gJ(J+1), \tag{1.23}$$

where J is the total angular momentum and g is the gyromagnetic factor of the $4f$ electrons. In these alloys, a $5d$ virtual bound state i.e. the admixture of $5d$ states into the conduction states, is formed. The first term is orbital exchange term between $4f$ electrons and conduction electron arising from the $5d$ admixture. If the spin-orbit splitting of the $5d$ virtual bound state is taken into account, the $4f$-$5d$ spin exchange gives rise to the second term [2].

Naively, one would expect skew scattering to play no role in the Hall effect of very pure metals, since very few scatterers are present. As described before, however, this speculation has turned out to be incorrect according to the recent studies [14, 16, 18].

1.2.2.2 Remarks on Side Jump

By the calculation in which the spin-orbit energy is added to a potential $V(\boldsymbol{r})$, one obtains, using the first Born approximation, the side jump per collision [44, 47, 48]

$$\Delta y = -\lambda_{SO} s_z k_x \tag{1.24}$$

where $s_z = \pm 1/2$ is the spin of the itinerant electron. In the case of $3d$ band electrons, it gives $\Delta y \sim 10^{-11}$–10^{-10} m. As mentioned before, the side jump per collision is predicted to be independent of the strength, range, or sign of $V(\boldsymbol{r})$. Thus, the induced Hall resistivity is pretty much the same for phonon, impurity, or magnon scattering in the original theory presented by Berger [42, 43]. On the other hand, the side-jump contribution depends on the band structure of the metal, and on the location of the Fermi level ε_F in these bands, through the effective spin-orbit parameter $\lambda_{SO}(\varepsilon_F)$ in Eq. (1.21). This was considered to explain the variation of AHE as a function of composition in series of transition-metal alloys.

In the case of normal Hall effect as well as the skew-scattering-induced AHE, the contribution of each band is weighted according to the mobility of its electrons. As a result, high-mobility $4s$ electrons tend to give a dominant contribution. However, one can show that there are no such weight factors in the case of the side-jump mechanism [2]. Thus, low-mobility $3d$ electrons which undergo frequent collisions contribute as much or more as $4s$ electrons. The low degree of spin polarization of the $4s$ electrons further decreases their contribution.

Recently, several other scattering processes have been identified as side-jump mechanism besides Berger's original one [49]. In the case that all the scattering processes are included, it has been shown that the side jump mechanism sensitively depends on the symmetry property of the scattering [50]. They have proposed the following three classes of scattering: nonmagnetic impurity scattering and phonon scattering (class A); the scattering by magnetic impurity with spin directions oriented along the average magnetization (class B); and the scattering by magnetic impurity with random in-plane magnetic orientation, by electrons, and by magnons (class C). Since the s_z in Eq. (1.24) is affected differently in each scattering class, the three classes of scattering generate different contributions and compete each other.

At last, I present some of recent experimental attempts to separate the side-jump contribution from the intrinsic one, although it is basically so difficult since they predict the same ρ_{xx}-dependence of ρ_{yx}^A ($\rho_{yx}^A \propto \rho_{xx}^2$). In Fe films [51], the side-jump contribution was experimentally separated by assuming that the side-jump contribution is caused by the impurity scattering, i.e. $\rho_{yx} = \alpha\rho_0 + \beta{\rho_0}^2 + b\rho_{xx}^2$, where the first, second, and third terms are skew-scattering, side-jump, and intrinsic contributions, respectively. The estimated side-jump term is $\sim 500\,\Omega^{-1}\mathrm{cm}^{-1}$, which is as large as the intrinsic one. The comparable magnitude of side jump contribution has been reported for thin films of FePd and FePt alloys [52]. They estimated the intrinsic contribution by the theoretical calculation of the electronic structure, and determined the side-jump term by the subtraction of it from the term proportional to ρ_{xx}^2 in observed ρ_{yx}^A. Very recently, a theoretical estimation of the side-jump contribution has been

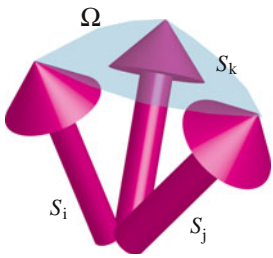

Fig. 1.5 Noncoplanar spin texture ($\boldsymbol{S}_i$, $\boldsymbol{S}_j$, and $\boldsymbol{S}_k$) and scalar spin chirality ($\propto \Omega$)

reported based on first-principles calculation for perfect crystals of bcc Fe, hcp Co, fcc Ni, and $L1_0$ FePd and FePt alloys [15].

1.3 Topological Hall Effect

1.3.1 Scalar Spin Chirality

A nontrivial spin texture also drives a Hall effect. To distinguish this mechanism from AHE due to the spin-orbit interaction, it is often referred to as "topological Hall effect" (THE) [53].

A key notion for the origin of THE is scalar spin chirality $\boldsymbol{S}_i \cdot (\boldsymbol{S}_j \times \boldsymbol{S}_k)$ defined on local three spins $\boldsymbol{S}_i$, $\boldsymbol{S}_j$, and $\boldsymbol{S}_k$ (Fig. 1.5). This scalar product corresponds to the solid angle Ω subtended by the three spins on the unit sphere, when the solid angle Ω is much smaller than 4π; for example, when the three spins lie in the plane of the equator, the scalar spin chirality is zero, while the solid angle is 2π. Obviously, it is zero in case that the three spins are coplanar. As discussed later, the noncoplanar spin configuration is connected to the Berry curvature and generates fictitious magnetic flux proportional to the scalar spin chirality, as the spin-orbit interaction does in ferromagnetic conductors.

The theoretical models of THE have been classified into strong coupling and weak coupling cases by the strength of s-d coupling. The strong coupling model was first presented by Ye et al. [13]. In order to explain the Hall effect observed in CMR manganites [54], they proposed a model of $3D$ ferromagnet with thermally excited Skyrmion strings (topological dipoles) and showed that a THE can be induced by the Berry phase related to the spatial variation of magnetization in the vicinity of the string [13]. Perovskite-type manganese oxides which show colossal magnetoresistance effect (CMR) has been explained by the double-exchange model [13]

$$H = -\sum_{i,j,\alpha} t_{ij}(c^{\dagger}_{i\alpha} + h.c.) - J_H \sum_i \boldsymbol{S}_i \cdot c^{\dagger}_{i\alpha}\boldsymbol{\sigma}_{\alpha\beta}c_{i\beta} \tag{1.25}$$

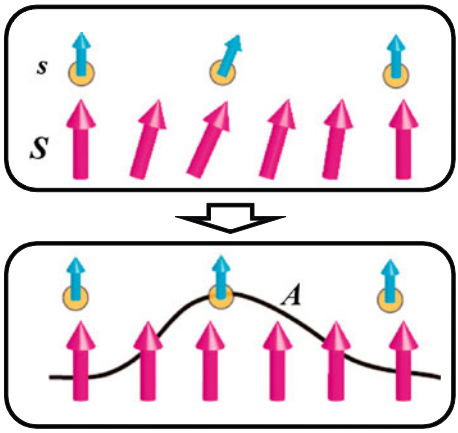

Fig. 1.6 Conduction electron and spatially varying spin texture. By gauge transformation, the conduction electrons are interpreted to interact with the gauge field $\boldsymbol{A}$

where J_H is the ferromagnetic Hund's coupling between the spin $\boldsymbol{\sigma}$ of the conduction electrons in e_g-orbitals and the localized spins $\boldsymbol{S}_i$ in t_{2g}-orbitals. In the limit of large J_H (strong coupling), the conduction electron spin $\boldsymbol{s}$ is forced to align with $\boldsymbol{S}_i$ at each site. In this case, the perturbative approach is not valid. Rather, we should discuss the spatial variation of the spin direction in terms of the gauge field. By a gauge transformation which makes the quantization axis oriented along vector $\boldsymbol{n}(\boldsymbol{r})$ at each point, the transformed Hamiltonian describes the electrons polarized along a uniform direction and moving in an SU(2) gauge potential (Fig. 1.6). This gauge potential couples to the electric charge and induces THE [55]. For CMR manganites, the THE occurs in the presence of the spin-orbit interaction [13] and the calculated T-dependence is well consistent with the experimental results [54].

The case in weak coupling has been discussed in [56] by a perturbative calculation. This weak coupling model has explained well the Hall effect observed in canonical spin glass systems. When the conduction electrons are only weakly coupled to the local spin, we take into account the s-d exchange coupling perturbatively [56]. We consider the Hamiltonian given by

$$H = \sum_{\boldsymbol{k},\sigma} \varepsilon_{\boldsymbol{k}\sigma} c^{\dagger}_{\boldsymbol{k}\sigma} c_{\boldsymbol{k}\sigma} + \frac{J}{N} \sum_{\boldsymbol{k}\boldsymbol{k}'} \boldsymbol{S}_{\boldsymbol{k}'-\boldsymbol{k}} (c^{\dagger}_{\boldsymbol{k}'} \boldsymbol{\sigma} c_{\boldsymbol{k}}) + \frac{v_{imp}}{N} \sum_{i,n_{imp}} e^{i(\boldsymbol{k}-\boldsymbol{k}')X_i} c^{\dagger}_{\boldsymbol{k}'} c_{\boldsymbol{k}}, \quad (1.26)$$

where $\sigma = \pm$ and $\boldsymbol{S}$ denote electron and localized spins, respectively. Electron energy is $\varepsilon_{\boldsymbol{k}\sigma} = \boldsymbol{k}^2/2m - \sigma\Delta - \varepsilon_F$, where Δ is a uniform polarization of conduction electron due to magnetization or external magnetic field. In the second term of Eq. (1.26), $\boldsymbol{\sigma} = (\sigma^x, \sigma^y, \sigma^z)$ denotes Pauli matrices, N is the total number of lattice sites, and J is the exchange coupling. The third term represents the scattering by nonmagnetic impurities (constant v_{imp}) at sites X_i. By perturbation calculation with respect to the second term (the interaction between conduction electrons and the localized spins), σ_{xy} is calculated. In the case that the polarization of conduction electron is small

($\Delta \sim 0$), the Hall conductivity is

$$\sigma_{xy}^{(3)} = \frac{N}{\pi V}\left(\frac{e}{m}\right)^2 (2\pi\nu J)^3\tau^2\chi_0 = 16\pi^2\sigma_0 J^3\nu^2\tau\chi_0, \tag{1.27}$$

where ν is the density of states per site and σ_0 is the Boltzmann conductivity, $\sigma_0 \equiv \frac{N}{2V}\left(\frac{e}{m}\right)^2 \nu k_B^2\tau$. We note that $\sigma_{xy}^{(3)} \propto \tau^2$ i.e. $\rho_{yx}^{(3)}$ is independent of τ. The uniform scalar spin chirality χ_0 is given by

$$\chi_0 \equiv \frac{1}{6N}\sum_{\boldsymbol{X}_i} \boldsymbol{S}_{\boldsymbol{X}_1}\cdot(\boldsymbol{S}_{\boldsymbol{X}_2}\times\boldsymbol{S}_{\boldsymbol{X}_3}) \tag{1.28}$$

$$\times\left[\frac{(\boldsymbol{a}\times\boldsymbol{b})_z}{ab}I'(a)I'(b)I(c) + \frac{(\boldsymbol{b}\times\boldsymbol{c})_z}{bc}I(a)I'(b)I'(c) + \frac{(\boldsymbol{c}\times\boldsymbol{a})_z}{ca}I'(a)I(b)I'(c)\right], \tag{1.29}$$

where $\boldsymbol{X}_i$ runs over all the positions of local spins. $\boldsymbol{a} = \boldsymbol{X}_1 - \boldsymbol{X}_2$, $\boldsymbol{b} = \boldsymbol{X}_2 - \boldsymbol{X}_3$, and $\boldsymbol{c} = \boldsymbol{X}_3 - \boldsymbol{X}_1$ are the vectors representing sides of the triangle. $I(r) = 1/(2\pi N\nu\tau)\sum_{\boldsymbol{k}} e^{i\boldsymbol{k}\cdot\boldsymbol{r}}G_{\boldsymbol{k}}^R G_{\boldsymbol{k}}^A$ and $I'(r) = \frac{\mathrm{d}I(r)}{\mathrm{d}r}$. The Hall current is driven by three spins which form a finite solid angle in spin space spanning a finite area in coordinate space. Since $I(r)$ is reduced to $I(r) = \frac{\sin k_F r}{k_F r}e^{-r/2l}$, where $l = \hbar k_F\tau/m$ is the elastic mean free path, the contribution from largely separated three spins with the scale of r decays rapidly as $\sim e^{-3r/2l}/(k_F r)^3$, and the Hall effect is dominantly driven by chirailties of spins on small triangles. Thus, we can neglect the contribution from the larger triangles than those with the length of the sides about equal to l. A crucial point is that although simple sum of the chirality without geometrical factor ($[\cdots]$ term in Eq. (1.29)) vanishes, the uniform chirality may be finite if the spatial inhomogeneiety of the lattice is taken into account in the geometrical weight factor.

In canonical spin glass (a dilute noble metal/3d transition metal alloys) [58–60], the interaction between localized moments is the RKKY interaction which is mediated by conduction electrons via the s-d exchange coupling $J_{sd}(>0)$. Since the Heisenberg spins are frozen in a spatially random manner in the spin glass ordered state, the sign of the local chirality appears randomly, which inevitably leads to the vanishing total chirality in the bulk, i.e. $\chi_0 = 0$. However, in the presence of the spin-orbit interaction, the term which couples the total chirality to the total magnetization M:

$$H_{SO} = \alpha\lambda M\chi_0 \tag{1.30}$$

induces the chirality-induced Hall resistivity whose magnitude is proportional to M and λ, where a coupling coefficient α depends on the band structure. The chirailty induced term in additional to the conventional normal and anomalous Hall terms has been observed in many canonical spin glass sytems, e.g. Au-Fe [61], as well as reentrant spin glass systems, e.g. $Fe_{1-x}Al_x$ [62] and $La_{1.2}Sr_{1.8}Mn_2O_7$ [63].

It is noted that in both the cases exemplified above, in order to get a net chiralty, the spin-orbit interaction must be invoked. In contrast, for some cases described in

Table 1.1 Examples of THE and several corresponding papers

System	Theory	Experiment	Spin-orbit interaction
CMR manganites	[13]	[54]	Necessary
Kagomè/pyrochlore lattice	[64–66]	[67, 68]	Unnecessary
Triangular lattice[a]	[69, 70]	[71]	Unnecessary
Distorted fcc lattice	[72]	–	Unnecessary
Skyrmion lattice	[8]	[73–75]	Unnecessary
Canonical spin glass	[58–60]	[61–63]	Necessary

[a]For triangular lattice, some special spin structure such as 4-sublattice order is needed for nonzero scalar spin chirality

the following subsections, the total scalar spin chirality survives even in the absence of the spin-orbit interaction. A significant feature of the Berry phase in THE is that the $\boldsymbol{r}$-space Berry phase sometimes shows dominant contribution rather than $\boldsymbol{k}$-space one which also manifests in AHE. A crossover of dominant contribution from $\boldsymbol{k}$-space to $\boldsymbol{r}$-space one occurs when the mean free path l becomes smaller than the length of spin texture. When the $\boldsymbol{r}$-space Berry phase causes THE, the Hall resistivity is independent of τ ($\rho_H \propto \tau^0$, i.e. $\sigma_H \propto \tau^2$), while the Hall conductivity is independent of τ in the case of $\boldsymbol{k}$-space one ($\sigma_H \propto \tau^0$, i.e. $\rho_H \propto \tau^2$). Since the relation of $\rho_H \propto \tau^0$ is same as the normal Hall effect, the $\boldsymbol{r}$-space Berry curvature can be regarded as fictitious magnetic field in real space, as discussed later.

We briefly summarize recent theories and experiments in Table 1.1. It should be noted that even if a noncoplanar spin configuration is realized, such as helical magnets under applied magnetic field, the scalar spin chirality often sums to zero due to the structural symmetry of the lattice and no THE is expected. The rare exception appears in some materials with special lattice structures e.g. Kagomè, pyrochlore, or distorted-fcc lattice and in those with special spin structures e.g. 4-sublattice orders on triangular lattice or Skyrmion lattice phases. As explained above, THE has been observed also in case that the spin-orbit interaction breaks the chirality symmetry e.g. in CMR manganites and canonical spin glass systems.

1.3.2 k-Space Berry Phase

Neglecting the spin-orbit interaction, the scalar spin chirality in real space often cancels out due to the symmetry of lattice structure. On the other hand, the gauge field corresponding to the Berry phase in $\boldsymbol{k}$ space potentially becomes non-zero for the Bloch wavefunctions in the momentum space. Roughly speaking, this happens when the unit cell contains more than two different types of loops, and each band feels the fluxes with different weights to obtain the Chern number [76]. Actually, a nonvanishing THE is obtained in 2D Kagomè or 3D pyrochlore lattice [64–66]. Although the net scalar spin chirality in the real space is zero also in Kagomè or pyrochlore lattice, it is connected to the Berry curvature in $\boldsymbol{k}$ space and therefore

THE is induced. In the strong coupling limit, the matrix element for hopping from $j \to i$ is given by

$$t_{ij}^{\text{eff}} = t_{ij}\langle\chi_i|\chi_j\rangle = t_{ij}e^{ia_{ij}}\cos(\theta_{ij}/2), \tag{1.31}$$

where $|\chi_i\rangle$ is the two-component spinor spin wave function with quantization axis $||\boldsymbol{S}_i$. If $\boldsymbol{S}_i$, $\boldsymbol{S}_j$, and $\boldsymbol{S}_k$ are the local spins at sites i, j, and k, respectively, the product of the three transfer integrals corresponding to the loop $i \to j \to k \to i$ is

$$\langle\boldsymbol{n}_i|\boldsymbol{n}_k\rangle\langle\boldsymbol{n}_k|\boldsymbol{n}_j\rangle\langle\boldsymbol{n}_j|\boldsymbol{n}_i\rangle \tag{1.32}$$

$$= (1 + \boldsymbol{n}_i \cdot \boldsymbol{n}_j + \boldsymbol{n}_j \cdot \boldsymbol{n}_k + \boldsymbol{n}_k \cdot \boldsymbol{n}_i) + i\boldsymbol{n}_i \cdot (\boldsymbol{n}_j \times \boldsymbol{n}_k), \tag{1.33}$$

where $|\boldsymbol{n}_i\rangle$ is the two-component spinor wavefunction of the spin state polarized along $\boldsymbol{n}_i = \boldsymbol{S}_i/|\boldsymbol{S}_i|$. Its imaginary part is proportional to the scalar spin chirality $\boldsymbol{S}_i \cdot (\boldsymbol{S}_j \times \boldsymbol{S}_k)$ (Fig. 1.5). The phase acquired by the electron's wave function around the loop leads to the Aharonov-Bohm (AB) effect, and consequently, to a large Hall response. In a Kagomè lattice ferromagnet, a unit cell contains three independent sites. If the scalar spin chirality per triangle unit is denoted by ϕ, the Chern numbers of three bands are $C_1 = -\text{sgn}(\sin\phi)$, $C_2 = 0$, and $C_3 = +\text{sgn}(\sin\phi)$ [64, 65], which means that the quantum Hall effect is realized.

The Hall effect which seems to be irrelevant with the magnetization in $Nd_2Mo_2O_7$ [57, 67] and $Pr_2Ir_2O_7$ [68] has been explained by this model. For $Nd_2Mo_2O_7$, Nd spins form "two-in, two-out" structures due to the strong spin anisotropy with the easy axis pointing to the center of each tetrahedron. The spin chirality of Nd moments is transmitted to the Mo spins via the f-d exchange interaction, and a conduction electron moving in the Mo sublattice would feel a fictitious magnetic field which is parallel to $\boldsymbol{M}$ (Fig. 1.7a, b).

The analysis in $\boldsymbol{k}$ space above is justified when the magnetic unit cell is small compared with the mean free path l [76]. If l is smaller than the size of the spin texture, the analysis in $\boldsymbol{r}$ space becomes more appropriate than $\boldsymbol{k}$ space. This situation is realized in "Skyrmion" crystal, which will be explained in the next subsection.

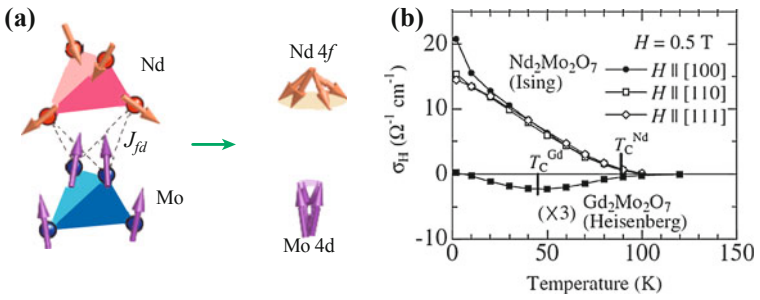

Fig. 1.7 **a** Schematic spin structure of $Nd_2Mo_2O_7$ in the ferromagnetic phase. **b** Temperature dependence of Hall conductivity for $Nd_2Mo_2O_7$ and $Gd_2Mo_2O_7$ [57]. Reprinted with permission from American Physical Society

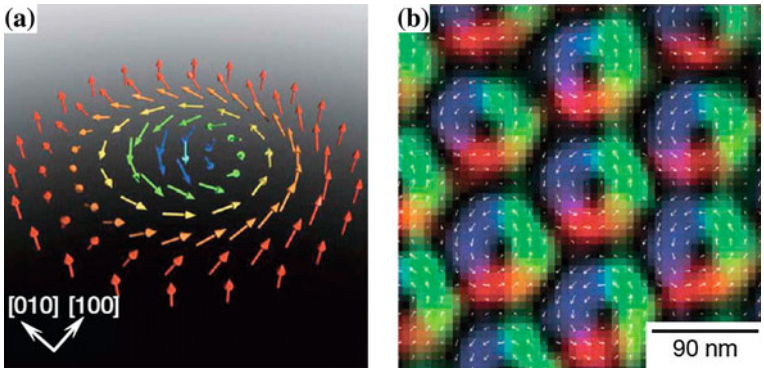

Fig. 1.8 **a** Schematic of the spin configuration in a Skyrmion [79]. **b** The contour map of the Skyrmion crystal structure for $Fe_{0.5}Co_{0.5}Si$. (Lorentz TEM data) [79]. Reprinted with permission from Nature Publishing Group

Fig. 1.9 Geometrical meaning of B_{eff} in Eq. (1.34)

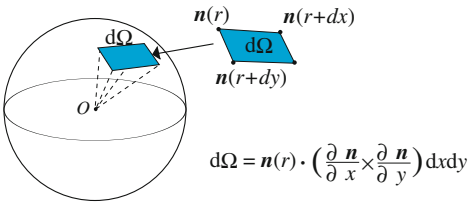

1.3.3 r-Space Berry Phase

An important example of THE induced by the $\boldsymbol{r}$-space Berry phase is Skyrmion, a vortex-like spin-swirling object (Fig. 1.8a). Recently, small angle neutron scattering studies and Lorentz transmission electron microscopy (TEM) have detected the formation of a triangular lattice of Skyrmions in some B20-type helimagnets, e.g. MnSi [77], $Fe_{1-x}Co_xSi$ [78, 79] and FeGe [80] (Fig. 1.8b). In the continuum approximation, the (topological) fictitious magnetic flux originating from the slowly-varying spin texture $\boldsymbol{n}(\boldsymbol{r}) \equiv \boldsymbol{S}(\boldsymbol{r})/|\boldsymbol{S}(\boldsymbol{r})|$ is expressed as [53]

$$B_{\text{eff}} = \frac{\phi_0}{4\pi}\boldsymbol{n}(\boldsymbol{r}) \cdot \left(\frac{\partial \boldsymbol{n}(\boldsymbol{r})}{\partial x} \times \frac{\partial \boldsymbol{n}(\boldsymbol{r})}{\partial y}\right), \tag{1.34}$$

where ϕ_0 is the quantum flux $\phi_0 = hc/e$. B_{eff} in Eq. (1.34) corresponds to the solid angle for the small area depicted in Fig. 1.9. The integral of B_{eff} in Eq. (1.34) over an area S indicates the total topological magnetic field on S. For a Skyrmion, the spin variation spans the entire area of a sphere. Thus, the topological magnetic field for a Skyrmion is

$$B_{\text{eff}} = \pm\phi_0. \tag{1.35}$$

A Skyrmion with $B_{eff} = -\phi$ is sometimes called "Anti-Skyrmion". The number of Skyrmions (Skrymion number) is defined by

$$N_s = \frac{1}{4\pi}\int_A dxdy\boldsymbol{n}\cdot\left(\frac{\partial \boldsymbol{n}}{\partial x}\times\frac{\partial \boldsymbol{n}}{\partial y}\right). \tag{1.36}$$

For a (Anti-)Skrymion, $N_s = 1$ (-1). For Skyrmion lattice phase realized in chiral helimagnets e.g. MnSi, the fictitious flux proportional to the Skyrmion density ($B_{\rm eff} = \phi_0 N_s$) induces the THE. The Hall effect induced by this fictitious flux should be treated theoretically in the real space, i.e. $\rho_{yx}^T \sim R_0 B_{eff}$, where R_0 is the normal Hall coefficient [81].

The experiments of Hall effect in MnSi have been reported at ambient pressure [73] and under high pressure [74]. The observed THE at ambient pressure is very small ($|\rho_{yx}^T| \sim 4$ nΩcm) and limited in a very narrow temperature (<1K) magnetic field (<0.1 T) window. Recently, on the other hand, large THE has been observed in polycrystalline MnGe, which has the same crystal structure with MnSi [75]. By powder neutron diffraction measurement at zero field, it was clarified that MnGe shows the helimagnetic transition at $T_N \approx 170$ K and the helical period varies from 6 to 3 nm with decrease of temperature (Fig. 1.10c), which is the shortest among the known B20-type helimagnets (Table 1.2). Since the lattice spacing in the Skyrmion latice is shown to be of the same order as the helical period for MnSi, $Fe_{1-x}Co_xSi$, and FeGe, the highest-density Skyrmion lattice is highly expected if realized in a magnetic field. As shown in Fig. 1.10a and b, the magnetic field dependence of Hall resistivity deviates from that of magnetization and the deviation becomes more conspicuous below 30 K, where the sign change of ρ_{yx} is observed. The additional component in the Hall effect was estimated as the topological Hall term by the fitting curve $\rho_{yx} = R_0\mu_0 H + R_s\rho_{xx}^2 M + \rho_{yx}^T$. The magnitude of ρ_{yx}^T is almost independent of scattering rate i.e. $\rho_{yx}^T \propto \tau^0$ (Fig. 1.10d), which is consistent with the theoretical prediction [81].

Comparison between the theory and experiments are summarized in Table 1.2. $B_{eff} = \sqrt{3}\phi_0/2\lambda^2$ is calculated from the Skyrmion density by using the helix period in zero field under assumption that the Skyrmion arranges in a triangular net with the nearest-neighbor distance is $2\lambda/\sqrt{3}$. The maximal value of $|\rho_{yx}^T|$ is 35 times larger in MnGe than in MnSi, which almost corresponds to the ratio of B_{eff} between MnGe and MnSi. However, the quantitative value of $|\rho_{yx}^T|^{\max}/R_0$ in MnSi is much smaller than the expected B_{eff}. This discrepancy has been explained by a polarization factor, which indicates the ratio between majority- and minority-spin. Since the conduction electrons are not fully polarized ($P < 1$), the corrected expression of the Hall effect is $\rho_{yx}^T \approx PR_0B_{eff}$. The factor P(<0.1) may have additional meaning because the Hund coupling is not so large in these compounds compared with CMR manganites.

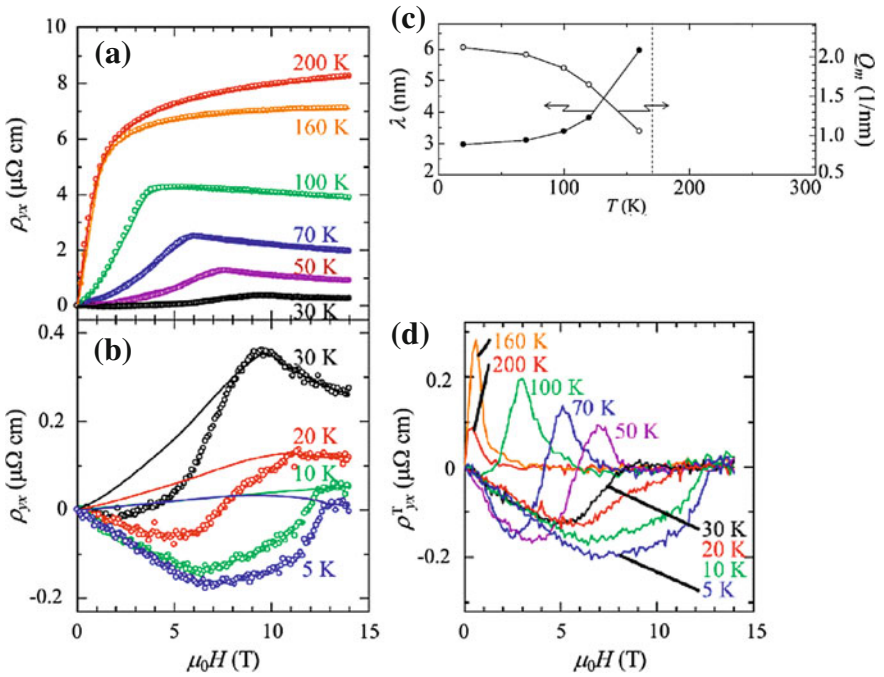

Fig. 1.10 **a**, **b** Hall resistivity ρ_{yx} at various temperatures. *Solid lines* are the fitted curves of ρ_{yx}. **c** Temperature dependence of the helical period λ and the magnitude of magnetic modulation vector $\boldsymbol{Q}_m$. The *dashed line* indicates T_N. **d** Magnetic field dependence of topological Hall resistivity ρ^T_{yx}. These data are taken from [75]. Reprinted with permission from American Physical Society

Table 1.2 Fictitous flux (B_{eff}) and topological hall resistivity (ρ^T_{yx}) in Skyrmion crystal phase of MnSi and MnGe

Material	λ (nm)	B_{eff} (T)	$\lvert\rho^T_{yx}\rvert^{\max}$ (nΩcm)	$\lvert\rho^T_{yx}\rvert^{\max}/R_0$ (T)
MnSi	17.5	11.7	4.5	~ 0.3
MnGe	$3 \sim 6$	$398 \sim 100$	160	–

The normal hall coefficient (R_0) is too small to be estimated correctly for MnGe

1.4 Purpose and Constitution

In this section, we summarize what has been achieved and what is not yet understood for AHE and THE, and then describe the purpose in this book.

(i) anomalous Hall effect in itinerant ferromagnets (Chaps. 3 and 4)

Some of recent (important) developments are summarized as follows:

1. The connection between topological concepts and the intrinsic mechanism have been clarified [36, 37]. The intrinsic anomalous Hall current should show the dissipationless nature, which is promising for future device with low energy loss.

2. Three distinct regimes as a function of σ_{xx} at low temperatures have been recognized [14, 18]. In the clean region, the skew-scattering is predominant ($\sigma_{xy}^{A} \propto \sigma_{xx}$). In the intermediate region, the intrinsic mechanism is dominant and σ_{xy}^{A} hardly depends on σ_{xx} ($\sigma_{xy}^{A} \sim$ constant). In the dirty regime, σ_{xy}^{A} depends on σ_{xx} such as $\sigma_{xy}^{A} \propto \sigma_{xx}^{1.6}$.

Some of open questions are as follows:

1. Temperature (inelastic scattering) dependence of AHE. Many reports have targeted only elastic scattering which corresponds to impurity scattering dominant only in very low temperature region.
2. Study of the extrinsic mechanisms. While the intrinsic mechanism has been reinterpreted in terms of the Berry phase and investigated by many recent experiments, the extrinsic mechanisms (skew scattering and side jump) have not been sufficiently understood.

In response to these questions, I study the following topics in the present study:

1. We investigate the influence of inelastic scattering on AHE in terms of Lorenz ratio, which is determined by the ratio between electrical and thermal Hall conductivities. Especially, I discuss on the influence of inelastic scattering on the dissipationless nature of the intrinsic anomalous Hall current (Chap. 3) and on the intrinsic to extrinsic (skew scattering) crossover (Sect. 4.1).
2. We study the skew-scattering-induced AHE in Fe by systematic change of impurity elements in it. (Sect. 4.2)

(ii) topological Hall effect in itinerant helimagnets (Chap. 5)

Recently, THE has been observed in some magnets. The results are summarized as follows:

1. For pyrochlore magnets [9, 68], (canonical) spin glass systems [61–63], CMR manganites [54], and Skyrmion lattice phases of chiral helimagnets [1, 73, 74] (etc.), the THE induced by scalar spin chirality has been observed.
2. In MnGe, the large THE possibly induced by Skyrmion has been observed in much wider temperature magnetic-field window than in MnSi [75].

Important problems are as follows:

1. In itinerant helimagnets, although the noncoplanar spin structure is generally expected under magnetic field, the THE is often not expected by the cancellation of the scalar spin chirality due to the structural symmetry. Actually, there have been few reports on the THE in itinerant helimagnets except for the Skyrmion lattice phases of B20-type chiral helimagnets.
2. Since the Skyrmion lattice phase in MnSi is narrow, THE driven by heat current in that phase is too difficult to investigate.

Our purposes in this topic are:

1. Research of new examples of helimagnets in which THE occurs (Sects. 5.1 and 5.2).
2. Investigation of topological Hall effects driven by heat current (Nernst effect and thermal Hall effect) in MnGe (Sect. 5.3). Since the Skyrmion lattice phase is present in much wider region for MnGe, the thermal transport property is easier to investigate than for MnSi.

References

1. E.H. Hall, Am. J. Math. **2**, 287 (1879)
2. C.L. Chien, C.R. Westgate (eds.), *The Hall Effect and Its Applications* (Plenum Press, New York, 1980)
3. E.H. Hall, Phil. Mag. **10**, 301 (1880)
4. E.H. Hall, Phil. Mag. **12**, 157 (1881)
5. A.W. Smith, R.W. Sears, Phys. Rev. **34**, 1466 (1929)
6. N. Nagaosa, J. Sinova, S. Onoda, A.H. MacDonald, N.P. Ong, Rev. Mod. Phys. **82**, 1539 (2010)
7. R.E. Prange, S.M. Girvin (eds.), *The Quantum Hall Effect* (Springer, Berlin, 1987)
8. E. Xiao, M.-C. Chang, Q. Niu, Rev. Mod. Phys. **82**, 1959 (2010)
9. Y. Yao, L. Kleinman, A.H. MacDonald, J. Sinova, T. Jungwirth, D-S. Wang, E. Wang, and Q. Niu. Phys. Rev. Lett. **92**, 037204 (2003)
10. Z. Fang, N. Nagaosa, K.S. Takahashi, A. Asamitsu, R. Mathieu, T. Ogasawara, H. Yamada, M. Kawasaki, Y. Tokura, K. Terakura, Science **302**, 92 (2003)
11. W.-L. Lee, S. Watauchi, V.L. Miller, R.J. Cava, N.P. Ong, Science **303**, 1647 (2004)
12. P.A. Lee, N. Nagaosa, X.-G. Wen, Re. Mod. Phys. **78**, 17 (2006)
13. J. Ye, Y.B. Kim, A.J. Millis, B.I. Shraiman, P. Majumdar, Z. Tesanovic, Phys. Rev. Lett. **83**, 3737 (1999)
14. S. Onoda, N. Sugimoto, N. Nagaosa, Phys. Rev. Lett. **97**, 126602 (2006)
15. J. Weischenberg, F. Freimuth, J. Sinova, S. Blügel, Y. Mokrousov, Phys. Rev. Lett. **107**, 106601 (2011)
16. T. Miyasato, N. Abe, T. Fujii, A. Asamitsu, S. Onoda, Y. Onose, N. Nagaosa, Y. Tokura. Phys. Rev. Lett. **99**, 086602 (2007)
17. J.M. Luttinger, Phys. Rev. **112**, 739 (1958)
18. S. Onoda, N. Sugimoto, N. Nagaosa, Phy. Rev. B **77**, 165103 (2008)
19. X.-J. Liu, X. Liu, J. Sinova, Phys. Rev. B **84**, 165304 (2011)
20. S. Iguchi, N. Hanasaki, Y. Tokura, Phys. Rev. Lett. **99**, 077202 (2007)
21. K. Ueno, T. Fukumura, H. Toyosaki, M. Nakano, M. Kawasaki, Appl. Phys. Lett. **90**, 072103 (2007)
22. J.H. Cho, T.J. Hwang, D.H. Kim, Y.G. Joh, E.C. Kim, D.H. Kim, W.S. Yoon, H.C. Ri, J. Korean Phys, Soc. **48**, 1400 (2006)
23. R. Ramaneti, J.C. Lodder, R. Jansen, Appl. Phys. Lett. **91**, 012502 (2007)
24. H. Toyosaki, T. Fukumura, Y. Yamada, K. Nakajima, T. Chikyow, T. Hasegawa, H. Koinuma, M. Kawasaki, Nat. Mater. **3**, 221 (2004)
25. J.S. Higgins, S.R. Shinde, S.B. Ogale, Venkatesan, and R.L. Greene. Phys. Rev. B **69**, 073201 (2004)
26. Y. Lyanda-Geller, S.H. Chun, M.B. Salamon, P.M. Goldbart, P.D. Han, Y. Tomioka, A. Asamitsu, Y. Tokura, Phys. Rev. B **63**, 184426 (2001)
27. M. Manyala, Y. Sidis, J.F. Ditusa, G. Aeppli, D.P. Young, Z. Fisk, Nat. Mater. **3**, 255 (2004)
28. M. Lee, Y. Onose, Y. Tokura, N.P. Ong, Phys. Rev. B **75**, 172403 (2007)
29. F. Matsukura, H. Ohno, A. Shen, Y. Sugawara, Phys. Rev. B **57**, R2037 (1998)

30. K.W. Edmonds, R.P. Campion, K.-Y. Wang, A.C. Neumann, B.L. Gallagher, C.T. Foxon, P.C. Main, J. Appl. Phys. **93**, 6787 (2003)
31. S.U. Yuldashev, H.C. Jeon, H.S. In, T.W. Kang, S.H. Lee, J.K. Furdyna, Phys. Rev. B **70**, 193203 (2004)
32. D. Chiba, Y. Nishitani, F. Matsukura, H. Ohno, Appl. Phys. Lett. **90**, 122503 (2007)
33. H. Ohno, H. Munekata, T. Penney, S. von Molnar, L.L. Chang, Phys. Rev. Lett. **68**, 2664 (1992)
34. A. Oiwa, A. Endo, S. Katsumoto, Y. Iye, H. Ohno, H. Munekata, Phys. Rev. B **59**, 5826 (1999)
35. R. Karplus, J.M. Luttinger, Phys. Rev. **95**, 1154 (1954)
36. T. Jungwirth, Q. Niu, A.H. MacDonald, Phys. Rev. Lett. **88**, 207208 (2002)
37. M. Onoda, N. Nagaosa, J. Phys. Soc. Jpn. **71**, 19 (2002)
38. M. Chang, Q. Niu, Phys. Rev. B **53**, 7010 (1996)
39. G. Sundaram, Q. Niu, Phys. Rev. B **59**, 14915 (1999)
40. J. Smit, Physica **21**, 877 (1955)
41. J. Smit, Physica **24**, 39 (1958)
42. L. Berger, Phys. Rev. B **2**, 4559 (1970)
43. L. Berger, Phys. Rev. B **5**, 1862 (1972)
44. A. Crépieux, P. Bruno, Phys. Rev. B **64**, 014416 (2001)
45. A. Fert, O. Jaoul, Phys. Rev. Lett. **28**, 303 (1972)
46. A. Fert, A. Friederich, Phys. Rev. B **13**, 397 (1976)
47. S.K. Lyo, T. Holstein, Phys. Rev. Lett. **29**, 423 (1972)
48. P. Nozieres, C. Lewiner, J. Phys. (Paris) **34**, 901 (1973)
49. N.A. Synitsyn, A.H. MacDonald, T. Jungwirth, V.K. Dugaev, J. Sinova, Phys. Rev. B **75**, 045315 (2007)
50. S.A. Yang, H. Pan, Y. Tao, Q. Niu, Phys. Rev. B **83**, 125122 (2011)
51. Y. Tian, L. Ye, X. Jin, Phys. Rev. Lett. **103**, 087206 (2009)
52. K.M. Seemann, Y. Mokrousov, A. Aziz, J. Miguel, F. Kronast, W. Kuch, M.G. Blamire, A.T. Hindmarch, B.J. Hickey, I. Souza, C.H. Marrows, Phys. Rev. Lett. **104**, 076402 (2010)
53. P. Bruno, V.K. Dugaev, M. Taillefumier, Phys. Rev. Lett. **93**, 096806 (2004)
54. P. Matl, N.P. Ong, Y.F. Yan, Y.Q. Li, D. Studebaker, T. Baum, G. Doubinina, Phys. Rev. B **57**, 10248 (1998)
55. G.E. Volovik, J. Phys. C Solid State Phys. **20**, L83 (1987)
56. G. Tatara, H. Kawamura, J. Phys. Soc. Jpn. **71**, 2613 (2002)
57. Y. Taguchi, T. Sasaki, S. Awaji, Y. Iwasa, T. Tayama, T. Sakakibara, S. Iguchi, T. Ito, Y. Tokura, Phys. Rev. Lett. **90**, 257202 (2003)
58. H. Kawamura, Phys. Rev. Lett. **90**, 047202 (2003)
59. H. Kawamura, Phys. Rev. Lett. **68**, 3785 (1992)
60. H. Kawamura, Phys. Rev. Lett. **80**, 5421 (1998)
61. T. Taniguchi, K. Yamanaka, H. Sumioka, T. Yamazaki, Y. Tabata, and S. Kawarazaki, Phys. Rev. Lett. 93, 246605 (2004), (and references therein).
62. T. Kageyama, N. Aito, S. Iikubo, M. Sato, J. Phys. Soc. Jpn. **72**, 1491 (2003)
63. S.H. Chun, Y. Lyanda-Geller, M.B. Salamon, R. Suryanarayanan, G. Dhalenne, A. Revcolevschi, J. Appl. Phys. **90**, 6307 (2001)
64. K. Ohgushi, S. Murakami, N. Nagaosa, Phys. Rev. B **62**, R6065 (2000)
65. Z. Wang, P. Zhang, Phys. Rev. B **76**, 064406 (2007)
66. S. Onoda, N. Nagaosa, Phys. Rev. Lett. **90**, 196602 (2003)
67. Y. Taguchi, Y. Oohara, H. Yoshizawa, N. Nagaosa, Y. Tokura, Science **291**, 2573 (2001)
68. Y. Machida, S. Nakatsuji, Y. Maeno, T. Tayama, T. Sakakibara, S. Onoda, Phys. Rev. Lett. **98**, 057203 (2007)
69. Y. Akagi, Y. Motome, J. Phys. Soc. Jpn. **79**, 083701 (2010)
70. I. Martin, C.D. Batista, Phys. Rev. Lett. **101**, 156402 (2008)
71. H. Takatsu, S. Yonezawa, S. Fujimoto, Y. Maeno, Phys. Rev. Lett. **105**, 137201 (2010)
72. R. Shindou, N. Nagaosa, Phys. Rev. Lett. **87**, 116801 (2001)
73. A. Neubauer, C. Pfleiderer, B. Binz, A. Rosch, R. Ritz, P.G. Niklowitz, P. Böni, Phys. Rev. Lett. **102**, 186602 (2009)

74. M. Lee, W. Kang, Y. Onose, Y. Tokura, N.P. Ong, Phys. Rev. Lett. **102**, 186601 (2009)
75. N. Kanazawa, Y. Onose, T. Arima, D. Okuyama, K. Ohoyama, S. Wakimoto, K. Kakurai, S. Ishiwata, Y. Tokura, Phys. Rev. Lett. **106**, 156603 (2011)
76. N. Nagaosa, Y. Tokura, Phys. Scr. **T146**, 014020 (2012)
77. S. Mühlbauer, B. Binz, F. Jonietz, C. Pfleiderer, A. Rosch, A. Neubaueer, R. Georgii, P. Böni, Science **323**, 915 (2009)
78. W. Münzer, A. Neubauer, T. Adams, S. Mühlbauer, C. Franz, F. Jonietz, R. Georgii, P. Böni, B. Pedersen, M. Schmidt, A. Rosch, and C. Pfleiderer, Phys. Rev. B 81, 041203(R) (2010).
79. X.Z. Yu, Y. Onose, N. Kanazawa, J.H. Park, J.H. Han, Y. Matsui, N. Nagaosa, Y. Tokura, Nature **465**, 901 (2010)
80. X.Z. Yu, N. Kanazawa, Y. Onose, K. Kimoto, W.Z. Zhang, S. Ishiwata, Y. Matui, Y. Tokura, Nature Mater. **10**, 106 (2010)
81. M. Onoda, G. Tatara, N. Nagaosa, J. Phys. Soc. Jpn. **73**, 2624 (2004)

Chapter 2
Sample Preparation and Measurement Methods

Abstract In this chapter, the methods of sample preparation and measurements are presented. The relation among the Hall, thermal Hall, and Nernst effects will be explained in terms of the Boltzmann equation.

Keywords Hall effect · Thermal Hall effect · Nernst-Ettingshausen effect · Wiedemann-Franz law · Mott relation

2.1 Sample Preparation

We used commercially available specimens for pure Fe, Co, and Ni (Nilaco Co.). The alloys of impurity-doped Fe, Co, and Ni were made from pure elements by means of arc melting in an argon atmosphere.

The single crystalline samples of $Fe_{1.3}Sb$ and MnP were grown by a Bridgman method. The mixtures of appropriate amounts of elemental materials were placed in evacuated quartz tubes. The tubes were then fired at 850 °C ($Fe_{1+\delta}Sb$) and at 900 °C (MnP). The ingots were crushed into powder. The powder specimens were melted in a evacuated quartz tube with V-shaped end. They were slowly dragged down through the temperature gradient produced by two-zone furnace. The polycrystalline samples of MnGe were synthesized by Kanazawa et al. [1] with a cubic-anvil-type high-pressure apparatus. A mixture of elemental materials with an atomic ratio of 1 : 1 was placed in a cylindrical BN capsule and was heattreated for 1 h at 800 °C under a high pressure of 4 GPa.

All the samples were cut into rectangular shape to measure transport properties.

Y. Shiomi, *Anomalous and Topological Hall Effects in Itinerant Magnets*,
Springer Theses, DOI: 10.1007/978-4-431-54361-9_2, © Springer Japan 2013

2.2 Measurements

2.2.1 Hall Effect and Magnetization Measurements

The longitudinal and Hall resistivities were measured with use of Physical Property Measurement System (PPMS, Quantum Design Inc.). The electric current was applied parallel to the longest side (x axis) and the magnetic field parallel to the shortest one (z axis).

The electrical resistivity and conductivity are defined by the ratio of the applied current and the induced voltage, i.e.

$$\boldsymbol{j}^e = \boldsymbol{\sigma}\boldsymbol{E} \tag{2.1}$$

and

$$\boldsymbol{E} = \boldsymbol{\rho}\boldsymbol{j}^e. \tag{2.2}$$

From $j_y^e = 0$, we obtain

$$\rho_{xx} = \frac{E_x}{j_x} \tag{2.3}$$

$$\rho_{yx} = \frac{E_y}{j_x}. \tag{2.4}$$

Magnetization measurement was done by Magnetic Property Measurement System (MPMS, Quantum Design Inc.) and PPMS.

2.2.2 Thermal Hall Effect Measurement

Measurements of longitudinal and transverse thermal conductivities were done with use of a steady-state method. We measured the longitudinal temperature gradient utilizing two thermometers (Cernox, Lake Shore Cryotronics Inc.). As for the transverse temperature gradient, both type-E thermocouples ($T \geq 50\,\mathrm{K}$) and Cernox thermometers ($T < 100\,\mathrm{K}$) were used. A resistance bridge (Model 370 AC Resistance Bridge, Lakeshore Cryotronics Inc.) was used to measure the resistances of the thermometers. For the voltage measurement of thermocouples, we used the digital multimeter equipped with preamplifier (Keithley 2002, Keithley Instruments Inc.). A 1 kΩ chip resistance was attached to the end of the sample as a heat source (Fig. 2.1).

The thermal conductivity tensor is defined in the absence of the electric current by

$$\boldsymbol{j}^Q = \boldsymbol{\kappa}(-\boldsymbol{\nabla}\boldsymbol{T}), \tag{2.5}$$

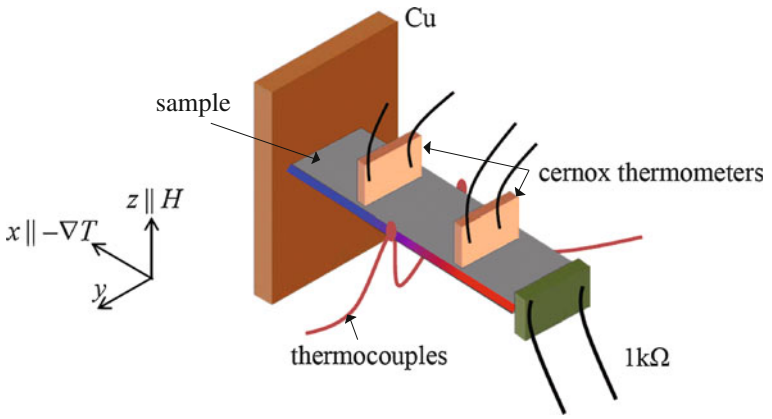

Fig. 2.1 An example of setups for thermal hall effect measurement

where the $\boldsymbol{\kappa}$ generally includes electronic contribution as well as phonon and magnon contributions. From the condition of $j_y^Q = 0$, we obtain

$$\kappa_{xx} = -\frac{j_x^Q}{\nabla_x T} \tag{2.6}$$

and

$$\kappa_{xy} = \kappa_{xx} \frac{\nabla_y T}{\nabla_x T}. \tag{2.7}$$

Even in metals, the contributions of phonon and magnon are actually important in κ_{xx}. By contrast, they can be neglected in κ_{xy}, since the phonon nor magnon hardly shows Hall effect Note that phonon Hall effect [2] and magnon Hall effect [3] have recently been reported in insulators, but the magnitude of them is much smaller than that of electronic contribution in metals.

If the conduction electrons are scattered without change of energy (elastic scattering), the thermal conductivity tensor is proportional to the electrical conductivity tensor, i.e.

$$\boldsymbol{\kappa} = L_0 \boldsymbol{\sigma} T, \tag{2.8}$$

where $L_0 = \pi^2 k_B^2 / 3e^2 = 2.44 \times 10^{-8}\ \mathrm{W\Omega/K^2}$ is called the Lorenz number (the Wiedemann-Franz law [4]). L_0 is independent of the properties of a metal, since L_0 does not depend on the scattering rate or on the energy-level structure. It is noted that degenerate Fermi statics ($k_B T \ll \varepsilon_F$) is required for its validity.

If collisions do not conserve the energy ε of each electron, thermal current (flow of $(\varepsilon - \mu)$, μ: chemical potential) will be degraded and consequently the Wiedemann-Franz law becomes violated. The expression of the Lorenz ratio $L_{xx} = \kappa_{xx}/(\sigma_{xx} T)$ including the phonon scattering is given by [5]

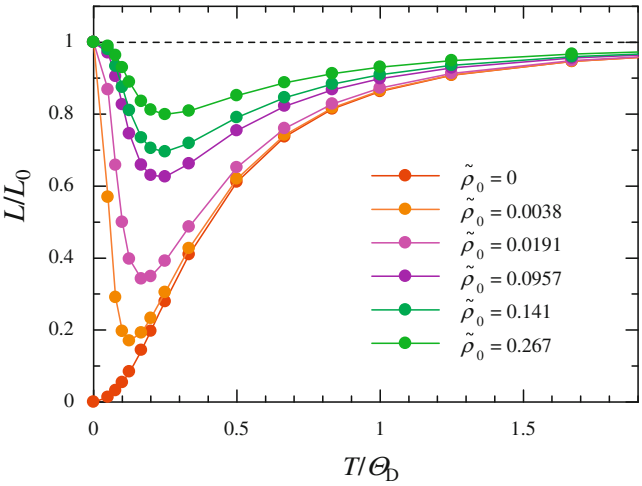

Fig. 2.2 Temperature dependence of Lorenz ratio (L)

$$\frac{L_{xx}}{L_0} = \frac{\tilde{\rho}_0 + \tilde{T}^5 \mathscr{F}_5(\tilde{T})}{\tilde{\rho}_0 + \left(1 + \frac{3}{2^{2/3}\pi^2}\tilde{T}^{-2}\right)\mathscr{F}_5(\tilde{T}) - \frac{1}{2\pi^2}\mathscr{F}_7(\tilde{T})}, \tag{2.9}$$

where $\tilde{\rho}_0$ is a renormalized residual resistivity (ρ_0), $\tilde{T} \equiv T/\Theta_D$, and

$$\mathscr{F}_n(\tilde{T}) = \int_0^{\tilde{T}^{-1}} \frac{z^n}{(e^z - 1)(1 - e^{-z})} dz. \tag{2.10}$$

The temperature dependence of L_{xx} is shown in Fig. 2.2. At the lowest temperature, the impurity scattering is dominant and $L_{xx} = L_0$. With increasing temperature, the Wiedemann-Franz law is violated due to the phonon scattering. In this region, L_{xx} decreases from L_0 rapidly. The magnitude of the deviation is larger in low-resistivity materials. In the high-temperature region, the change in energy of each electron in a collision ($\sim k_B \Theta_D$) should be small compared with $k_B T$ (quasi-elastic scattering). L_{xx} approaches L_0 again with increasing temperature and the Wiedemann-Franz law is well obeyed in $T > \Theta_D$. The Lorenz ratio for normal Hall current [$L_{xy} = \kappa_{xy}/(\sigma_{xy} T)$] also shows similar temperature dependence [6]. If the carrier density and mobility do not change with temperature, $\sigma_{xy} \propto \tau^2$ suggests $L_{xy} \sim L_{xx}^2$. This seems to be consistent with the experiment [6]. It is noted that since phonon and magnon also contribute to κ_{xx}, L_{xx} often deviates from the aforementioned behavior except for materials with high conductivity in which the electronic contribution is predominant.

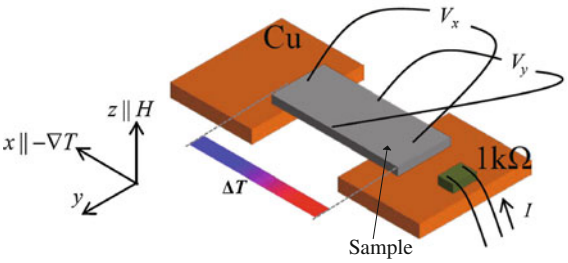

Fig. 2.3 An example of setups for Nernst effect measurement

2.2.3 Nernst Effect Measurement

Nernst effect (Nernst-Ettingshausen effect) measurement was done by a steady-state method. The longitudinal temperature gradient was measured with thermocouples or Cernox thermometers. The voltage signals of Seebeck and Nernst effect were measured with digital multimeter equipped with preamplifier and Nanovoltmeter (Keithley 2182A, Keithley Instruments Inc.). We used photosphor-bronze wires in voltage measurements for the sake of minimal heat loss. A typical setup for Nernst measurement is shown in Fig. 2.3.

Seebeck and Nernst effects are manifested by Pertier conductivity $\boldsymbol{\alpha}$, which is defined by the following relation,

$$\boldsymbol{j}^e = \boldsymbol{\sigma E} + \boldsymbol{\alpha}(-\boldsymbol{\nabla T}). \tag{2.11}$$

In the measurement condition of $\boldsymbol{j}^e = 0$,

$$\alpha_{xx} = S_{xx}\sigma_{xx} \tag{2.12}$$

and

$$\alpha_{xy} = \sigma_{xx}\left(e_{\mathrm{N}} + S_{xx}\frac{\sigma_{xy}}{\sigma_{xx}} + S_{xx}\frac{\kappa_{xy}}{\kappa_{xx}}\right), \tag{2.13}$$

where $S_{xx} = E_x/\nabla_x T$ and $e_{\mathrm{N}} = -E_y/\nabla_x T$ are Seebeck and Nernst coefficients, respectively. In the setup shown in Fig. 2.3, we need $S_{xx}\,(\kappa_{xy}/\kappa_{xx})$ term in α_{xy} because of $\Delta_y T \neq 0$ (adiabatic condition).

A relation between Pertier conductivity tensor and Hall conductivity tensor is known as the Mott relation, i.e.

$$\boldsymbol{\alpha} = \frac{\pi^2}{3}\frac{k_B^2 T}{e}\left(\frac{\partial \boldsymbol{\sigma}}{\partial \varepsilon}\right)_{\varepsilon=\mu}. \tag{2.14}$$

This relation is valid only at low temperatures, where the elastic scattering is dominant. The Mott relation is also applicable to the intrinsic mechanism of

anomalous Nernst effect [7]. However, in the presence of ambipolar diffusion, inelastic scattering, or superconducting fluctuations, it may be modified [8].

References

1. N. Kanazawa, Y. Onose, T. Arima, D. Okuyama, K. Ohoyama, S. Wakimoto, K. Kakurai, S. Ishiwata, Y. Tokura, Phys. Rev. Lett. **106**, 156603 (2011)
2. C. Strohm, G.L.J.A. Rikken, P. Wyder, Phys. Rev. Lett. **95**, 155901 (2005)
3. Y. Onose, T. Ideue, H. Katsura, Y. Shiomi, N. Nagaosa, Y. Tokura, Science **329**, 297 (2010)
4. N.W. Aschcroft, N.D. Mermin, *Solid State Physics* (Thomson Learning, London, 1976)
5. A.H. Wilson, *Theory of Metals* (Cambridge University Press, Cambridge, 1965)
6. Y. Zhang, N.P. Ong, Z.A. Xu, K. Krishana, R. Gagnon, L. Taillefer, Phys. Rev. Lett. **84**, 2219 (2000)
7. D. Xiao, Y. Yao, Z. Fang, Q. Niu, Pys. Rev. Lett. **97**, 026603 (2006)
8. D.I. Pikulin, C.Y. Hou, C.W.J. Beenakker, Phys. Rev. B **84**, 035133 (2011)

Chapter 3
Scattering-Free Nature of Intrinsic Anomalous Hall Current

Abstract First, we investigate the intrinsic AHE which is related with Berry-phase. In contrast to the extrinsic mechanisms, an intrinsic AHE induced by the Berry phase is, in principle, not affected by the scattering. Experimentally, the relation that $\rho_{yx} \propto \rho_{xx}^2$ (namely, Hall conductivity $\sigma_{xy} = \rho_{yx}/\rho_{xx}^2$ is independent of ρ_{xx}) is identified in some materials and is thought to be the evidence of the dissipationless nature of anomalous Hall current (C. Kooi, Phys. Rev. **95**, 843 (1954), W-L. Lee, S. Watauchi, V.L. Miller, R.J. Cava, and N.P. Ong, Science **303**, 1647 (2004)). Nevertheless, the same ρ_{xx} dependence of ρ_{yx} is also expected for the side jump mechanism. In addition, the Hall conductivity may show the nontrivial T- or doping-dependence because of its high sensitivity to the position of the chemical potential in the electronic band structure. Another way to examine the origin and nature of the AHE is thus highly desired. Here, we take the approach to this problem in terms of the comparative study on the charge and heat anomalous Hall currents. Since the Lorenz ratio for the anomalous Hall current (L_{xy}^A) is sensitive to the inelastic scattering, the scattering-free (dissipationless) nature of the intrinsic anomalous Hall current manifests in the temperature dependence of L_{xy}^A. Moreover, we investigate in the second section to what extent the scattering-free nature is robust against the scattering strength by changing the doping concentration in Ni, Fe, or Co.

Keywords Anomalous Hall effect · Berry phase of electrons · Spin-orbit interaction · Dissipationless electronic current · Itinerant ferromagnet

3.1 Temperature-Independent Behavior of Lorenz Ratio for Intrinsic Anomalous Hall Current

In this section we have measured the electrical and thermal Hall conductivity and investigated the Lorenz ratio for anomalous Hall current for Ni and $Ni_{0.97}Cu_{0.03}$, in which the AHE is anticipated to be induced by the intrinsic mechanism except for the low T (<100 K) region of Ni, as demonstrated by a recent study [1].

Y. Shiomi, *Anomalous and Topological Hall Effects in Itinerant Magnets*,
Springer Theses, DOI: 10.1007/978-4-431-54361-9_3, © Springer Japan 2013

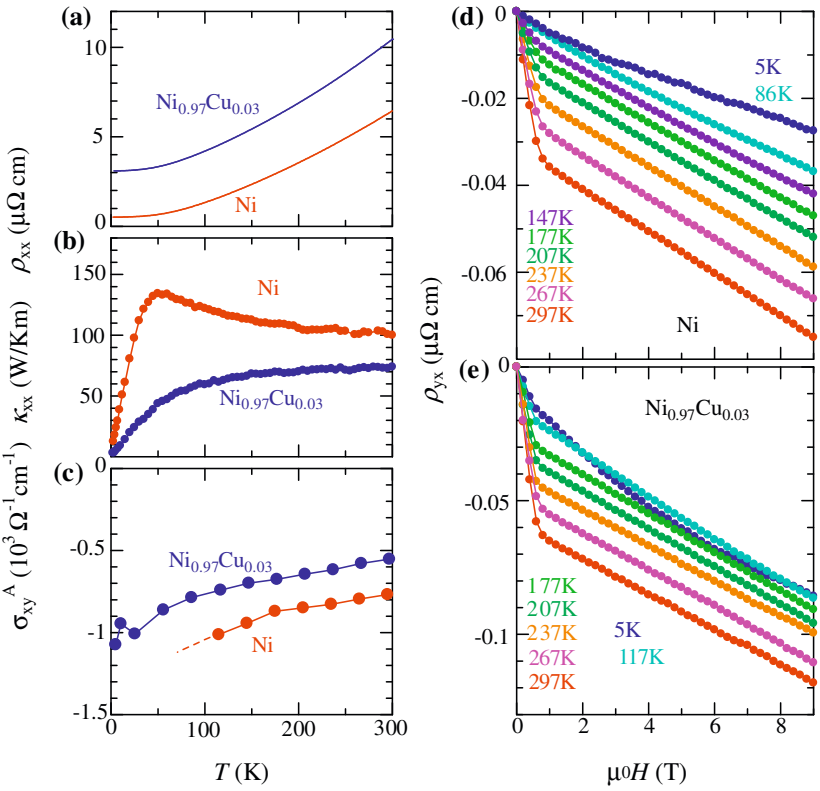

Fig. 3.1 **a**–**c** T dependence of **a** resistivity ρ_{xx}, **b** thermal conductivity κ_{xx}, and **c** anomalous part of Hall conductivity σ_{xy}^{A} for Ni and $Ni_{0.97}Cu_{0.03}$ [2]. **d**, **e** H dependence of Hall resistivity ρ_{yx} at various Ts for **d** Ni and **e** $Ni_{0.97}Cu_{0.03}$ [2]

In Fig. 3.1a, we show the T dependence of resistivity (ρ_{xx}) for Ni and $Ni_{0.97}Cu_{0.03}$. The resistivity for Ni is low ($\approx$0.5 $\mu\Omega$cm) at the lowest T and increases rapidly with T. When Cu is doped into Ni, the residual resistivity is increased but the T dependence is almost unchanged. This indicates that only the elastic impurity scattering is increased in $Ni_{0.97}Cu_{0.03}$. The thermal conductivities (κ_{xx}) for Ni and $Ni_{0.97}Cu_{0.03}$ are shown in Fig. 3.1b. The thermal conductivity for Ni increases gradually with decreasing T from 300 K, and shows a peak around 50 K. On the other hand, the thermal conductivity for $Ni_{0.97}Cu_{0.03}$ monotonically decreases with decreasing T. The nominal Lorenz ratio L_{xx} ($=\frac{\kappa_{xx}}{\sigma_{xx}T}$) does not differ too much from L_0 in a whole T region for both the samples ($1.6 \times 10^{-8} \leq L_{xx} \leq 3.2 \times 10^{-8}$), indicating that the electronic contribution is dominant to the thermal conductivity; this will be investigated in detail in the next section.

Figures 3.1d, e show the H dependence of the Hall resistivity (ρ_{yx}) for Ni and $Ni_{0.97}Cu_{0.03}$. The Hall resistivity for Ni is composed of the normal part ($\propto H$) and

the anomalous part ($\propto M$) at 297 K. While the normal part shows little T dependence above 86 K, the anomalous Hall resistivity decreases largely with decreasing T. At the lowest T, the anomalous Hall resistivity almost vanishes, and the normal part shows nonlinear field dependence. When the Cu is doped into Ni, the anomalous part becomes larger, and can be observed even at the lowest T, where the nonlinear normal part is observed as well. The nonlinear behavior for the normal part may be related to a large value of $\omega_c\tau$ (ω_c and τ being cyclotron frequency and relaxation time, respectively). The anomalous part of Hall resistivity can be obtained by the linear extrapolation from the high field above the saturation field of the magnetization ($\approx$0.6 T) to zero field. Using this procedure, we obtain and show in Fig. 3.1c the T dependence of the anomalous part of the Hall conductivity (σ_{xy}^{A}) for Ni and $Ni_{0.97}Cu_{0.03}$. The anomalous Hall conductivity for Ni increases in the absolute magnitude gradually with decreasing T. Below 86 K, it is difficult to estimate it because of the small anomalous Hall resistivity. The anomalous Hall conductivity for $Ni_{0.97}Cu_{0.03}$ shows a similar behavior, but can be estimated even at the lowest T.

In Fig. 3.2a, b, we show the H dependence of the thermal Hall conductivity (κ_{xy}) for Ni at various Ts. At 297 K, the thermal Hall conductivity is composed of the M-linear anomalous part and the H-linear normal part. Similarly to the normal part of electrical Hall conductivity (σ_{xy}), which varies with T as $\sim 1/\rho_{xx}(T)^2$, the normal part of the κ_{xy}/T increases largely with decreasing T. On the other hand, the anomalous part of the κ_{xy}/T does not show appreciable T variation, which is also similar to the electrical case. Below 86 K, it is difficult to identify the anomalous component, and the normal part shows a nonlinear behavior with H. The thermal Hall conductivity for $Ni_{0.97}Cu_{0.03}$ shows similar T and H dependences [Fig. 3.2c, d]. Compared with the pure Ni case, the normal component is smaller, while the anomalous one almost unchanged. The thermal Hall conductivity shows a kink around 0.6 T at 5 K, indicating the observable anomalous component even at the lowest T. This enables us to discuss the T dependence of the anomalous thermal Hall conductivity in the whole T region for $Ni_{0.97}Cu_{0.03}$.

Figure 3.3 compares the H dependences of thermal and electrical Hall conductivities at various Ts for Ni and $Ni_{0.97}Cu_{0.03}$. In this figure, the ordinate scales for the respective conductivities are determined so that the anomalous components for the both conductivities coincide with each other. For Ni, the whole field dependence of thermal Hall conductivity is fully scaled with that of the electrical one at 297 K. Below 207 K, however, the normal component of the thermal conductivity is suppressed compared with that of electrical conductivity. Below 56 K, the anomalous components of the both conductivities can hardly be discerned, but the field dependences become scaled again with each other. A similar T variation is seen for $Ni_{0.97}Cu_{0.03}$. The difference is that the anomalous component for $Ni_{0.97}Cu_{0.03}$ can be discerned down to the lowest T, where the both conductivities are scaled well. The violation of the scaling of the field dependences in the middle T range implies that the anomalous component of thermal Hall conductivity needs separate consideration from that of normal component.

To discuss the anomalous and normal parts separately, we define the Lorenz ratios for the anomalous and normal components, respectively, as

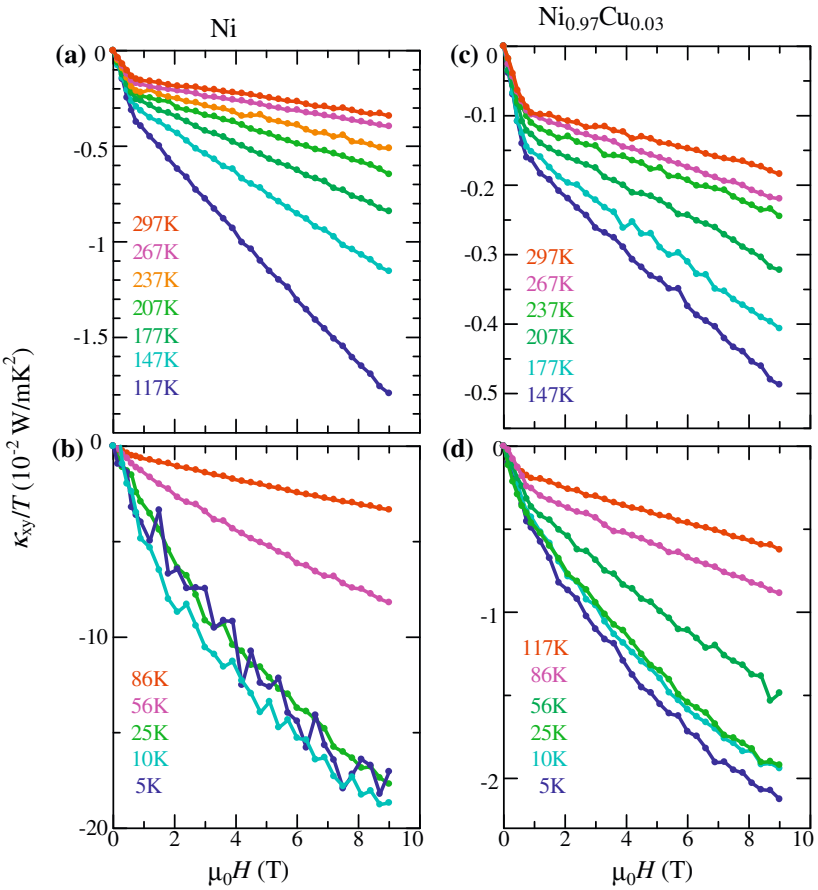

Fig. 3.2 H dependence of thermal Hall conductivity κ_{xy} at various Ts for **a**, **b** Ni and **c**, **d** $Ni_{0.97}Cu_{0.03}$ [2]

$$L^A_{xy} = \kappa^A_{xy}/\sigma^A_{xy}T \tag{3.1}$$

and

$$L^N_{xy} = \kappa^N_{xy}/\sigma^N_{xy}T\ , \tag{3.2}$$

where κ^A_{xy}, κ^N_{xy}, σ^A_{xy}, and σ^N_{xy} are the anomalous and normal components of thermal and electrical conductivities, respectively. The L^A_{xy} and L^N_{xy} for Ni and $Ni_{0.97}Cu_{0.03}$ are shown in Fig. 3.4a, b. The L^N_{xy} for Ni at the lowest T almost coincides with L_0. The L^N_{xy} decreases steeply with T and shows a minimum around 100 K. Above 100 K, the L^N_{xy} gradually increases with T. For $Ni_{0.97}Cu_{0.03}$, L^N_{xy} shows a similar behavior, but the decrease of L^N_{xy} is less significant. These behaviors are similar to

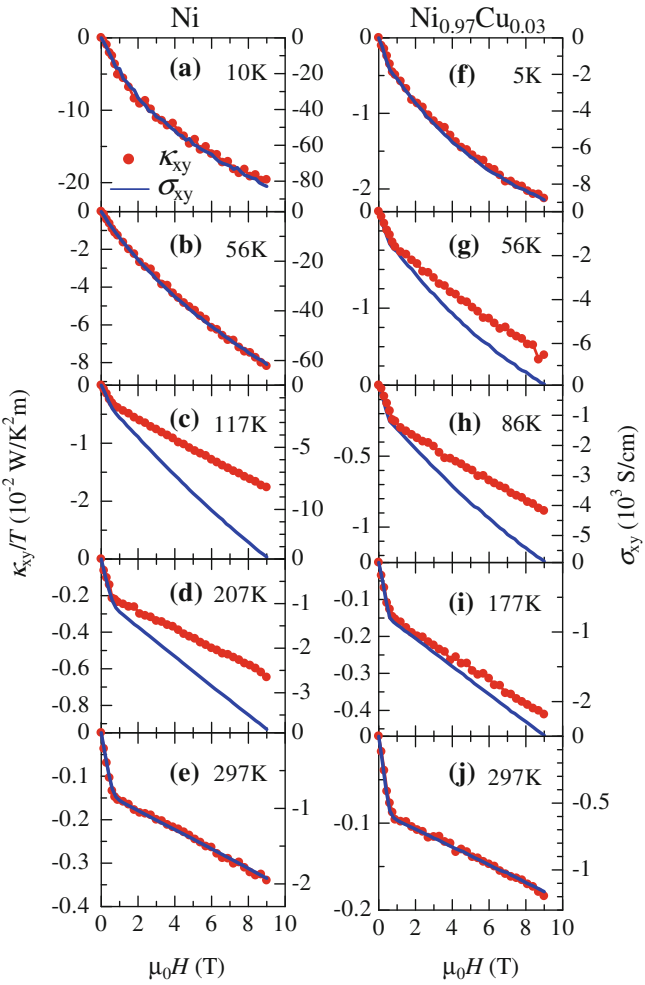

Fig. 3.3 H dependence of both electrical and thermal Hall conductivities at respective Ts for **a**–**e** Ni and **f**–**j** $Ni_{0.97}Cu_{0.03}$ [2]

the longitudinal part of Lorenz ratio (L_{xx}) for a normal metal as well as to the L_{xy} observed for a Pauli-paramagnetic metal Cu [3], and can be explained by the effect of inelastic scattering. The L_{xy}^{A} for both Ni and $Ni_{0.97}Cu_{0.03}$ almost coincides with L_0 in the low T region. This suggests that the Wiedemann-Franz law is valid also for the anomalous Hall current. For Ni, the L_{xy}^{A} remains almost constant below 180 K, while it is difficult to estimate the L_{xy}^{A} below 90 K. Above 180 K, the L_{xy}^{A} gradually decreases with T. The L_{xy}^{A} can be obtained over the whole T region for $Ni_{0.97}Cu_{0.03}$. The L_{xy}^{A} remains almost constant below 90 K down to the lowest T and decreases gradually with increasing T from 90 K. Thus, the L_{xy}^{A} shows little T dependence in

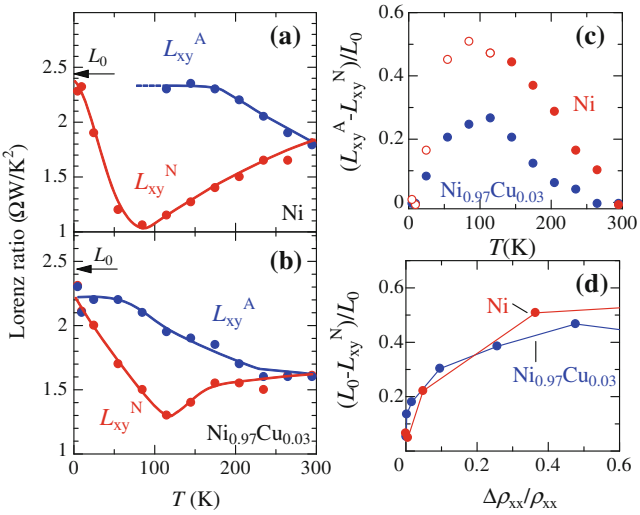

Fig. 3.4 **a**, **b** T dependences the Hall Lorenz ratios for the anomalous (L_{xy}^A) and normal parts (L_{xy}^N) for **a** Ni and **b** $Ni_{0.97}Cu_{0.03}$ [2]. **c** Difference between L_{xy}^A and L_{xy}^N for Ni and $Ni_{0.97}Cu_{0.03}$ normalized by the free-electron Lorenz number L_0 [2]. **d** The decrease of the L_{xy}^N normalized by L_0 plotted against $\Delta\rho_{xx}/\rho_0$, where ρ_0 and $\Delta\rho_{xx}$ are residual resistivity and $\rho_{xx} - \rho_0$, respectively [2]. The *arrows* in **a** and **b** indicate L_0. The *solid lines* are merely the guide to the eyes. The *open red circles* in **c** are plotted on the assumption that the L_{xy}^A for Ni is constant below 100 K, as represented by the *dashed line* in **a**

the low T region for both Ni and $Ni_{0.97}Cu_{0.03}$. In the high T region, the L_{xy}^A decreases gradually, but the decrease is much less than that of L_{xy}^N. The differences between L_{xy}^A and L_{xy}^N for Ni and $Ni_{0.97}Cu_{0.03}$ are shown explicitly in Fig. 3.4c. For the both samples, the L_{xy}^A and L_{xy}^N are almost equal to each other at the lowest T and room T, while the difference is significant around 100 K.

If there were no inelastic scattering, both the L_{xy}^A and L_{xy}^N should be equal to L_0. In other words, the deviation of the Lorenz ratio from L_0 signals the magnitude of the effect of inelastic scattering. In Fig. 3.4d, the relative deviation of the L_{xy}^N from L_0, $(L_0 - L_{xy}^N)/L_0$, in the low T region is plotted against $\Delta\rho/\rho_0$, where ρ_0 is the residual resistivity and $\Delta\rho = \rho - \rho_0$. Since ρ_0 and $\Delta\rho$ are caused by the elastic impurity scattering and inelastic scattering, respectively, the $\Delta\rho/\rho_0$ stands for the magnitude of inelastic scattering relative to that of the elastic scattering. The scaling behavior of the L_{xy}^N suggests that the decrease of Hall Lorenz ratio for the normal component certainly signals the contribution of the inelastic scattering. The reason why the decrease of L_{xy}^N for Ni is more significant than that for $Ni_{0.97}Cu_{0.03}$ is that the effect of inelastic scattering is relatively weak for $Ni_{0.97}Cu_{0.03}$ due to the larger ρ_0. Considering that L_{xy}^A is close to L_0 in the low-T region, where the scaling shown in Fig. 3.4d holds good, the T-dependent difference between L_{xy}^A and L_{xy}^N can be also ascribed to the influence of the inelastic scattering. When the intrinsic mechanism

works for the AHE in these samples, the transverse current is anticipated to be almost free from the effect of inelastic scattering, and is considered as "dissipationless current". Recently, the detailed theoretical [4, 5] and experimental [1] works have shown to what extent the intrinsic anomalous Hall current can be viewed as dissipation-free; the result is that even for the intrinsic mechanism the anomalous Hall conductivity depends on the scattering rate to some extent, but the effect is minimal in the range of $E_{SO} < \hbar/\tau < E_F$ (1–10 $\leq \rho \leq 10^{-3}$ Ωcm), where E_{SO} and E_F are the energy of spin-orbit coupling and Fermi energy, respectively. In the present case, the scattering rate is well within this range, except for the low T region ($T < 100$ K) of Ni. The T variation of Hall conductivity is weak in spite of the large residual resistivity ratio ($\rho_{300\,\mathrm{K}}/\rho_0 \approx 12$ and 3 for Ni and $Ni_{0.97}Cu_{0.03}$, respectively). The T independence of L^A_{xy} in the low T region indicates the dissipationless (scattering-free) nature, namely, the anomalous Hall current should be hardly affected by the inelastic scattering nor by the elastic scattering in this regime. Incidently, a pure dissiaptionless heat current would not affect the lattice temperature. However, the accumulated thermal energy should be eventually released to the lattice system, which we believe was measured by the actual experiment. As noted above, the anomalous Hall conductivity weakly depends on the scattering rate due to the broadening of spectral function even for the intrinsic mechanism. The gradual decrease of the L^A_{xy} in the high T region might be due to this weak influence of the scattering, and we will investigate in detail the dependence on the scattering strength in the next section.

3.2 Crossover to Scattering-Dependent Nature in High-Resistivity Regime

It is meaningful to extend the Lorenz ratio study to examine how robust the scattering-free nature of the intrinsic anomalous Hall current is against further increase in the scattering rate. For this purpose, we study here the anomalous part of the Lorenz ratio in the less-conductive region by doping more impurity into Co, Ni, or Fe.

We show the temperature (T) dependence of ρ_{xx} for the pure and impurity-doped Ni, Fe and Co in Fig. 3.5. The resistivities are very low at $T = 0$ for the pure Ni, Co, and Fe ($\rho_{xx} \sim$ 1–5 $\times 10^{-7}$ Ωcm) and steeply increase with T due to phonon and spin-wave scatterings [7]. According to the former studies [7], the resistivities of Fe, Co, and Ni in the low-T region is mainly attributed to the s-s and s-d scatterings by phonon and spin-wave and their contribution varies as T^5 or T^3 and as T^2, respectively. As T increases above Θ_D, the phonon scattering is much more important than the spin-wave scattering and the resistivity shows the T-linear dependence [7]. In fact, the T dependence of resistivity for the pure specimens changes from super-linear at the low T to linear at the high T, as seen in Fig. 3.5a, d and g. With doping impurity, the impurity scattering dominates the increasing residual resistivity. The resistivities of the most impurity-doped samples ($Ni_{0.9}Cu_{0.1}$, $Fe_{0.99}Si_{0.01}$, and $Co_{0.985}Si_{0.015}$) increase up to the order of 10^{-5} Ωcm

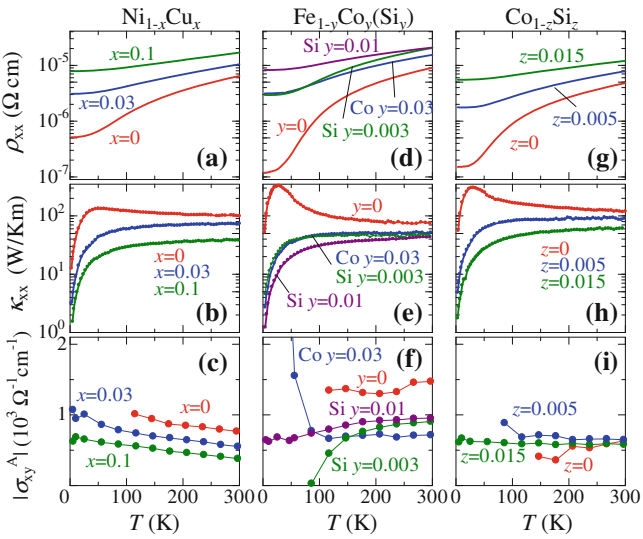

Fig. 3.5 T dependence of electrical resistivity (ρ_{xx}), thermal conductivity (κ_{xx}) and the anomalous parts of electrical Hall conductivities (σ_{xy}^{A}) for $Ni_{1-x}Cu_x$, $Fe_{1-y}Co_y(Si_y)$, and $Co_{1-z}Si_z$ [6]

and show small and monotonous T-dependences. The κ_{xx} values for all the samples are plotted as a function of T in Fig. 3.5b, e and f. The electronic contribution is dominant in κ_{xx} for such good metals as the present samples. (Later, we will argue the relative proportion of electronic and phononic contributions in more detail in terms of the Lorenz ratio.) The κ_{xx} for pure specimens are large and show broad peaks around 30 K. This peak structure is owing to the crossover between the increase of κ_{xx} due to the small scattering rate and the decrease due to the small thermal energies of the electrons with lowering T. As the impurity concentration is increased, the κ_{xx} decreases reflecting the increase in ρ_{xx}, shows no peak, and increases monotonically with T for all the impurity-doped samples.

In Fig. 3.6, we show the magnetic field (H) dependence of σ_{xy} for all the samples with solid lines. It is noted that we do not present the thermal and electrical Hall conductivities for pure Fe because they are largely dominated by the skew scattering and the intrinsic anomalous Hall effect cannot be discussed using them. The skew-scattering-induced AHE in Fe will be discussed in the next chapter. For $Ni_{0.9}Cu_{0.1}$, σ_{xy} is composed of the H-linear normal part and the M-linear anomalous part. The magnitude of the negative normal part increases with decreasing T. This is because $\sigma_{xy} \simeq \sigma_{xx}^2 \rho_{yx}$ and the σ_{xx} steeply increases with decreasing T. The anomalous part can be estimated from the linear extrapolation of the high field data to zero magnetic field. The sign of the anomalous part is also negative but the magnitude does not show large T-variation. When the Cu doping concentration is reduced, the T variation of the normal part becomes larger and the nonlinear field-dependence emerges at low T, while the T dependence of the anomalous part remains small. The nonlinear

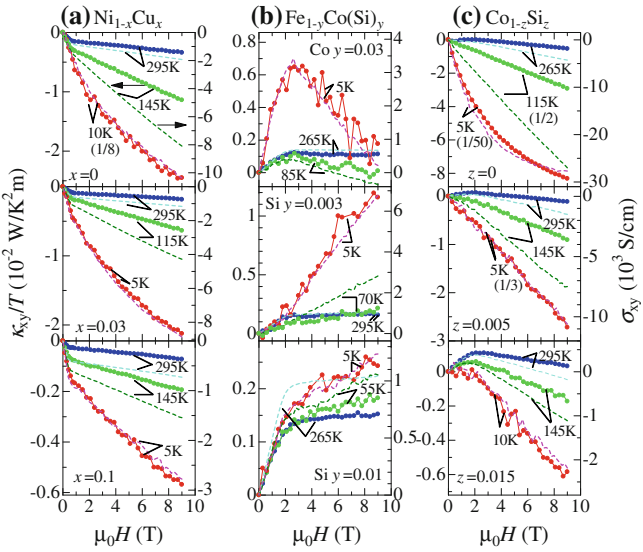

Fig. 3.6 H dependence of the thermal Hall conductivities divided by T (κ_{xy}/T, *circles*) and electrical Hall conductivities (σ_{xy}, *dashed lines*) at various Ts for **a** $Ni_{1-x}Cu_x$, **b** $Fe_{1-y}Co_y(Si_y)$, and **c** $Co_{1-z}Si_z$ [6]

behavior of the normal part is due to the large $\omega_c\tau$ (ω_c being cyclotron frequency) at the low-T region [8]. Similar T- and doping-dependences are seen in $Co_{1-x}Si_x$ system, while the sign of the anomalous part is positive and the magnitude of the normal part is larger. For the case of Fe alloys, the normal part of σ_{xy} is quite small compared with the $Ni_{1-x}Cu_x$ and $Co_{1-x}Si_x$ systems and the anomalous part does not show large T-variation in a high-T region. However, the H-linear and M-linear components change dramatically in the low-T region below 100 K for $Fe_{0.97}Co_{0.03}$ and $Fe_{0.997}Si_{0.003}$ owing to the skew scattering. The nature of the skew scattering for the Fe alloys will be discussed in the next chapter; we here concentrate on the high-T region of the Fe alloys above 100 K, where the intrinsic AHE is dominant.

In Fig. 3.5c, f and i, we show the T dependence of the anomalous Hall conductivity for all the samples. We could not accurately estimate the anomalous Hall conductivity in the low-T region ($T \lesssim 100$ K) for Fe, Co, Ni and $Co_{0.995}Si_{0.005}$ since the anomalous Hall resistivity is too low because of high σ_{xx}. As shown in Fig. 3.5c, i, the anomalous Hall conductivity for $Ni_{1-x}Cu_x$ and $Co_{1-x}Si_x$ does not show large T-variation. The absolute values for $Ni_{1-x}Cu_x$ only slightly decrease with increasing T, while those for $Co_{1-x}Si_x$ are almost constant [Fig. 3.5i]. These behaviors are consistent with the scattering-free nature of intrinsic AHE. The anomalous Hall conductivities for $Fe_{0.97}Co_{0.03}$ and $Fe_{0.997}Si_{0.003}$ are also nearly constant above 100 K, although a steep change below 100 K is caused by the skew scattering contribution. For $Fe_{0.99}Si_{0.01}$, the anomalous Hall conductivity shows small T-dependence

even in the low-T region and the skew scattering contribution ($\propto\sigma_{xx}$) is hardly discerned due to the increase of ρ_{xx}.

In Fig. 3.6, the measured values of κ_{xy}/T for all the samples are plotted with closed circles as a function of magnetic field in comparison with σ_{xy} (solid lines). The respective variations of κ_{xy}/T with the doping, H, and T share the qualitatively common features for all the samples; the field dependence of κ_{xy}/T at the lowest T coincides with that of σ_{xy} and the ratio is almost equal to L_0, satisfying the Wiedemann-Franz law. At high T, however, the magnitude of κ_{xy}/T is suppressed compared with σ_{xy} and the field dependences are different from each other. These are because the Lorenz ratio for anomalous Hall current does not coincide with that for normal Hall current.

We define the Lorenz ratios for anomalous and normal Hall currents; $L_{xy}^{A} = \kappa_{xy}^{A}/(\sigma_{xy}^{A}T)$ and $L_{xy}^{N} = \kappa_{xy}^{N}/(\sigma_{xy}^{N}T)$, where κ_{xy}^{A} and κ_{xy}^{N} (σ_{xy}^{A} and σ_{xy}^{N}) are the anomalous and normal parts of thermal (electrical) Hall conductivity, respectively. We plot the T dependences of L_{xy}^{N} and L_{xy}^{A} together with the conventional Lorenz ratio for the longitudinal conductivity [$L_{xx} = \kappa_{xx}/(\sigma_{xx}T)$] in Fig. 3.7. Note that the L_{xx} differs in principle from $L_{xx}^{\mathrm{e}}[\equiv \kappa_{xx}^{\mathrm{e}}/(\sigma_{xx}T)]$ when the contributions of phonon (κ^{ph}) and magnon (κ^{mag}) to κ_{xx} are not neglected compared with the electronic one (κ^{e}). The L_{xx} for Ni and Co almost coincides with L_0 at the lowest T, and becomes smaller than L_0 in the intermediate-T region. Then, it tends to recover to L_0 in the high-T region. This is same as the canonical T-dependence of L_{xx}^{e} as explained in Chap. 2, indicating that the electronic contribution is dominant in κ_{xx}

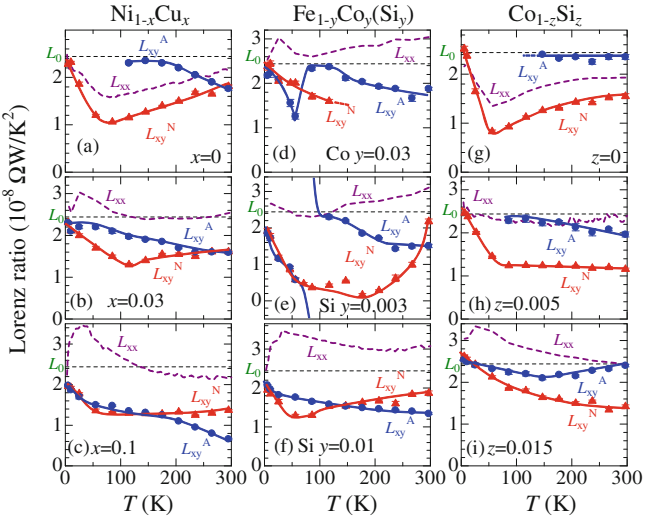

Fig. 3.7 T dependence of the Lorenz ratios for longitudinal conduction [L_{xx}, *dashed lines* (*purple*)], the normal Hall current [L_{xy}^{N}, *triangles* (*red*)], and the anomalous Hall current [L_{xy}^{A}, *circles* (*blue*)] [6]. For $Fe_{0.97}Co_{0.03}$, L_{xy}^{N} is not shown above 120 K because the normal part of Hall resistivity is too small to accurately estimate

in these highly-conductive pure materials. For the heavily impurity-doped samples ($Ni_{0.9}Cu_{0.1}$, $Fe_{0.99}Si_{0.01}$, and $Co_{0.985}Si_{0.015}$), on the other hand, L_{xx} increases with increasing T from $T = 0$ and shows a maximum around 30 K. The low-T behavior cannot be explained by the electronic contribution alone, implying some phonon contribution in these less-conducting samples.

The thermal Hall conductivity is composed of almost the electronic component alone, since phonons or magnons can hardly show Hall effect. Note that the thermal Hall effects of phonon and magnon were recently reported for $Tb_3Ga_5O_{12}$ [9] and $Lu_2V_2O_7$ [10], respectively. Nevertheless, the magnitude is quite small for phonon Hall effect ($\kappa_{xy} \leq 2\times10^{-4}$ W/Km) and magnon Hall effect. Also, magnon Hall effect should not occur in ferromagnets with simple crystal structures, such as Fe, Co, nor Ni, because it requires some conditions for lattice structure similarly to topological Hall effect [11]. The L_{xy}^N is expected to reflect the strength of the inelastic scattering similarly to $L_{xx}^{\rm e}$. As noted previously, the relation $L_{xy}^N/L_0 \propto (L_{xx}/L_0)^2$ is reported for Cu metal [3]. In the case of the pure Ni and Co, the T dependence of L_{xy}^N is similar to that of L_{xx}. To check the relation, we compare L_{xy}^N/L_0 and $(L_{xx}/L_0)^2$ for pure Ni and Co in Fig. 3.8. As is clear from the figure, the relation that $L_{xy}^N/L_0 \propto (L_{xx}/L_0)^2$ holds also for ferromagnetic metals, Ni and Co. This relation ensures the usefullness of the Hall Lorenz ratio to investigate the effect of inelastic scattering. The L_{xy}^N for impurity-doped samples also decreases with increasing T from $T = 0$, shows a minimum, and then tends to increase with T in the high-T region. For the Cu-doped Ni and Si-doped Co samples, the L_{xy}^N and the T at the minimum increase with increasing impurity concentration. This is because the ratio of inelastic to elastic scattering

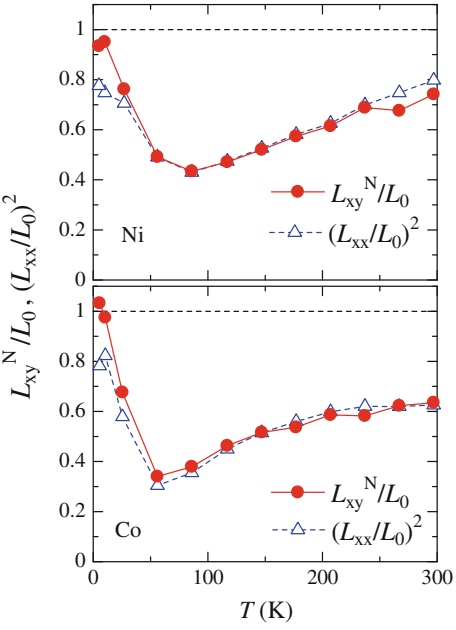

Fig. 3.8 Comparison between $(L_{xx}/L_0)^2$ and L_{xy}^N/L_0 for pure Ni and Co [6]

decreases with impurity doping. A similar impurity-concentration dependence of L_{xx}^{e} has been known for long [12] (see Sect. 2.2 of Chap. 2).

The T-variation of L_{xy}^{A} is rather different from those of L_{xx} and L_{xy}^{N} as shown in Fig. 3.7. For pure Co, L_{xy}^{A} shows less deviation from L_0 above 140 K, while it cannot be accurately estimated below 140 K. This indicates that the anomalous Hall current is hardly affected by the inelastic scattering. As discussed in the previous section, this is an indication of scattering-free nature of Berry-phase-induced anomalous Hall effect. For $Co_{0.995}Si_{0.005}$, the L_{xy}^{A} coincides with L_0 and shows little T-deviation in the low-T region, while it begins to decrease with increasing T from 150 K. With further increase of Si impurity ($Co_{0.985}Si_{0.015}$), L_{xy}^{A} decreases with T even in the low-T region. In the $Ni_{1-x}Cu_x$ system, the decrease in L_{xy}^{A} is observed around 160 K even for the pure ($x = 0$) sample. This onset T of the decrease becomes 90 K for $x = 0.03$. For $Ni_{0.9}Cu_{0.1}$ ($x = 0.1$), the L_{xy}^{A} gradually decreases with increasing T from the lowest T. In the case of impurity-doped Fe samples, $Fe_{0.97}Co_{0.03}$ and $Fe_{0.997}Si_{0.003}$, the L_{xy}^{A} shows steep change below 100 K, which is caused by the skew scattering as discussed in the next chapter. Apart from the influence of skew scattering, the L_{xy}^{A} coincides with L_0 around 100 K but decrease with T above 150 K. For $Fe_{0.99}Si_{0.01}$, the L_{xy}^{A} monotonically decreases with increasing T from the lowest T similarly to the high-doped cases of $Ni_{0.9}Cu_{0.1}$ and $Co_{0.985}Si_{0.015}$. Thus, there is the crossover from $L_{xy}^{A} \approx L_0$ to $L_{xy}^{A} < L_0$ in common for Ni-, Co-, and Fe-based systems. Since the decrease of L_{xy}^{A} is caused by the effect of inelastic scattering, the scattering-free nature appears to be lost above the crossover T.

To discuss this phenomenon more quantitatively, we plot L_{xy}^{A} as a function of temperature (T) and the longitudinal resistivity $\rho_{xx}(T)$ in Fig. 3.9 for all the samples. The low-T data below 100 K for $Fe_{0.97}Co_{0.03}$ and $Fe_{0.997}Si_{0.003}$ are omitted in this plot; they are dominated by the extrinsic skew scattering, which we do not discuss in this section. For $Ni_{1-x}Cu_x$ system, the data except the low-T region for $x = 0.1$ fall on to a single curve. The L_{xy}^{A} is almost equal to L_0 in the low-ρ_{xx} region, but it deviates in the high-ρ_{xx} region. Similar tendency is also observed for Co and Fe systems. Thus, the effect of inelastic scattering on the anomalous Hall current seems to change at $\rho_{xx} \sim 3$–6×10^{-6} Ωcm for all the three systems. Incidentally, open triangles in Fig. 3.9 mark the sharp convergence of $L_{xy}^{A}(T)$ into $L_{xy}^{A}(T = 0) \approx L_0$ in lowering T toward $T = 0$ for the higher-resistive samples with higher doping; this should be distinguished from the aforementioned crossover ρ_{xx} value. The crossover is not related to the energy gap of phonon nor magnon, since the gaps should not be changed so dramatically by the small amount of impurity doping. In addition, the crossover is dominated by the magnitude of resistivity value, which reflects the sum of the inelastic and elastic scattering rates, not the inelastic scattering alone. Therefore, the crossover shold be caused by the scattering rates exceeding some critical energy scale. A similar type of crossover for the intrinsic AHE was proposed by Miyasato et al. (experiment) [1] and by Onoda et al. (theory) [4, 5] as mentioned in Chap. 1. In that case, the σ_{xx} dependence of σ_{xy} changes from $\sigma_{xy} \propto \sigma_{xx}^{0}$ to $\sigma_{xy} \propto \sigma_{xx}^{1.6}$ around $\rho_{xx} \sim 10^{-4}$–10^{-3} Ωcm. However, this ρ_{xx} value is much larger than the present crossover value ($\rho_{xx} \sim 3$–6×10^{-6} Ωcm). (In the present case, any

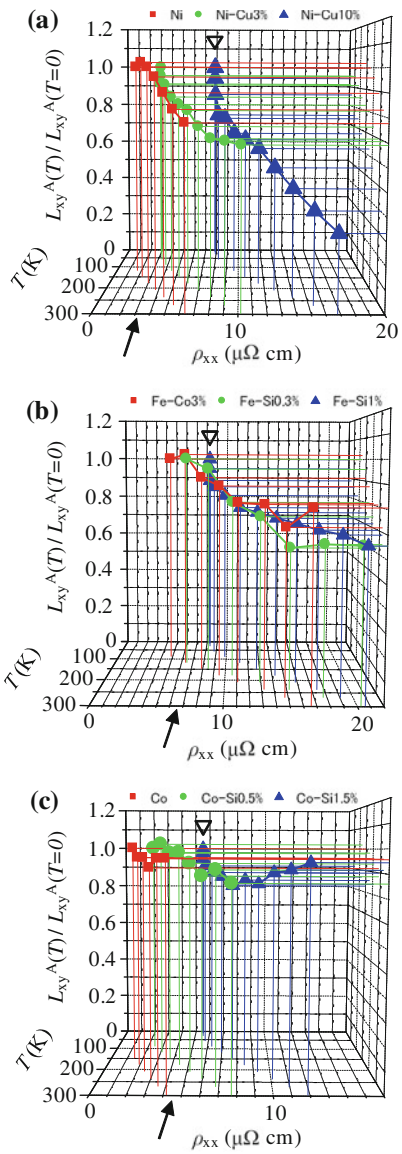

Fig. 3.9 The $\rho_{xx}(T)$ dependence of L_{xy}^{A}/L_{xy}^{A} $(T = 0)$ for **a** $Ni_{1-x}Cu_x$, **b** $Fe_{1-y}Co_y(Si_y)$, and **c** $Co_{1-z}Si_z$. The values of L_{xy}^{A} $(T = 0)$ are estimated by extrapolation from the finite-T data in Fig. 3.7. We omit the low-T data governed by the skew scattering for $Fe_{0.97}Co_{0.03}$ and $Fe_{0.997}Si_{0.003}$. The *arrows* indicate the critical ρ_{xx} values, above which L_{xy}^{A} tends to deviate from its $T = 0$ value ($\approx L_0$). *Open triangles* mark the sharp convergence of L_{xy}^{A} (T) into $L_{xy}^{A}(T = 0) \approx L_0$ in lowering T towards $T = 0$ for the higher-resistive samples with higher doping; this should be distinguished from the aforementioned crossover ρ_{xx} value

appreciable change in σ_{xy} is not discerned in Fig. 3.5 around our crossover value.) The Lorenz ratio study as presented here should be more sensitive to the scattering effect than the σ_{xy}-σ_{xx} analysis and enabled us to identify another crossover of the AHE with change of scattering rate. Then, the next question is what is the origin of the crossover. From the observed value of the crossover resistivity, we can estimate the corresponding scattering rate, $\hbar/\tau \sim 20\,\mathrm{meV}$, assuming the carrier density $n \sim 1.7 \times 10^{22}/\mathrm{cm}^3$ for Fe. Here, the carrier density for Fe is approximately esimated

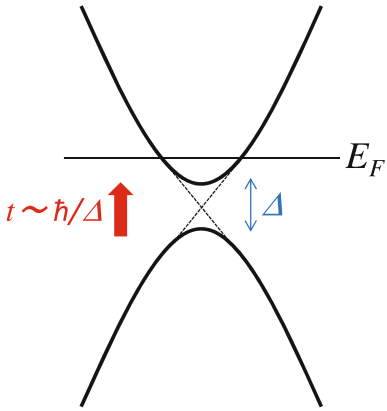

Fig. 3.10 Band anti-crossing point around Fermi energy (E_F), where energy gap is caused by the spin-orbit coupling (see Sect. 1.2.1 of Chap. 1)

as the 4s-like conduction electron density [13]. The energy scale is much smaller than Fermi energy ($\sim$10 eV) and exchange spilitting ($\sim$1 eV). Only one quantity on a similar energy scale is the magnitude of energy gap at the band anti-crossing point caused by the spin-orbit coupling; the gap of $\sim$70 meV is estimated in terms of first-principles band calculation for Fe [14] (see also Sect. 1.2.1 of Chap. 1). The interband mixing is decisive for Berry-phase-induced AHE, therefore the broadening of the electronic spectrum greater than the gap magnitude (Δ) around the band anti-crossing point is likely to take away the scattering-free nature of anomalous Hall current. From the other point of view, the lifetime of virtual interband-transition induced by electric field is given by $\sim\hbar/\Delta$ according to the uncertainty principle (Fig. 3.10). Since this lifetime is independent of scattering (i.e. τ), the intrinsic mechanism is considered to exhibit the dissipationless nature. When the scattering effect becomes stronger and τ becomes smaller than $\hbar/\Delta$, however, the scattering starts to affect the intrinsic mechanism, and consequently, the anomalous Hall current becomes dissipative.

3.3 Summary

The major results in this chapter are summarized as follows:

- We have observed the anomalous *thermal* Hall effect for (Cu-doped) Ni, (Si-doped) Co, and (Si or Co-doped) Fe.
- The Hall Lorenz ratio for the anomalous component L_{xy}^A almost coincides with the free-electron Lorenz number L_0 at the lowest T. This confirms the validity of Wiedemann-Franz law for the anomalous Hall current as well.
- While the Hall Lorenz ratio for the normal component L_{xy}^N decreases significantly with increasing T from the lowest T, the L_{xy}^A for slightly-doped Ni and Co shows little T dependence in the low T region. This is an indication of the dissipationless nature of the intrinsic anomalous Hall effect.

- The Lorenz ratio for the intrinsic anomalous Hall current L_{xy}^{A} coincides with L_0 when ρ_{xx} is smaller than 3–6 $\times$ 10^{-6} Ωcm. This is an indication of scattering-free nature of Berry-phase-induced intrinsic anomalous Hall current. When ρ_{xx} exceeds the value of 3–6 $\times 10^{-6}$ Ωcm, on the other hand, L_{xy}^{A} decreases and deviates from L_0. The value of ρ_{xx} at the crossover is estimated to be $\hbar/\tau \sim 20$ meV for Fe, which is comparable to the expected magnitude of the energy gap around band anticrossing point formed by the spin-orbit interaction.

References

1. T. Miyasato, N. Abe, T. Fujii, A. Asamitsu, S. Onoda, Y. Onose, N. Nagaosa, Y. Tokura, Phys. Rev. Lett. **99**, 086602 (2007)
2. Y. Onose, Y. Shiomi, Y. Tokura, Phys. Rev. Lett. **100**, 016601 (2008)
3. Y. Zhang, N.P. Ong, Z.A. Xu, K. Krishana, R. Gagnon, L. Taillefer, Phys. Rev. Lett. **84**, 2219 (2000)
4. S. Onoda, N. Sugimoto, N. Nagaosa, Phys. Rev. Lett. **97**, 126602 (2006)
5. S. Onoda, N. Sugimoto, N. Nagaosa, Phy. Rev. B **77**, 165103 (2008)
6. Y. Shiomi, Y. Onose, Y. Tokura, Phys. Rev. B **81**, 054414 (2010)
7. D.A. Goodings, Phys. Rev. **132**, 542 (1963), and references therein
8. J.M. Ziman, *Principles of the Theory of Solids* (Cambridge University Press, Cambridge, 1972)
9. C. Strohm, G.L.J.A. Rikken, P. Wyder, Phys. Rev. Lett. **95**, 155901 (2005)
10. Y. Onose, T. Ideue, H. Katsura, Y. Shiomi, N. Nagaosa, Y. Tokura, Science **329**, 297 (2010)
11. T. Ideue, Y. Onose, H. Katsura, Y. Shiomi, S. Ishiwata, N. Nagaosa, Y. Tokura, Phys. Rev. B **85**, 134411 (2012)
12. A.H. Wilson, *Theory of Metals* (University Press, Cambridge, 1965)
13. N.F. Mott, H. Jones, *The Theory of the Properties of Metals and Alloys* (Dover, New York, 1958)
14. Y. Yao, L. Kleinman, A.H. MacDonald, J. Sinova, T. Jungwirth, D.-S. Wang, E. Wang, Q. Niu, Phys. Rev. Lett. **92**, 037204 (2003)

Chapter 4
Skew-Scattering-Induced Anomalous Hall Effect in Impurity-Doped Fe

Abstract In this chapter, we investigate the AHE induced by skew scattering mechanism for impurity-controlled Fe. While recent theoretical and experimental works show that the AHE can be well explained by the Berry phase theory in most cases, Onoda et al. theoretically showed that the skew-scattering mechanism should be dominant in the clean-limit regime. Miyasato et al. investigated the AHE for nominally pure Fe to explore the clean-limit regime. They observed some crossover in this regime and assigned it to the intrinsic to extrinsic crossover. This kind of crossover behavior in Fe had already been reported in literature of decades ago (P.N. Dheer, Phys. Rev. **156**, 637 (1967), A.K. Majumdar and L. Berger, Phys. Rev. **B 7**, 4203 (1973)). Nevertheless, the extrinsic skew-scattering-induced AHE in ferromagnets could hardly be analyzed quantitatively because of the difficulty in discriminating it from the nonlinearly H-dependent normal Hall conductivity in this region and because of the difficulty in theoretical elucidation. In this chapter, we examine the nature of the skew-scattering-induced AHE in impurity-controlled Fe. In the first section, we investigate the crossover from intrinsic to extrinsic mechanism caused by T elevation in terms of the Lorenz ratio for nominally-pure, Si-doped, and Co-doped Fe. In the second section, we reveal the different nature of the skew-scattering mechanism between Co-doped and Si-doped Fe by systematic study on the impurity-element dependence.

Keywords Anomalous Hall effect · Skew-scattering mechanism · Side-jump mechanism · Spin-orbit interaction · Fe

4.1 Anomaly in Lorenz Ratio due to Intrinsic–Extrinsic Crossover

Figure 4.1a shows the temperature (T) dependence of the electrical conductivity σ_{xx} for nominally-pure Fe ($4N$ purity; major impurity is Si of 16 ppm), $Fe_{0.997}Si_{0.003}$, $Fe_{0.99}Si_{0.01}$, $Fe_{0.99}Co_{0.01}$, $Fe_{0.97}Co_{0.03}$ and $Fe_{0.9}Co_{0.1}$. The σ_{xx} at the lowest T (σ_0) for nominally-pure Fe is as large as $10^7\ \Omega^{-1}\mathrm{cm}^{-1}$, but decreased by doping Co or Si.

Y. Shiomi, *Anomalous and Topological Hall Effects in Itinerant Magnets*,
Springer Theses, DOI: 10.1007/978-4-431-54361-9_4, © Springer Japan 2013

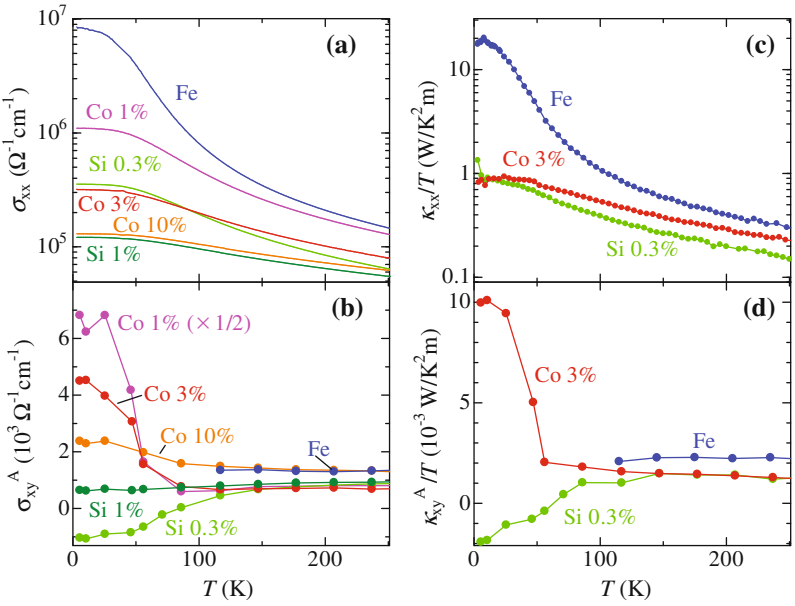

Fig. 4.1 T profiles of **a** the electrical conductivity (σ_{xx}), **b** the anomalous part of electrical Hall conductivity (σ_{xy}^{A}), **c** the thermal conductivity (κ_{xx}) divided by T and **d** the anomalous part of thermal Hall conductivity (κ_{xy}^{A}) divided by T [1]. For the Co 1 % doped sample, $\sigma_{xy}^{A}/2$ is shown in (**b**)

In Fig. 4.1c, we show the T variations of the thermal conductivity κ_{xx} (divided by T) for nominally-pure Fe, $Fe_{0.97}Co_{0.03}$ and $Fe_{0.997}Si_{0.003}$. The κ_{xx}/T monotonically increases with decreasing T similarly to σ_{xx}, which indicates that the electronic contribution is dominant in κ_{xx}. The H dependences of Hall resistivities, electric ρ_{yx} and thermal $w_{yx} \equiv \kappa_{xy}/(\kappa_{xx}^2 + \kappa_{xy}^2)$, at 5 K are shown in Fig. 4.2. While the Hall resistivity for nominally-pure Fe shows quadratic H-dependence, those for $Fe_{0.997}Si_{0.003}$, $Fe_{0.99}Si_{0.01}$ and $Fe_{0.97}Co_{0.03}$ are composed of well-defined H-linear normal and M-linear anomalous terms. It is to be noted that the anomalous term is negative for $Fe_{0.997}Si_{0.003}$ contrary to other specimens, signaling the sensitivity of the low-T Hall resistivity to the species and amounts of the impurities and hence to the impurity scattering.

The anomalous parts of the Hall conductivities σ_{xy}^{A} and κ_{xy}^{A}/T for all the samples are plotted as a function of T in Fig. 4.1b, d. These are calculated from the linear extrapolation from the high-H values above the saturation H of the magnetization, as exemplified by dashed lines in Fig. 4.2. The σ_{xy}^{A} and κ_{xy}^{A}/T for nominally-pure Fe cannot be deduced below 100 K because of difficulty in estimating the anomalous part due to the high-H nonlinear behavior of ρ_{yx} and $w_{yx}T$. The σ_{xy}^{A} and κ_{xy}^{A}/T for all the samples are almost constant above 100 K, reminiscent of the dominant intrinsic component both for the charge and heat Hall transport. The difference in the σ_{xy}^{A}

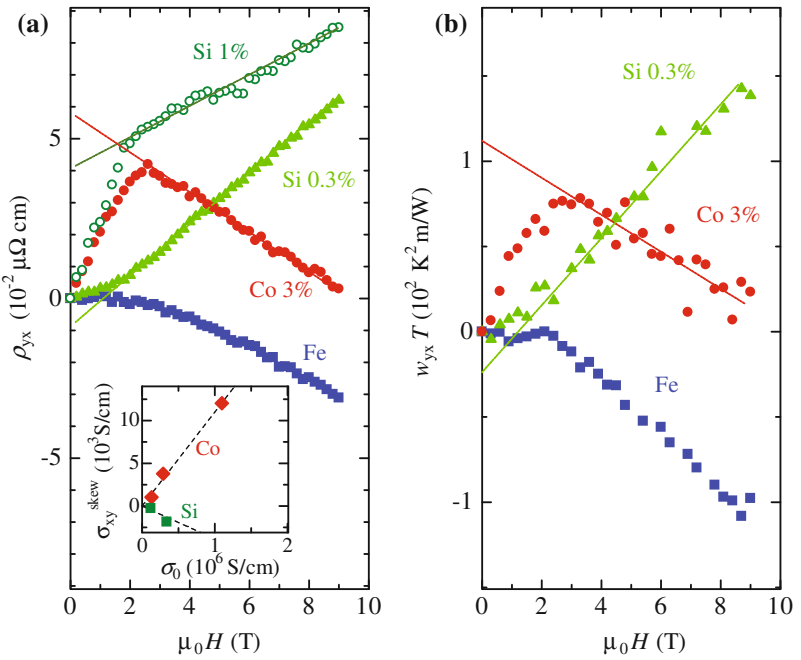

Fig. 4.2 **a**, **b** H dependence of the electrical and thermal Hall resistivity [$\rho_{yx} = \sigma_{xy}/(\sigma_{xx}^2 + \sigma_{xy}^2)$ and $w_{yx} = \kappa_{xy}/(\kappa_{xx}^2 + \kappa_{xy}^2)$, respectively] at $T = 5$ K for each sample [1]. The *dashed lines* exemplify the extrapolation procedure for the estimate of the anomalous Hall resistivity. The inset shows the skew scattering induced anomalous Hall conductivity (σ_{xy}^{skew}) (see text for definition) plotted against the lowest-T conductivity (σ_0, inverse of residual resistivity). *Diamonds* (*red*) and *squares* (*green*) represent the data of Co-doped and Si-doped samples, respectively

at high Ts (>100 K) among the samples may be ascribed to the difference in Fermi energy which is dependent on the species and amount of the dopant. For Si-doped Fe the σ_{xy}^A and κ_{xy}^A/T decrease with decreasing T below 100 K. For Co-doped Fe, by contrast, the σ_{xy}^A and κ_{xy}^A/T increase with decreasing T below 100 K. We plotted the low-T change of σ_{xy}^A, $\sigma_{xy}^{skew} = \sigma_{xy}^A(T = 5\,\mathrm{K}) - \sigma_{xy}^A(T = 207\,\mathrm{K})$, as a function of the longitudinal conductivity σ_{xx} at the lowest T (5 K) in the inset of Fig. 4.2. Here, this definition of σ_{xy}^{skew} assumes (i) the skew-scattering contribution vanishes at 207 K and (ii) the intrinsic and side-jump contribution is constant with T. The validity of these assumptions will be discussed in the next section. As the impurity content increases, the magnitude of σ_{xy}^{skew} decreases rapidly and the intrinsic AHE seems to become dominant. The σ_{xy}^{skew} is proportional to σ_{xx} with the positive and negative slope for Co-doped and Si-doped samples, respectively. The linear relation agrees with the skew scattering theory [2–5] and the sign and slope should reflect the effective impurity potential. The dependence on impurity species will be discussed detailedly in the next section. The onset T of the skew scattering is almost identical (∼100 K). Thus, the contribution of the skew scattering is also clearly observed in

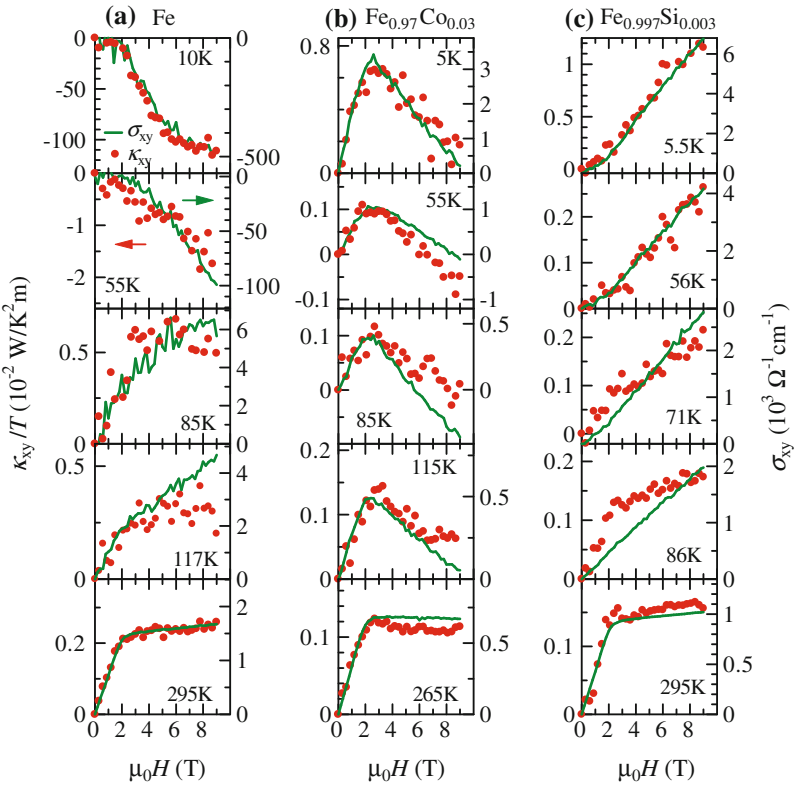

Fig. 4.3 H dependence of electrical and thermal Hall conductivities (σ_{xy} *solid lines* and κ_{xy}/T *dots*, respectively) for **a** nominally-pure Fe, **b** $Fe_{0.97}Co_{0.03}$, and **c** $Fe_{0.997}Si_{0.003}$ [1]

κ_{xy}^{A}/T below 100 K. As described below, the Hall Lorenz ratio $L_{xy} = \kappa_{xy}/(\sigma_{xy}T)$ at the lowest T (5 K), where the skew scattering totally dominates the Hall effect, is $\sim L_0$.

Figure 4.3 compares the thermal and electrical Hall conductivities at various Ts for these samples. At any T, the electrical and thermal Hall conductivities (σ_{xy} and κ_{xy}) for $Fe_{0.97}Co_{0.03}$ and $Fe_{0.997}Si_{0.003}$ are composed of the M-linear anomalous part and the H-linear normal part, apart from the indistinguishable feature for nominally-pure Fe below 100 K. The H dependence of κ_{xy} roughly scales with that of σ_{xy} for all the samples. Nevertheless, the ratio of the normal to anomalous components is different between κ_{xy} and σ_{xy} in some cases (e.g., at 117 K for Fe and 86 K for $Fe_{0.997}Si_{0.003}$). This signals that the Lorenz ratio for anomalous component $L_{xy}^{A} = \kappa_{xy}^{A}/(\sigma_{xy}^{A}T)$ is different from that for normal component $L_{xy}^{N} = \kappa_{xy}^{N}/(\sigma_{xy}^{N}T)$, as shown in the previous chapter. On the basis of these data, we show L_{xy}^{A} and L_{xy}^{N} in Fig. 4.4. For $Fe_{0.97}Co_{0.03}$, we cannot obtain L_{xy}^{N} accurately above 120 K because of the small magnitude of the normal Hall conductivity. Although the Hall conductivity for nominally-pure Fe

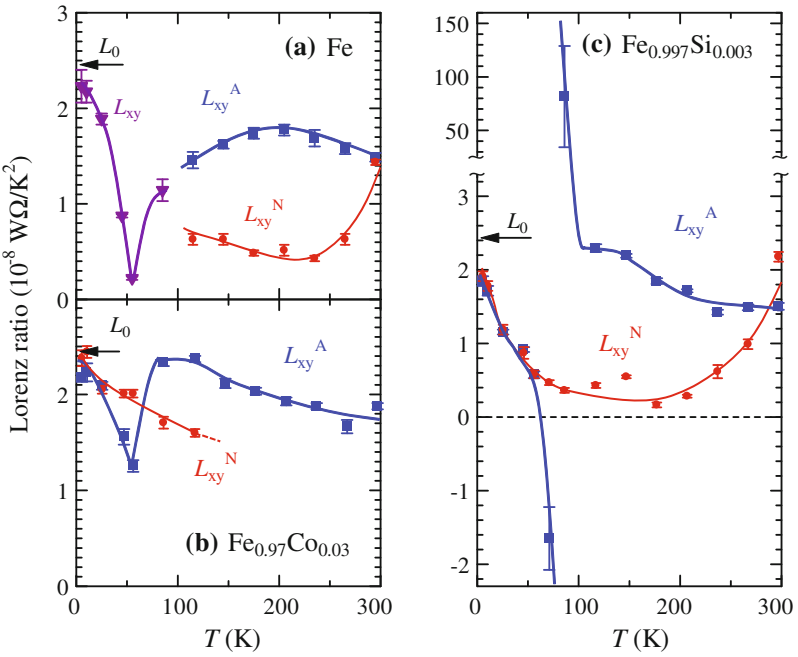

Fig. 4.4 T dependence of Lorenz ratio for Hall current for **a** nominally-pure Fe, **b** $Fe_{0.97}Co_{0.03}$, and **c** $Fe_{0.997}Si_{0.003}$ [1]. The *squares* (L^A_{xy}; *blue*) and *circles* (L^N_{xy}; *red*) indicate the Lorenz ratios for anomalous and normal Hall currents (see text for definition), respectively. *Triangles* (*purple*) in **a** stand for the Lorenz ratio determined by the scaling of the whole H-dependence of thermal and electrical conductivities. The *solid* and *dashed lines* are merely the guide for the eyes. L_0 ($= 2.44 \times 10^{-8}\,\mathrm{W\Omega/K^2}$) is the free electron value prescribed by the Wiedemann-Franz law

below 100 K cannot be decomposed into normal and anomalous parts, the scaling of the whole H dependence of both the Hall conductivities is fairly good in this T region. We plot in Fig. 4.4a this Lorenz ratio L_{xy} for nominally-pure Fe. The L^A_{xy} for $Fe_{0.97}Co_{0.03}$ [Fig. 4.4b] increases gradually with decreasing T from 300 K, almost coincides with L_0 around 150 K, but abruptly decreases below 80 K. After showing a sharp minimum around 60 K, it recovers to L_0 at the lowest T. The L^A_{xy} for $Fe_{0.997}Si_{0.003}$ [Fig. 4.4c] varies with T similarly to the case of $Fe_{0.97}Co_{0.03}$ above 100 K. Below 100 K, however, it divergently increases and then turns to a negative value at 71 K. Below 50 K, it again increases toward L_0 at the lowest T. These steep changes in L^A_{xy} below 100 K are not discerned for the higher-doped sample $Fe_{0.99}Si_{0.01}$ [see Fig. 3.7f]. The L^N_{xy} for all the samples shows a large downward deviation from L_0 with a broad minimum around 150 K. The total L_{xy} (with indistinguishable normal and anomalous components) for nominally-pure Fe shows a sharp minimum around 60 K similar to the L^A_{xy} for $Fe_{0.97}Co_{0.03}$.

The effect of inelastic scattering as measured by the deviation of Lorenz number from L_0 can be seen not only in L^N_{xy} but also in the low-T (<100 K) L^A_{xy}.

Around 150 K, the L_{xy}^{A} for all the samples is larger than L_{xy}^{N} and close to L_0. This indicates that the anomalous Hall current is hardly affected by the inelastic scattering in this T range; this is due to the dissipation-less nature of the Berry phase induced AHE, as discussed in the previous chapter. The abrupt change of L_{xy}^{A} for $Fe_{0.97}Co_{0.03}$ and $Fe_{0.997}Si_{0.003}$ occurs around the onset T ($\sim$100 K) of the skew scattering in the electrical conduction. The decrease of L_{xy}^{A} for $Fe_{0.97}Co_{0.03}$ can be thus ascribed to the non-dissipative to dissipative crossover of AHE due to the emergence of skew scattering at finite Ts. The negative Lorenz ratio for $Fe_{0.997}Si_{0.003}$ at 71 K means that the direction of the electrical current is opposite to that of the thermal current. This surprising phenomenon can be explained as follows. The Lorenz ratio can be defined for both the Berry-phase- and the skew-scattering-induced anomalous Hall currents, $L_{\mathrm{xy}}^{\mathrm{int}}$ and $L_{\mathrm{xy}}^{\mathrm{skew}}$. The L_{xy}^{A} is then expressed as

$$L_{\mathrm{xy}}^{\mathrm{A}} = \frac{\kappa_{\mathrm{xy}}^{\mathrm{skew}} + \kappa_{\mathrm{xy}}^{\mathrm{int}}}{\sigma_{\mathrm{xy}}^{\mathrm{skew}} + \sigma_{\mathrm{xy}}^{\mathrm{int}}} \frac{1}{T} = \frac{L_{\mathrm{xy}}^{\mathrm{skew}} \sigma_{\mathrm{xy}}^{\mathrm{skew}} + L_{\mathrm{xy}}^{\mathrm{int}} \sigma_{\mathrm{xy}}^{\mathrm{int}}}{\sigma_{\mathrm{xy}}^{\mathrm{skew}} + \sigma_{\mathrm{xy}}^{\mathrm{int}}} . \tag{4.1}$$

Here, $\kappa_{\mathrm{xy}}^{\mathrm{skew}}$, $\kappa_{\mathrm{xy}}^{\mathrm{int}}$, $\sigma_{\mathrm{xy}}^{\mathrm{skew}}$ and $\sigma_{\mathrm{xy}}^{\mathrm{int}}$ stand for the thermal and electrical Hall conductivities induced by the skew scattering (extrinsic) and the Berry phase (intrinsic), respectively. $L_{\mathrm{xy}}^{\mathrm{skew}}$ is quite T-dependent, whereas $L_{\mathrm{xy}}^{\mathrm{int}}$ is nearly constant ($\approx L_0$) because of the dissipation-less nature of the intrinsic AHE. Note that the sign of $\sigma_{\mathrm{xy}}^{\mathrm{skew}}$ and $\kappa_{\mathrm{xy}}^{\mathrm{skew}}$ is opposite to that of $\sigma_{\mathrm{xy}}^{\mathrm{int}}$ and $\kappa_{\mathrm{xy}}^{\mathrm{int}}$ for $Fe_{0.997}Si_{0.003}$. This is the reason why a negative value is observed for L_{xy}^{A} of $Fe_{0.997}Si_{0.003}$ in the crossover T region. Conversely, the *negative* Lorenz ratio for $Fe_{0.997}Si_{0.003}$ is viewed as the compelling evidence for the existence of two distinct anomalous Hall currents, i.e. induced by the skew scattering and the Berry phase.

As detailed in the next section, we can estimate the intrinsic and extrinsic anomalous Hall conductivities ($\sigma_{xy}^{\mathrm{intrinsic}}$ and $\sigma_{xy}^{\mathrm{extrinsic}}$, respectively) for Si-doped Fe by an empirical relation of Eq. (4.4), as shown in Fig. 4.5. Here it is assumed that the intrinsic anomalous Hall conductivity is independent of T (scattering rate), while the extrinsic anomalous Hall conductivity ($\sigma_{xy}^{\mathrm{extrinsic}} = \sigma_{xy}^{\mathrm{skew}} + \sigma_{xy}^{\mathrm{side-jump}}$) changes with T (scattering rate) through $\sigma_{xx}[T]^2$. As shown in Fig. 4.5, the intrinsic to extrinsic crossover occurs between 86 and 71 K for Si0.3 %-doped Fe, which is consistent with the above results of Lorenz ratio [Fig. 4.4c].

4.2 Change of Skew-Scattering Contribution Among Various Impurity Elements

In this section, we further examine the skew-scattering-induced AHE observed in Fe. We reveal the different nature of the skew-scattering-induced AHE between Co-doped and Si-doped Fe by systematic study of the dependence on the impurity species. For Co-doped Fe, the resonant skew scattering mechanism [6] seems to show

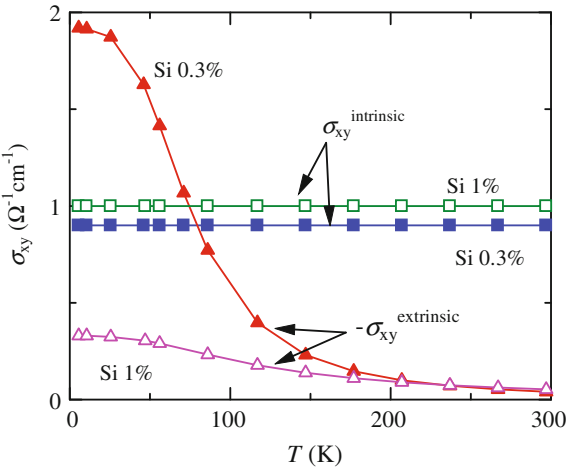

Fig. 4.5 T dependence of the estimated anomalous Hall conductivity of intrinsic and extrinsic origins ($\sigma_{xy}^{\text{intrinsic}}$ and $\sigma_{xy}^{\text{extrinsic}}$, respectively) for Fe doped with Si (0.3 and 1 %). With increasing Si concentration, the extrinsic term (skew scattering term) decreases and thus the intrinsic contribution becomes dominant down to the lowest T

large anomalous Hall effect. For Si-doped Fe, by contrast, the impurity potential is considered to be weak and the skew-scattering-induced ρ_{yx}^{A} does not show any T dependence.

4.2.1 Resonant Skew Scattering for Fe Doped with 3d Transition Metal Series

Firstly, we investigate the variation of skew scattering contribution through the 3*d* transition metal impurities (Ti - Cu). Here, the impurity-doped specimens have not been obtained for Zn and Ga due to the high-rate evaporation during synthesis (arc melting). For (nominally-)pure iron, as shown in Fig. 4.2a, since $\omega_c \tau$ is very large corresponding to the small resistivity, the normal Hall resistivity shows $\sim H^2$ dependence, which makes the analysis of anomalous Hall term difficult. By controlling the concentration of dopants, we tuned the residual resistivities to 2–5 $\mu\Omega$ cm so that the anomalous Hall term can be clearly distinguished by the extrapolation from high H [Fig. 4.6a].

Figure 4.7 shows H dependence of the Hall resistivity for these samples. The Hall resistivities show the kink structure around 2 T, corresponding to the saturation H of magnetization. For the early transition metal impurities (Ti, V, Cr, and Mn), the slope of the ρ_{yx} in high-H region is positive at 297 K, while that of Co is negative. For Ni, Cu, and Ge, the slope again turns to be positive. We show the impurity-species dependence of the normal Hall coefficients (R_0) in Fig. 4.6c. The R_0 is larger than that of nominally-pure Fe for the early transition metal series and smaller for the late transition metal series except for Ni1 %-doped specimen. Although R_0 of

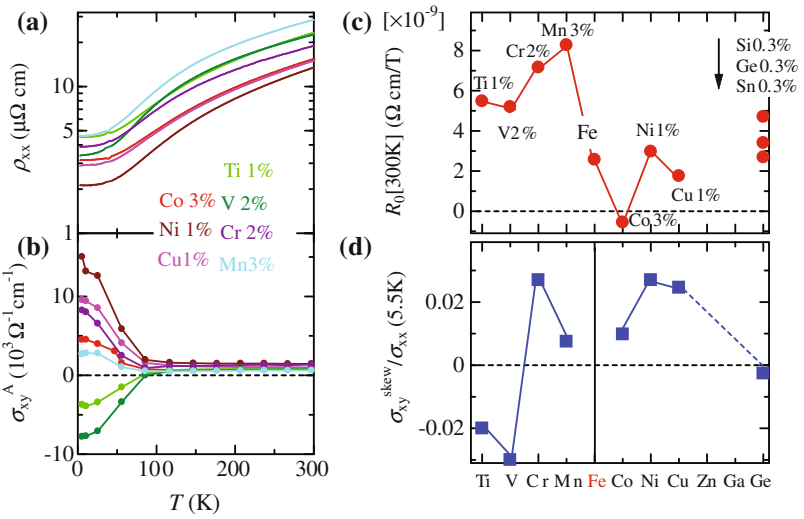

Fig. 4.6 T dependence of **a** the resistivity ρ_{xx} and **b** the anomalous Hall conductivity σ_{xy}^{A} for Fe doped with 3*d* transition metal impurity (Ti-Cu). **c** The normal Hall coefficient for Fe doped with 3*d* transition metal impurity (Ti-Cu), Si, Ge, or Sn. For Si, Ge, or Sn-doped samples, see also Fig. 4.10. **d** Skew scattering coefficient for the impurity (Ti-Zn, and Ge)-doped Fe. The *dashed line* is merely the guide for the eyes

negative sign for Co-doped Fe seems to be electron-doped by Co, the complex band structure of Fe makes such a simple analysis difficult.

The anomalous Hall resistivity extrapolated from high-H data is 0.2–0.4 μΩcm at 300 K. The T dependence of anomalous Hall conductivity $\sigma_{xy}^{A} = \rho_{yx}^{A}/\rho_{xx}^{2}$ is shown in Fig. 4.6b. The anomalous Hall conductivity is $\sim$1000 Ω^{-1}cm^{-1} at 300 K and almost independent of T above 100 K for all the samples, which indicates the dominant intrinsic contribution. With decreasing T below 100 K, on the other hand, the Hall resistivity shows different H dependence from that in the high-T region. The ρ_{yx} at 5.5 K was highlighted by blue dots in Fig. 4.7. For Ti- and V-doped Fe, the anomalous Hall term at 5.5 K is negative, but for Cr-doped one, it becomes to show large value of positive sign. For Mn-, Co-, Ni-, and Cu-doped Fe, the anomalous Hall term at 5.5 K enhances in positive direction. For the comparison, we also show the Hall resistivity for Ge0.3 %-doped Fe in Fig. 4.7. For the slightly Ge-doped specimen, the anomalous term is dramatically suppressed and ρ_{yx} at 5.5 K shows almost H linear dependence up to 9 T, while the magnitude of ρ_{xx} and that of R_0 is almost same for Ni1 %-doped one. This big difference among impurity elements is a strong evidence of the skew scattering mechanism. Corresponding to the enhancement of ρ_{yx}^{A}, σ_{xy}^{A} is also enhanced due to the skew-scattering term below 100 K, as shown in Fig. 4.6b. Compared to Ge0.3 %-doped Fe, the skew scattering contribution seems to be large for Fe doped with 3*d* transition metal series. This indicates that the impurity 3*d* state

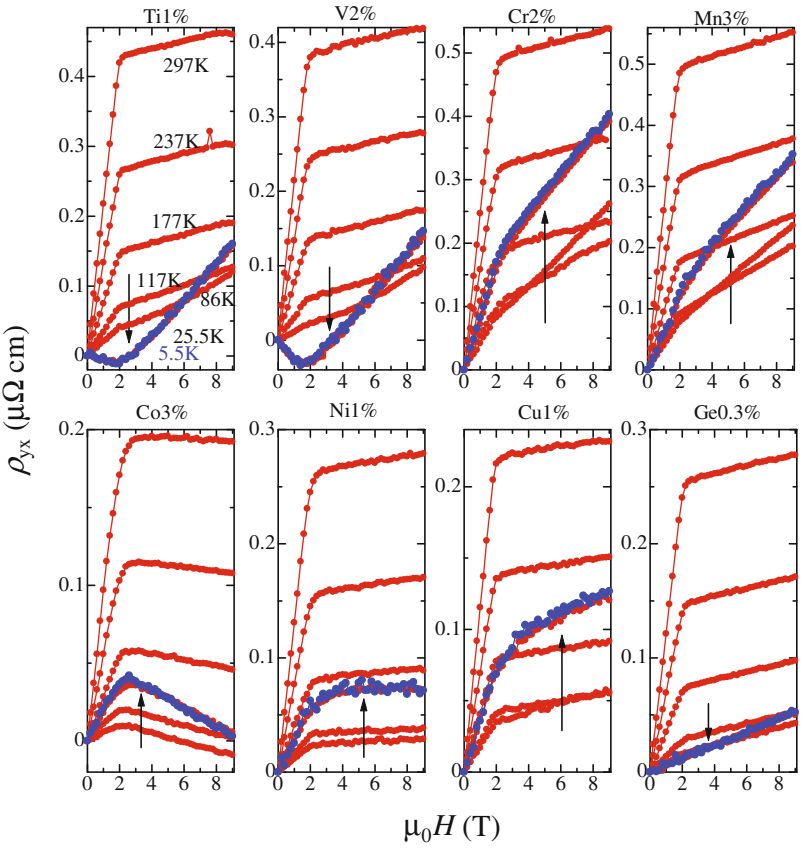

Fig. 4.7 H dependence of Hall resistivity (ρ_{yx}) for the Fe doped with impurity (Ti-Cu, or Ge). The *arrows* indicate the directions of the T variation of ρ_{yx} in the low-T region where the skew-scattering contribution is dominant

near the Fermi energy enhances the skew scattering contribution by resonant skews scattering mechanism.

We define the skew scattering contribution to anomalous Hall conductivity as done in the previous section by $\sigma_{xy}^{\text{skew}} = \sigma_{xy}^{A}(5.5\,\text{K}) - \sigma_{xy}^{A}(207\,\text{K})$. The skew scattering coefficient [$\equiv \sigma_{xy}^{\text{skew}}/\sigma_{xx}(5.5\,\text{K})$] is plotted in Fig. 4.6d as a function of impurity element. The skew scattering coefficient is considered to reflect the impurity potential. For Cr and Mn, the skew scattering coefficient is enhanced in a positive direction, while for Ti and V, the skew scattering contribution is negative for Ti and V. For the late elements, the skew scattering coefficient shows maximum for Ni and seems to decrease beyond Ni.

For the resonant skew scattering mechanism, the energy state, especially 3*d* state, of the impurity should be important. In [7], spin-polarized impurity-site-projected local density of states (DOS) of $Fe_{26}X_1$ (equivalent to a concentration of 3.7 at.%,

X = Sc − Zn) were investigated using FLAPW method based on GGA. With the substitution of Sc, the valence $3d$ electron is accommodated in the minority t_{2g} states. If Ti is added, its additional $3d$ electron occupies the minority t_{2g} states with e_g states shifting toward lower energy. For the impurity from Sc to Cr, all the $3d$ electrons occupy in the local minority spin bands to achieve charge neutrality and consequently to align the impurity magnetic moments in an opposite sense to the host magnetic moments. For Mn impurity, the majority e_g spin states also become occupied, while the local DOS is very sensitive to volume. The t_{2g} minority spin states are filled beyond Mn so that further additional $3d$ electrons are forced to enter the t_{2g} majority spin states and couple ferromagnetically to the host Fe atoms. Thus, the transition from antiferromagnetic to ferromagnetic coupling occurs when the virtual bound state in the majority spin band crosses E_F. The change of the impurity-state around E_F from minority to majority one may be related with the sign change of the skew-scattering term from negative to positive between V-doped and Cr-doped Fe.

The impurity energy state around the Fermi energy should affect Nernst effect sensitively, since the thermoelectric effect is sensitive to the impurity DOS around E_F according to the Mott relation [8, 9]. We show the H dependence of α_{xy}/T for Co3 % and Si0.3 % doped samples at various Ts in Fig. 4.8. At room T, α_{xy}/T is positive and the magnitude is almost same for Co-3 % and Si-0.3 % doped Fe. As T is decreased, the sign of the α_{xy}/T changes from positive to negative around 100 K. Since the sign of Nernst signal for electrons and holes is same, the sign change of α_{xy}/T indicates the emergence of the additional contribution, i.e. skew scattering contribution. For Co-3 % doped Fe, the α_{xy}/T is enhanced in a negative direction below 85 K, which corresponds to the onset T of intrinsic-extrinsic crossover, whereas such an enhancement is absent for Si-0.3 % doped Fe.

The anomalous Nernst terms are determined by the extrapolation of high-H data in Fig. 4.8 and plotted as a function of T in Fig. 4.9b. The anomalous term of α_{xy}/T at 5 K for Co-3 % doped Fe shows 16 times larger value in magnitude than for Si-0.3 % doped Fe. In the case of the anomalous term of σ_{xy}, the ratio of its magnitude between Co-3 % doped Fe and Si-0.3 % doped Fe is 4. In Nernst effect, the enhancement by the skew scattering becomes larger than in electrical Hall effect.

In the low-T region of metals, the Pertier conductivity is related with the electrical conductivity by the Mott formula

$$\alpha_{ij} = \frac{\pi^2}{3}\frac{k_B^2 T}{e}\left(\frac{\partial \sigma_{ij}}{\partial \varepsilon}\right)_{\varepsilon=\varepsilon_F} \quad (i, j) = (x, x), (x, y). \tag{4.2}$$

If the skew scattering term is dominant at 5.5 K, the σ_{xy} is proportional to σ_{xx}, i.e. $\sigma_{xy} \simeq \gamma\sigma_{xx}$, where γ is the skew scattering coefficient. Thus, α_{xy} is reduced to

$$\alpha_{xy}^A = \frac{\pi^2}{3}\frac{k_B^2 T}{e}\left(\frac{\partial \gamma}{\partial \epsilon}\right)_{\varepsilon=\varepsilon_F} + S_{xx}\sigma_{xy}^A. \tag{4.3}$$

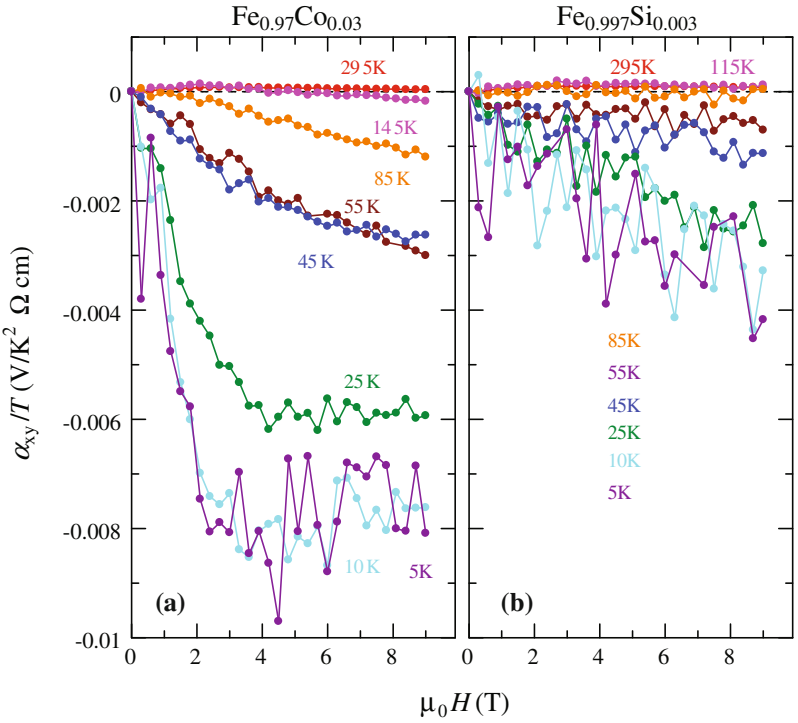

Fig. 4.8 H dependence of α_{xy}/T for **a** Co-3 % doped Fe and **b** Si-0.3 % doped Fe

For our samples, the second term is much smaller than the first term, and consequently α_{xy}^{A} is proportional to σ_{xx} as shown in Fig. 4.9c. The different slope between Co-doped Fe and Si-doped Fe is owed to the different $(\partial\gamma/\partial\varepsilon)_{\varepsilon=\varepsilon_F}$. The impurity $3d$ states near the Fermi energy should be an origin of the enhanced skew scattering contribution for Co-doped Fe. α_{xy} is more sensitive to the resonant skew scattering through the Mott relation ($\propto \partial\sigma_{xy}/\partial\varepsilon$) than electrical Hall effect.

4.2.2 Temperature Dependence of the Skew-Scattering-Induced Anomalous Hall Conductivity

As discussed above, the resonant skew scattering mechanism is the origin of the large skew-scattering term for Fe doped with $3d$ transition-metal series, while it seems not to be related with that in Si- or Ge- doped Fe. Next, we show different T-dependence of skew-scattering-induced anomalous Hall conductivity between Si- or Ge-doped Fe and the $3d$-transition-metal doped one, which also results from the different origin of skew scattering.

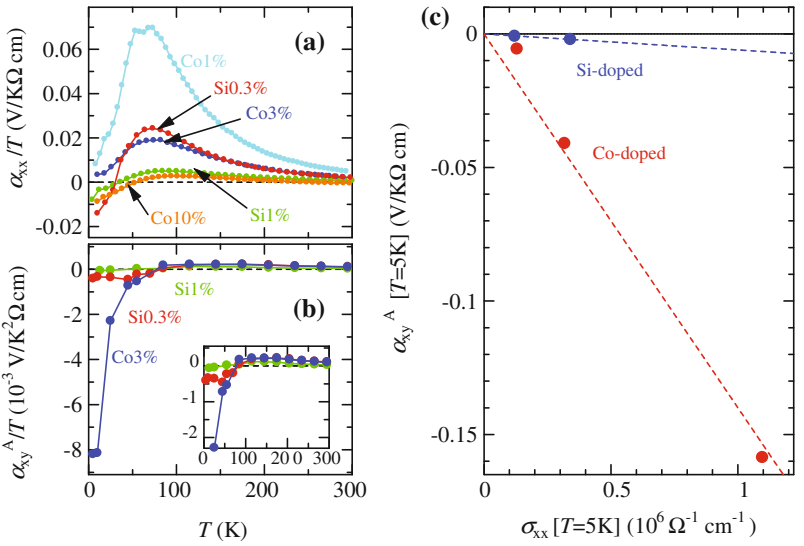

Fig. 4.9 T dependence of **a** α_{xx} divided by T and **b** the anomalous Hall term of α_{xy} divided by T for Si-doped and Co-doped Fe. **c** The anomalous term of α_{xy} as a function of σ_{xx} at 5 K for Co-doped (1, 3, and 10 %) Fe and Si-doped (0.3 and 1 %) Fe. The *dashed lines* are guides to the eyes

Let us investigate the skew scattering contribution to Hall effect for Fe doped with Si, Ge, or Sn, which belongs to the same group in the periodic table. In Fig. 4.10a, we show the resistivities for Si-doped (0.3, 0.6, and 1 %), Ge-doped (0.3, 0.6, and 1 %), and Sn-doped (0.3 and 0.6 %) Fe. The residual resistivities increase linearly with increasing the doping content x, as shown in Fig. 4.10b. The residual resistivities of the specimens with the same x are almost same regardless of the impurity species.

We show the Hall resistivities of Si-, Ge-, and Sn-doped Fe with $x = 0.3$ % in Fig. 4.11. The Hall resistivities for them show almost same H-dependence down to 117 K reminiscent of the intrinsic mechanism. On the other hand, below 100 K, where the skew-scattering-induced anomalous Hall effect should be dominant, the H dependences become different among different impurity elements. At 5.5 K, the anomalous Hall term seems to be negative for the Si-doped sample, while that for the Ge-doped sample is almost zero. For the Sn-doped sample, the anomalous Hall term becomes positive. We show the T dependence of anomalous Hall conductivities of all the samples in Fig. 4.10c. Compared to Fe doped with 3d-transition metal impurities [Fig. 4.6b], the onset T of intrinsic to skew-scattering crossover ($\approx$100 K) is rather obscured for Si- or Ge-doped samples. For Sn-doped samples, the anomalous Hall conductivity is almost independent of T.

Recently, an experimental relation about T dependence of ρ_{yx}^A,

$$\rho_{yx}^A = \alpha\rho_0 + \beta{\rho_0}^2 + b{\rho_{xx}}^2 \tag{4.4}$$

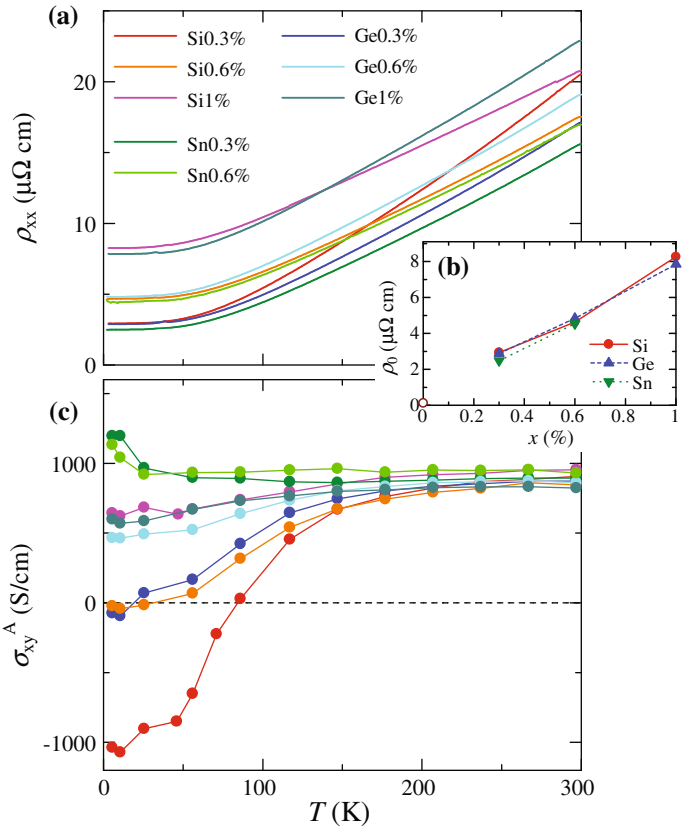

Fig. 4.10 **a** T dependence of the longitudinal resistivity ρ_{xx} for Si-, Ge-, and Sn-doped Fe. **b** The residual resistivity ρ_0 as a function of the doping concentration x. The *open circle* indicates the ρ_0 for the nominally-pure Fe. **c** T dependence of the anomalous Hall conductivity σ_{xy}^{A} for Si-, Ge-, and Sn-doped Fe

or

$$\sigma_{xy}^{A} = \alpha\rho_0\sigma_{xx}^{\ 2} + \beta{\rho_0}^2\sigma_{xx}^{\ 2} + b \tag{4.5}$$

was proposed for Fe thin film [10], where α, β, and b are assumed to be constant. The first and second terms in Eq. (4.4) are extrinsic contributions, i.e. skew scattering and side jump terms, respectively, where they assumed the extrinsic contributions result from only impurity scattering and independent of T. The third term in Eq. (4.4) is the term of intrinsic AHE which depends on T through $\rho_{xx}[T]^2$. For Si-, Ge-, and Sn-doped Fe, we investigate this relation between $\sigma_{xy}^{A}[T]$ and $\sigma_{xx}^{2}[T]$ [10] for our samples in Fig. 4.12. The σ_{xy}^{A} shows almost linear dependence on σ_{xx}^{2}, which means that the T dependence of anomalous Hall conductivity up to 300 K is well explained by the single relation of Eq. (4.5). By contrast, this relation is not valid for the impurities

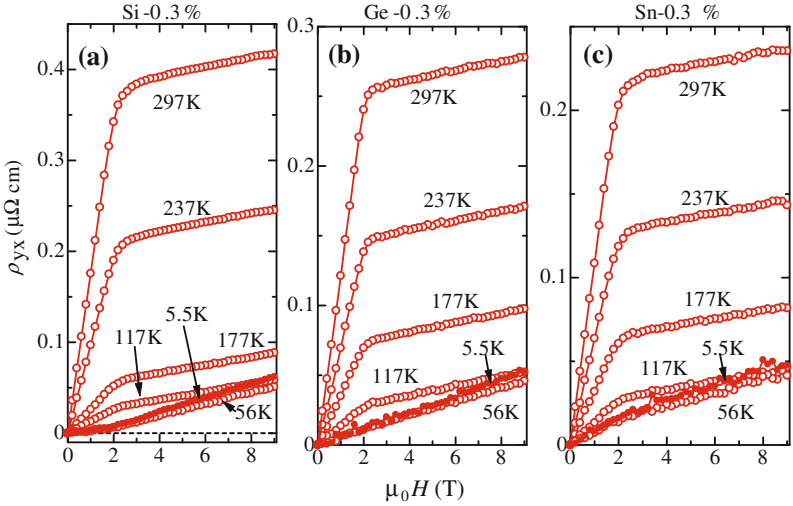

Fig. 4.11 H dependence of the Hall resistivity for Si0.3 %, Ge0.3 %, or Sn0.3 % doped Fe. The data at 5.5 K are shown by *solid circles*

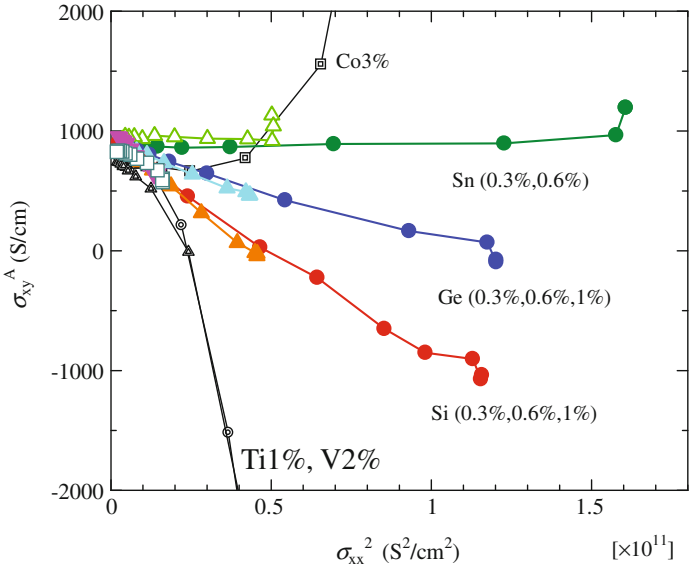

Fig. 4.12 $\sigma_{xx}^2[T]$-$\sigma_{xy}^A[T]$ relation proposed in [10] for Si-doped (0.3, 0.6, 1 %), Ge-doped (0.3, 0.6, 1 %), or Sn-doped (0.3, 0.6 %) Fe. For comparison, we also plot the data for Ti1 %, V2 %, or Co3 %-doped Fe

of transition metals from Ti to Cu, in which the resonant skew scattering induces the large $\sigma_{xy}^{\mathrm{skew}}$. For example, for Co-doped Fe, with decreasing T, the σ_{xy}^{A} suddenly enhances below 100 K in positive direction up to 5000 $\Omega^{-1}\mathrm{cm}^{-1}$ at 5.5 K, while it shows almost constant value $\approx$1000 $\Omega^{-1}\mathrm{cm}^{-1}$ above 100 K. Such a sudden change of σ_{xy}^{A} below 100 K cannot be explained only by the T variation of σ_{xx}^{2}.

From the relation between σ_{xy}^{A} and σ_{xx}^{2} shown in Fig. 4.12, we obtain the extrinsic contribution $a \equiv \alpha\rho_0 + \beta\rho_0^2$ as slopes and the intrinsic contribution b as ordinate intercepts for each specimen. The value of a slightly decreases with increasing impurity concentration x. The value of b, on the other hand, is 800–1000 $\Omega^{-1}\mathrm{cm}^{-1}$ and independent of the impurity elements and of the x value. Using the b value, we can calculate $\sigma_{xy}^{A}[5.5\,\mathrm{K}] - b$ which is equal to $\alpha\sigma_0 + \beta$ for Si-doped, Ge-doped, and Sn-doped Fe, respectively. If we assume that α and β do not change with the doping concentration, we can estimate the values of α and β for Si-, Ge-, and Sn-doped Fe, respectively. We show the T dependence of the estimated anomalous Hall conductivity induced by skew-scattering ($\sigma_{xy}^{\mathrm{skew}}$), side-jump ($\sigma_{xy}^{\mathrm{side-jump}}$), and intrinsic ($\sigma_{xy}^{\mathrm{int}}$) mechanisms for all the samples in Fig. 4.13. The summation of these terms ($\sigma_{xy}^{\mathrm{skew}} + \sigma_{xy}^{\mathrm{side-jump}} + \sigma_{xy}^{\mathrm{int}}$) (shown by open diamonds with pink lines) is well consistent with the observed σ_{xy}^{A} (shown by open triangles with orange lines) for Si- and Ge-doped specimens, but not for Sn-doped ones especially in the low-T region due to the error of the fit. As the impurity element is heavier, the side jump term $\beta{\rho_0}^2\sigma_{xx}^2$ decreases. Such a dependence on the strength of spin-orbit interaction has already been reported for FePd and FePt flims [11]. The ratio of the intrinsic σ_{xy} ($\equiv \sigma_{xy}^{\mathrm{int}}$) to the side-jump σ_{xy} ($\equiv \sigma_{xy}^{\mathrm{side-jump}}$) is expressed as [11, 12] $\sigma_{xy}^{\mathrm{int}}/\sigma_{xy}^{\mathrm{side-jump}} = (\Delta/vk_F)^2 + 1/4$, where k_F and Δ denote Fermi momentum and the strength of the spin-orbit interaction. Thus, for the larger strength of spin-orbit interaction, the side jump contribution becomes smaller. For the skew scattering mechanism, the stronger spin-orbit interaction of the impurity element is expected to generate the larger contribution. Since the skew scattering contribution $\alpha\rho_0\sigma_{xx}^2$ changes the sign from negative (Si-dope and Ge-dope) to positive (Sn-dope), the analysis on the magnitude of the skew scattering term is difficult.

Here, we need small modification in some analyses for Si-doped Fe presented before in the presence of the unignorable side-jump contribution. First, we are to note that our estimation (definition) of $\sigma_{xy}^{\mathrm{skew}} \equiv \sigma_{xy}^{A}[5.5\,\mathrm{K}] - \sigma_{xy}^{A}[207\,\mathrm{K}]$ used in the previous section is in fact not correct in case that the above relation [Eq. (4.5)] is applicable. When the T dependence of σ_{xy}^{A} obeys Eq. (4.5), $\sigma_{xy}^{A}[5.5\,\mathrm{K}] - \sigma_{xy}^{A}[207\,\mathrm{K}]$ is expressed as

$$\sigma_{xy}^{A}[5.5\,\mathrm{K}] - \sigma_{xy}^{A}[207\,\mathrm{K}] = (\alpha\sigma_0 + \beta)\left(1 - \frac{\sigma_{xx}[207\,\mathrm{K}]^2}{\sigma_0^2}\right), \tag{4.6}$$

where $\sigma_0 = \sigma_{xx}[5.5\,\mathrm{K}]$. Since $(\sigma_{xx}[207\,\mathrm{K}]/\sigma_0)^2 \sim 1/10$ for Si0.3 %-doped Fe, then

$$\sigma_{xy}^{\mathrm{skew}} = \sigma_{xy}^{A}[5.5\,\mathrm{K}] - \sigma_{xy}^{A}[207\,\mathrm{K}] \approx \alpha\sigma_0 + \beta. \tag{4.7}$$

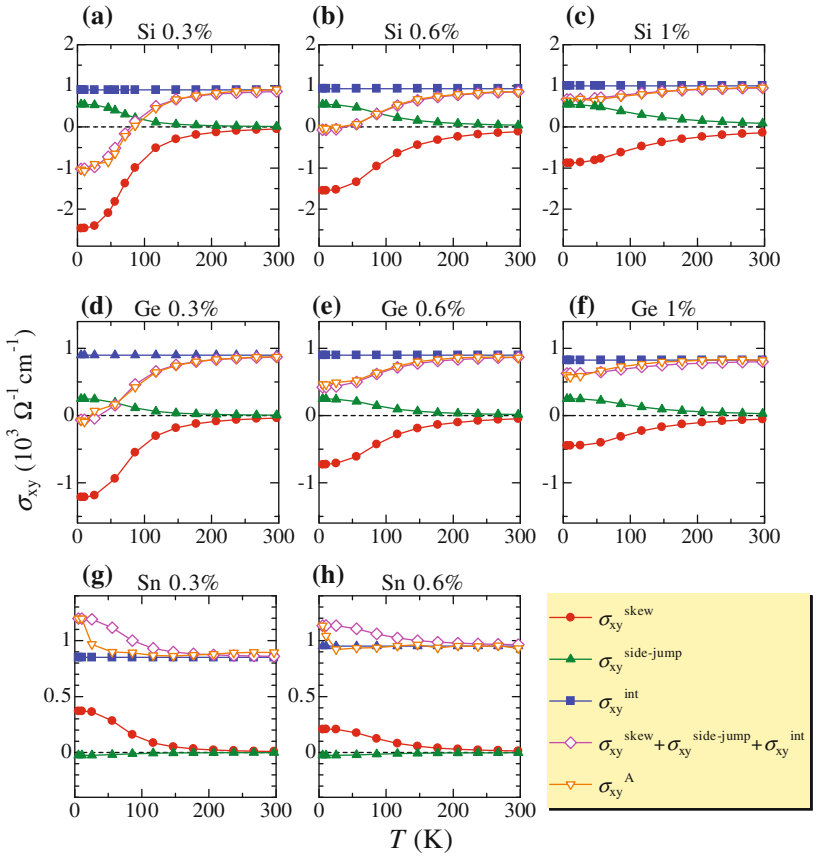

Fig. 4.13 T dependence of the estimated anomalous Hall conductivity induced by skew-scattering ($\sigma_{xy}^{\text{skew}}$), side-jump ($\sigma_{xy}^{\text{side-jump}}$), and intrinsic ($\sigma_{xy}^{\text{int}}$) mechanisms

Thus, the side-jump term β appears as the ordinate intercept in relation of $\sigma_{xy}^{\text{skew}}$ versus σ_0 in Fig. 4.2a. For Si-doped Fe, the fitting curve (dotted line) should be straight line not from the origin $(\sigma_0, \sigma_{xy}^{\text{skew}}) = (0, 0)$ but from $(0, \beta)$ with $\beta \simeq 500\,\Omega^{-1}\text{cm}^{-1}$. By contrast, for Co-doped (and other $3d$-transition-metal-doped) Fe, the side-jump term can be neglected compared to the giant skew-scattering term.

In the discussion on the Lorenz ratio in the previous section, the side-jump contribution should be added besides skew-scattering one into the dissipative current for Si-doped Fe. The extrinsic contribution (skew scattering + side jump) is $\propto (\alpha\rho_0 + \beta\rho_0^2)\sigma_{xx}^2 \propto \tau^2$ while the intrinsic contribution is $\propto \tau^0$ (see also Fig. 4.5). Now we can explain the different T dependence of L_{xy}^A between Si0.3 %-doped and Co3 %-doped Fe in the low T region where the extrinsic contribution is dominant [Fig. 4.4b, c]. For Si0.3 %-doped Fe [Fig. 4.4c], $L_{xy}^A = L_{xy}^N$ is satisfied below 50 K, while $L_{xy}^A \neq L_{xy}^N$ for Co3 %-doped one [Fig. 4.4b]. Since the T dependence of

$\sigma_{xy}^{\text{extrinsic}}$ for Si0.3 %-doped Fe is $\propto \tau^2$ as described above and that of $\sigma_{xy}^N = R_0 \sigma_{xx}^2 H$ is also $\propto \tau^2$, L_{xy}^N and L_{xy}^A should show almost similar T-dependence, which is consistent with the experimental results. On the other hand, for Co3 %-doped Fe, in which the above relation of Eq. (4.5) is not valid, the T dependences of L_{xy}^N and L_{xy}^A are no longer same ($L_{xy}^N \neq L_{xy}^A$), as shown in Fig. 4.4b.

4.3 Summary

The major results in this chapter are summarized as follows:

- We have successfully identified the skew scattering contribution to the electrical Hall conductivity as well as thermal one for iron metals with controlled doping of impurity.
- In the low-T region below 100 K, the Lorenz ratio for anomalous Hall current is much smaller than L_0 or even negative. These features result from the predominant contribution of the scattering-dependent Hall conductivity induced by the skew scattering (and side-jump for Si-doped Fe) in the low-T ($<$100 K) region, in addition to the almost scattering-free intrinsic anomalous Hall conductivity.
- For Fe doped with a 3d-transition metal impurity, the resonant skew scattering mechanism shows large anomalous Hall effect below 100 K. On the other hand, for Si, Ge, or Sn doped Fe, the resonant mechanism is not feasible and the skew-scattering-induced anomalous Hall conductivity is much smaller than that for Fe doped with a 3d-transition metal impurity. The T dependence of ρ_{yx}^A for Fe doped with Si-, Ge-, or Sn-doped Fe is well explained by an empirical formula on the assumption that the extrinsic anomalous Hall resistivity does not depend on T.

References

1. Y. Shiomi, Y. Onose, Y. Tokura, Phys. Rev. **B 79**, 100404(R) (2009)
2. S. Onoda, N. Sugimoto, N. Nagaosa, Phys. Rev. Lett. **97**, 126602 (2006)
3. S. Onoda, N. Sugimoto, N. Nagaosa, Phy. Rev. **B 77**, 165103 (2008)
4. J. Smit, Physica **21**, 877 (1955)
5. J. Smit, Physica **24**, 39 (1958)
6. A. Fert, O. Jaoul, Phys. Rev. Lett. **28**, 303 (1972)
7. G. Rahman, I.G. Kim, H.K.D.H. Bhadeshina, A.J. Freeman, Phys. Rev. **B 81**, 184423 (2010)
8. J.P. Heremans, V. Jovovic, E.S. Toberer, A. Saramat, K. Kurosaki, A. Charoenphakdee, S. Yamanaka, G.J. Snyder, Scienc **321**, 554 (2008)
9. J.H. Lee, J. Wu, J.C. Grossman, Phys. Rev. Lett. **104**, 016602 (2010)
10. Y. Tian, L. Ye, X. Jin, Phys. Rev. Lett. **103**, 087206 (2009)
11. K.M. Seemann, Y. Mokrousov, A. Aziz, J. Miguel, F. Kronast, W. Kuch, M.G. Blamire, A.T. Hindmarch, B.J. Hickey, I. Souza, C.H. Marrows, Phys. Rev. Lett. **104**, 076402 (2010)
12. N.A. Synitsyn, A.H. MacDonald, T. Jungwirth, V.K. Dugaev, J. Sinova, Phys. Rev. **B 75**, 045315 (2007)

Chapter 5
Topological Hall Effect in Itinerant Helimagnets

Abstract In this chapter, we focus on the topological Hall effect in itinerant helimagnets. As described in Chap. 1, there have been few helimagnets which show topological Hall effect except for Skyrmion lattice phases of chiral helimagnets (e.g. MnSi and MnGe). This is because the total scalar spin chirality summed over the whole lattice sites often becomes zero due to structural symmetry, although the non-coplanar spin configuration is generally realized in helical magnets under applied H. In the first and second sections of this chapter, we report two new examples of helimagnets in which the scalar spin chirality does not cancel out owing to the modulation of spin structure by DM interaction and thus topological Hall effect occurs. In the third section, we investigate the topological Hall effects by heat current, i.e. topological thermal Hall effect and topological Nernst effect, for MnGe. In contrast to the cases of MnSi and (Fe,Co)Si, the Skyrmion lattice phase of MnGe has been considered to prevail in wide temperature and magnetic-field window. This enables us to examine thoroughly the topological Hall effects by heat current in the Skyrmion lattice phase.

Keywords Topological Hall effect · Itinerant helimagnet · Scalar spin chirality · Dzyaloshinsky-Moriya interaction · Berry phase of electrons

5.1 Topological Hall Effect in $Fe_{1.3}Sb$

In the case of the triangular lattice with three-sublattice spin order (e.g. 120°-spin structure), the whole scalar spin chirality cancels out and the contribution to Hall effect is not expected [1, 2]. Recently, however, in a triangular-lattice antiferromagnet $PdCrO_2$ where Cr^{3+} spins order with a 120°-structure below $T_N = 37$ K, an unconventional Hall effect was observed under H applied parallel to the c axis below $T^* \sim 20$ K that is noticeably lower than T_N [3]. It was speculated in [3] that the spin structure would change so as to have a finite scalar spin chirality below T^* under

Y. Shiomi, *Anomalous and Topological Hall Effects in Itinerant Magnets*,
Springer Theses, DOI: 10.1007/978-4-431-54361-9_5, © Springer Japan 2013

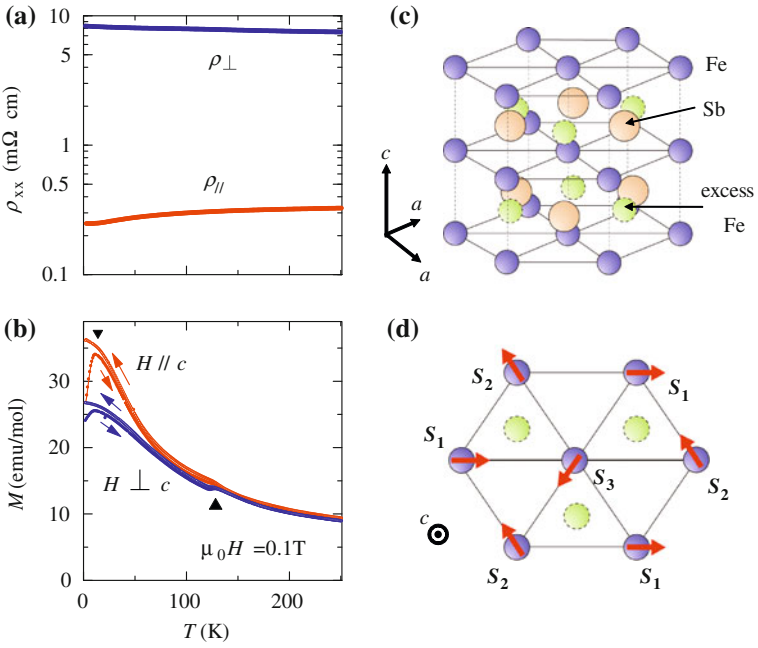

Fig. 5.1 **a** Temperature dependence of the in-plane and out-of-plane resistivities, $\rho_{||}$ and $\rho_\perp$, for $Fe_{1.3}Sb$ [4]. **b** T dependence of the magnetization (M) in external magnetic field (H) parallel or perpendicular to the c axis [4]. Two *triangles* indicate the ordering temperatures of the in-plane Fe(l) spins (T_N) and the interstitial-Fe(i) spins, respectively. **c** Schematic view of the crystal structure of $Fe_{1+\delta}Sb$ [4]. Fe(i) atoms, whose concentration is δ, randomly occupy the sites shown by *dotted circles*. **d** *Top view* of the Fe(l) and Fe(i) sites where the (*red*) *arrows* indicate the directions of the Fe(l) spins in the 120°-spin structure below T_N [4]

H applied parallel to the spin-spiral plane, although such a subtle spin-structural modification could not be proved. In this section, we report on a more explicit case of the spin-chirality induced Hall effect on the triangular-lattice magnet $Fe_{1+\delta}Sb$, in which we could identify that Dzyaloshinsky-Moriya (DM) interaction modifies the spin structure in the spin clusters associated with the interstitial-Fe spins to generate the net scalar spin chirality. The DM-interaction mediated topological Hall effect as proposed here may be found in many of triangular-lattice magnets with modified 120°-spin structures.

The crystal structure of $Fe_{1+\delta}Sb$ (NiAs-type) is depicted in Fig. 5.1c. Fe and Sb triangular nets are alternately stacked along the c axis, while hosting the interstitial-Fe [Fe(i)] atoms (content δ). The dotted circles in Fig. 5.1c indicate the possible positions which can be randomly occupied by the Fe(i) atoms; these positions correspond to the apex connecting the upper and lower adjacent-lattice Fe-triads. $Fe_{1+\delta}Sb$ is always off-stoichiometric ($\delta \neq 0$) and is known to be stabilized for $0.08 < \delta < 0.35$ [5]. Spins of lattice-Fe [Fe(l)] order in a 120°-spin structure within the c plane and ferromagnetically along the c axis below T_N (Fig. 5.1d), as determined by the neutron

diffraction measurement for $Fe_{1.14}Sb$ [6]. The T_N value obtained from the Mössbauer spectroscopy and susceptibility data decreases from 200 to 50 K with increasing Fe(i) content δ [5]. Spins of Fe(i) do not order at T_N but freeze in the much lower-T region than T_N with the thermal hysteresis in M-T curve (see Fig. 5.1b) [7]. According to the powder neutron diffraction measurement [6], the 120°-spin structure of the Fe(l) spins is still retained in such a low-T region independently of the spin glass transition of the Fe(i) spins. It is anticipated that the long range 120°-spin order and the spin-glass (micto-glass) state around Fe(i) coexist at the lowest T [7]. Although the magnetic properties have been intensively investigated for $Fe_{1+\delta}Sb$ as described above, little attention has been paid to the transport properties. The development of the local magnetic order on Fe(i) sites is expected to affect the net scalar spin chirality of the system which would be totally canceled out in the 120°-spin structure without Fe(i). We show here that the topological Hall resistivity as induced by the scalar spin chirality is observed in external H applied parallel to the c axis in the low-T region where the chiral magnetic clusters are built up around the Fe(i) sites.

Figure 5.1a shows the T dependence of resistivity measured within and out of the c plane ($\rho_{||}$ and $\rho_{\perp}$ respectively). $\rho_{||}$ slightly decreases with decreasing T, but the residual resistance ratio to the room-temperature value is less than 2, suggesting the appreciable effect of disorder by randomly occupying Fe(i). On the other hand, $\rho_{\perp}$ is one order of magnitude larger than $\rho_{||}$ and slightly increases with decreasing T, indicating the quasi-two-dimensional transport characteristic of the layered lattice structure shown in Fig. 5.1c. We show in Fig. 5.1b the T dependence of M measured in H parallel or perpendicular to the c axis. A transition is observed around 130 K, below which Fe(l) spins order in the in-plane 120° spin structure (Fig. 5.1d) [8]. According to the previous study [5], the T_N value corresponds to that of $\delta \sim 0.25$, which is slightly smaller than the nominal value ($\delta \sim 0.3$) in the present crystal. The decrease of M upon T_N in $H \perp c$ is larger than that in $H||c$. The observed anisotropy is consistent with the magnetic transition to the in-plane 120°-spin order. Since the Fe(i) spins do not order magnetically at T_N, the Curie-like increase of M persists below T_N as observed. Around 10 K, M shows the maximum accompanying the large thermal hysteresis both for $H||c$ and $H \perp c$. In the present sample, the spin glass transition relevant to the Fe(i) spins seems to occur around 10 K, which is lower than the value reported in literature (∼30 K) [6, 7].

In Fig. 5.2a, we show the magnetoresistance below 90 K. The magnetoresistance is as small as 2 % even at 2 K and 14 T. Figure 5.2b shows the $H(||c)$ dependence of M at several temperatures. The slope of M-H curve increases with decreasing T, but M does not saturate up to 14 T even at 2 K; the M at 14 T is about 0.35 μ_B/f.u., which is far smaller than the full moment value (∼0.9 μ_B/f.u.) of Fe determined by neutron diffraction measurement [6]. Since the magnetization of Fe(l) (M^l) would not change largely below T_N, the increase of M below T_N should be attributed to the increase in the magnetization of Fe(i) (M^i). For the latter use in the analysis of the Hall resistivity, we estimated the M^l value (assumed to be T-independent) by $M^l = \chi^l H$, where the T-independent susceptibility for Fe(l) spins (χ^l) is obtained by the subtraction of the Fe(i) component $\propto 1/(T + T_0)$ from M below T_N in Fig. 5.1b. (Here, the fitted Curie-Weiss temperature T_0 is close to $T_g \sim 10$ K.) Thus, the obtained M^l

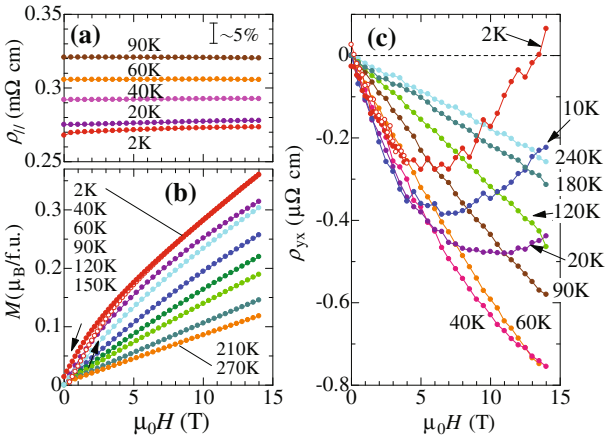

Fig. 5.2 Magnetic-field (H) dependence of (**a**) the in-plane resistivity ($\rho_{||}$), (**b**) the magnetization (M), and (**c**) the Hall resistivity ρ_{yx} under $H||c$ at several temperatures [4]. Small hysteresis is observed in M and ρ_{yx} at 2 K, as seen as the difference between *closed* and *open circles*.

value below T_N based on this assumption is H-linear by definition, and reaches, for example, 0.17 μ_B/f.u. at 14 T. The observed non-linear H-dependence of M in the low-T region is ascribed to M^i ($\equiv M - M^l$ at every temperature below 120 K). At 2 K, the hysteresis is observed in the M-H curve up to around 5 T, perhaps reflecting the freezing of Fe(i) spins or micto-glass state.

Figure 5.2c shows the Hall resistivity (ρ_{yx}) measured in $H||c$. ρ_{yx} is negative and almost linear with H above 60 K. The roughly estimated carrier density ($\equiv -1/R_0 e$, where R_0 is normal Hall coefficient) and mobility ($\equiv |R_0|/\rho_{||}$) above T_N are 1.2×10^{23}/cm^3 and 0.16 cm^2/Vs, respectively. Since the magnitude of ρ_{yx} increases with decreasing T in proportional to M, the contribution from the anomalous Hall effect as induced by the spin-orbit interaction seems to be dominant below T_N. Below 40 K, ρ_{yx} shows an almost linear H-dependence in the low-H region, but tends to curve positively in the high-H region. Below 20 K, ρ_{yx} increases toward a positive direction in high-H region, and at 2 K shows even a sign-reversal around 13 T, while the magnetoresistance remains as small as a few percent. Judging from the T region in which the anomaly takes place, the order of the Fe(i) spins affects the anomalous Hall effect, whereas no distinct change in the H dependence of M nor $\rho_{||}$ is observed.

The Hall effect in a magnet is generally described by the empirical formula $\rho_{yx} = R_0(\mu_0 H) + R_s M$, where R_0 and R_s are normal and anomalous Hall coefficients, respectively. For the present material, the contributions from the moments of Fe(l) and Fe(i) should be distinguished, i.e. $\rho_{yx} = R_0(\mu_0 H) + R_s^i M^i + R_s^l M^l$ (R_s^i and R_s^l are R_s for Fe(i) and Fe(l), respectively.). As shown in Fig. 5.3a, b, c, and d, we can fit nicely the experimental data above 40 K using this relation with constant values of R_0, R_s^l, and R_s^i. The obtained values of R_0, R_s^l, and R_s^i are -4.9×10^{-9} Ωcm/T, -1.07×10^{-6} Ωcm/(μ_B/f.u.), and -3.59×10^{-6} Ωcm/(μ_B/f.u.), respectively. The good agreement between ρ_{yx} and the fitting curve with use of these parameters above

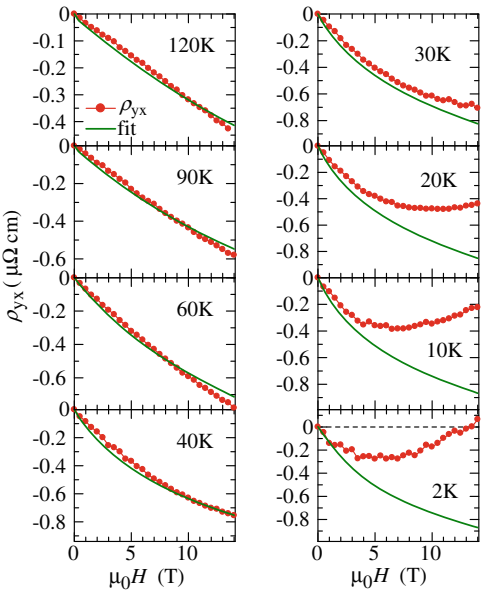

Fig. 5.3 **a–h** Fitting (*solid lines*) of the Hall resistivity ρ_{yx} with the relation of $\rho_{yx} = R_0(\mu_0 H) + R_s^i M^i + R_s^l M^l$ below 120 K [4]. Fitting parameters R_0, R_s^i, and R_s^l are assumed to be T-independent (see text)

40 K (Fig. 5.3a, b, c and d) indicates that the Hall effect in the triangular lattice with an in-plane 120°-spin order can be understood within the framework of the conventional anomalous Hall effect. Below 30 K, by contrast, ρ_{yx} deviates from the fitting curve as shown in Fig. 5.3e, f, g and h. (At 2 K, we used the average values of M^i and ρ_{yx} in the hysteresis region for the fitting.) To explain such a large deviation from the conventional fit, one may consider the possibility that the R_s^i value changes with the ordering of the Fe(i) spins around 10 K. However, a dramatic change of R_s^i, including a sign-reversal in H and steep H- and T-dependences, would be necessary for the explanation of the H dependence of ρ_{yx}; this is highly unlikely. Moreover, R_0 and R_s^l show negative signs above 40 K and these values could be hardly changed by the ordering of the Fe(i) spins. It was confirmed that the different estimation of M^l and M^i least affects the emergent deviation below 30 K, although does slightly the accuracy of the fitting curve above 40 K. Thus, the difference between ρ_{yx} and the fitting curve below 30 K is not explained by the conventional formula and regarded as an unconventional term, which we assign here to the spin chirality mechanism.

We estimate the chirality-driven ρ_{yx} (ρ_{yx}^{χ}) as the deviation from the conventional normal and anomalous terms (see Fig. 5.3) and plot its H dependence below 40 K in Fig. 5.4a. ρ_{yx}^{χ} at 14 T is almost zero at 40 K, but below 30 K increases with decreasing T, as shown in the inset to Fig. 5.4a. The onset T for the H (14 T)-induced spin chirality is tangibly higher than the transition T of the Fe(i) spins (∼10 K), which indicates the spin glass state is not directly related with the spin chiraliy mechanism. At 2 K, $\sigma_{xy}^{\chi} = \rho_{yx}^{\chi}/\rho_{||}^2$ is $\sim 15\,\Omega^{-1}\mathrm{cm}^{-1}$ at 14 T. This value is as large as σ_{xy}^{χ} observed in $Nd_2Mo_2O_7$, in which the scalar spin chirality plays a dominant role due to the tilting (∼4°) of the Mo spins from the ferromagnetic alignment [9]. The H-dependence of ρ_{yx}^{χ} is approximately linear or slightly superlinear.

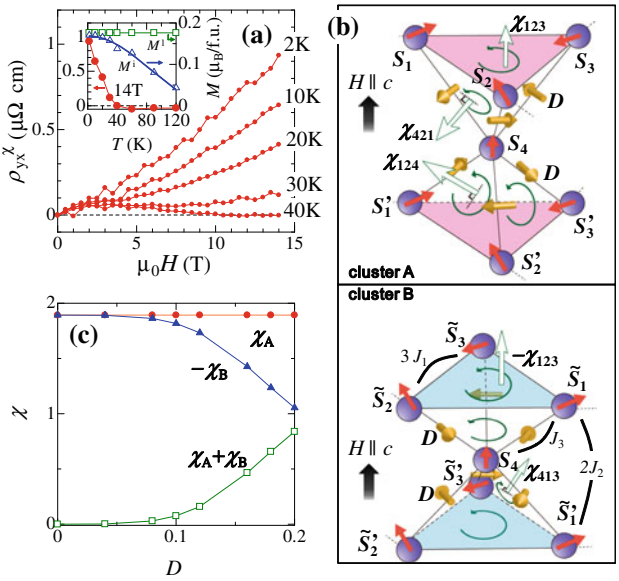

Fig. 5.4 **a** Magnetic-field (H) dependence of the chirality-driven Hall resistivity, ρ_{yx}^{χ}, estimated from Fig. 5.3 [4]. Inset shows temperature (T) dependence of ρ_{yx}^{χ}, M^i, and M^l at 14 T. **b** Schematic views of two types of the heptamer spin-clusters, A and B, consisting of one Fe(i) spin and two Fe(l)-spin triads above and below it under $H||c$ at low temperatures [4]. Here the Fe(i) spins are assumed to be well H-polarized. Vectors normal to the faces as described by (*green*) *open arrows* denote directions of the scalar spin chirality from the respective triangle faces of the heptamer. The (*yellow*) *arrows* indicate directions of the DM vectors $\boldsymbol{D}_{ij}$ on the nearest-neighbor Fe(l)-Fe(i) bonds. **c** Scalar spin chiralities χ_A and χ_B of the cluster A and B, and their sum $\chi_A + \chi_B$ as functions of D (normalized by the in-plane interaction J_1) obtained by a numerical calculation (see text) [4]

In the relatively-high-T region below T_N, the Fe(i) spins are almost disordered due to thermal agitation, and the spin order occurs only as the in-plane 120°-spin structure on the Fe(l) triangular lattices as shown in Fig. 5.1d. In this situation, the net scalar spin chirality should cancel out in $\boldsymbol{k}$-space as suggested theoretically [1, 2], and, thus, no additional Hall effect is expected, being consistent with our observation. On the other hand, in the low-T region where the Fe(i) spins tend to be polarized by external H (M^i(14 T) is shown in Fig. 5.4a), there appear some heptamer spin-clusters in which one Fe(i) spin couples to two Fe(l)-triangles with 120°-spin orders located above and below the Fe(i). Because of the alternate stacking of Fe(i) and Sb atoms, there are two kinds of the heptamer clusters with the equal population, A and B, as illustrated in Fig. 5.4b. The total scalar spin chirality χ_A (χ_B) for the heptamer cluster A (B) can be calculated as a sum of vectors normal to the respective triangular faces as exemplified by (green) open arrows, whose lengths are χ_{ijk}. When only the symmetric exchange ($J_{ij}\boldsymbol{S}_i \cdot \boldsymbol{S}_j$) works among the Fe spins, the relation $\boldsymbol{S}_m = \boldsymbol{S}'_m = \tilde{\boldsymbol{S}}_m = \tilde{\boldsymbol{S}}'_m$ holds for $m = 1, 2$, and 3 even under $H \parallel c$. Consequently χ_A coincides with $-\chi_B$, both of which are given by $(2/3)(\chi_{124} + \chi_{234} + \chi_{314}) + 2\chi_{123}$.

This is because the cluster B is a mirror image of the cluster A, and each face of the heptamer gives an opposite contribution between A and B. For example, each of the basal and top Fe(l) triads gives χ_{123} for the cluster A, while $-\chi_{123}$ for the cluster B. The perfect cancelation of χ_A and χ_B indicates that we need more ingredients to account for the observed topological Hall effect.

Incorporation of the DM interaction, $\boldsymbol{D}_{ij} \cdot (\boldsymbol{S}_i \times \boldsymbol{S}_j)$, changes the situation dramatically. The DM vectors $\boldsymbol{D}_{ij}$ are locally defined on the bonds connecting two spins, and become finite when the local inversion symmetry is absent. Because of the absence of inversion symmetry on the Fe(i)-Fe(l) bonds, there are finite DM vectors $\boldsymbol{D}_{ij}$ whose directions are illustrated by (yellow) arrows in Fig. 5.4b. The DM interaction causes canting of the Fe(l) spins and thus modifies the spin structure. Since the vectors $\boldsymbol{D}_{ij}$ on the upper Fe(i)-Fe(l) bonds are opposite to those on the lower Fe(i)-Fe(l) bonds in each heptamer, the spin canting becomes inequivalent between the basal and top triangle planes, i.e., $\boldsymbol{S}_m \neq \boldsymbol{S}'_m$ and $\tilde{\boldsymbol{S}}_m \neq \tilde{\boldsymbol{S}}'_m$. Moreover the Fe(l) spins cant in a different manner between the clusters A and B. For the Fe(l) triads of the cluster A, directions of the three Fe(l) spins are modified while keeping the original chirality for the case without DM interaction, whereas for those of the cluster B the spin canting alters the chirality value (see Appendix B). Owing to the inequivalent modifications of the spin structure, the two contributions χ_A and χ_B no longer cancel out, and the net scalar spin chirality proportional to $\chi_A + \chi_B$ becomes nonzero, which works as an origin of the observed topological Hall effect.

The above discussion is confirmed by numerical simulations of a classical Heisenberg model on the heptamer spin clusters. In this model, the spins are treated as classical vectors whose norms are set to be unity. The model contains the symmetric exchange interactions, DM interaction, magnetic anisotropy, and Zeeman coupling. For the symmetric exchange interactions, we consider antiferromagnetic $3J_1$ between the in-plane Fe(l)-Fe(l) spin pairs, ferromagnetic $2J_2$ between the out-of-plane Fe(l)-Fe(l) spin pairs, and weak antiferromagnetic J_3 between the Fe(i)-Fe(l) spin pairs (see Fig. 5.4b). Since the Fe(l) spins in the 120° order direct along the in-plane bonds at $H = 0$, we includes the following anisotropy term, $-A\sum_i[(\boldsymbol{S}_i \cdot \boldsymbol{l})^2 + (\boldsymbol{S}_i \cdot \boldsymbol{m})^2 + (\boldsymbol{S}_i \cdot \boldsymbol{n})^2]$ where $\boldsymbol{l}$ and $\boldsymbol{m}$ are the Bravis vectors of the triangular lattice and $\boldsymbol{n} = \boldsymbol{l} + \boldsymbol{m}$. The Zeeman couping is given by $-H\sum_i S_{zi}$. For the parameter values to simulate the low-T case, we take $J_1 = 1$, $J_2 = -0.5$, $J_3 = 0.2$, $A = 0.2$, and $H = 0.1$. We numerically search the lowest-energy spin cofigurations, and calculate the scalar spin chiralities χ_A and χ_B as functions of strength of the DM vector $|\boldsymbol{D}_{ij}| = D$ as shown in Fig. 5.4c. In the absence of the DM interaction ($D = 0$), χ_A and $-\chi_B$ are equivalent. As D increases, $-\chi_B$ decreases whereas χ_A does not change, which results in finite $\chi_A + \chi_B$. In reality, for D to be effective to generate the spin chirality (empirically, $D/J = 0.1 \sim 0.2$), the averaged moment value of Fe(i) spin and the canting angle of the in-plane Fe(l) spin moments by DM interaction are essential; the former is mainly determined by magnetic field, while the latter by D/J. This may explain the low temperature (30 K) and the nearly H-linear evolutions of topological Hall effect as observed.

The D dependence of the scalar spin chirality for cluster A and B can also be estimated analytically. We here set simply the $\boldsymbol{S}_1$, $\boldsymbol{S}_2$, $\boldsymbol{S}_3$, and $\boldsymbol{S}_4$ spins by

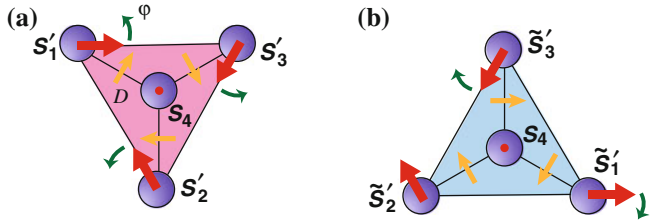

Fig. 5.5 Rotation direction of the Fe(l) spins on the bottom face of (**a**) cluster A and (**b**) cluster B by DM interaction

$$\boldsymbol{S}_1 = (S_{||}, 0, S_{\perp}) \tag{5.1}$$
$$\boldsymbol{S}_2 = (S_{||}\cos(2\pi/3), S_{||}\sin(2\pi/3), S_{\perp}) \tag{5.2}$$
$$\boldsymbol{S}_3 = (S_{||}\cos(4\pi/3), S_{||}\sin(4\pi/3), S_{\perp}) \tag{5.3}$$
$$\boldsymbol{S}_4 = (0, 0, S_i), \tag{5.4}$$

where we define $S_{||} = S_l \cos\alpha$ and $S_{\perp} = S_l \sin\alpha$ using the tilting angle (α) of the Fe(l) spin (S_l) from the c plane by external magnetic field along c axis. The in-c-plane spin rotation of Fe(l) spins on the bottom face of the cluster by DM interaction is shown by the angle φ in Fig. 5.5. As described before, the spin modulation between cluster A and B is different each other. By also considering the spin modulation on the top face, we calculate the spin chirality for cluster A and B. The result is

$$\chi_A = 3\sqrt{3}S_i S_{||}^2 \cos\theta + 3\sqrt{3}S_{||}^2 S_{\perp} \tag{5.5}$$
$$\chi_B = -\sqrt{3}S_i S_{||}^2 \cos\theta(1 + 2\cos\phi) - \sqrt{3}S_{||}^2 S_{\perp}(1 + 2\cos\phi), \tag{5.6}$$

where θ is the acute angle between the vector normal to a side face of cluster and c axis. If $\varphi = 0$, $\chi_A = -\chi_B$. As φ is increased from 0, $\chi_A + \chi_B$ increases from 0 according to $(1 - \cos\varphi)$, which is consistent with the numerical calculation in Fig. 5.4c.

At last, we show, in Fig. 5.6, δ (concentration of interstitial-Fe) dependence of Hall resistivity measured under $H||c$ at 2 K. The Hall resistivity shows a positive value for the compound with low δ value, but it becomes negative for those with $\delta \geq 0.2$. The topological Hall term, which is indicated by the upturn in high magnetic-field region, becomes smaller with decreasing δ value. This is consistent with our scalar-spin-chirality mechanism described above.

5.2 Topological Hall Effect in MnP

Manganese phosphide (MnP) is one of the typical itinerant helimagnets and its magnetic properties have been intensively investigated for these decades [10–15], but the complete understanding is yet to be attained [16, 17]. MnP has an orthorhombic

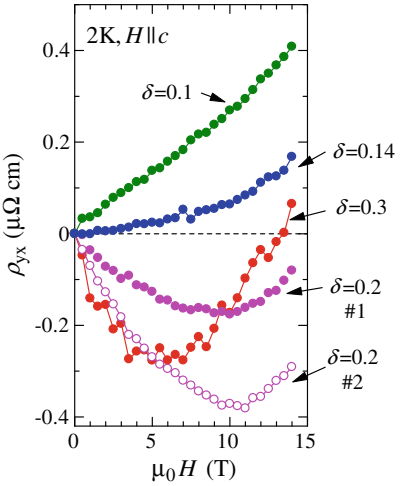

Fig. 5.6 Magnetic field dependence of the Hall resistivity in $H||c$ at 2 K for $Fe_{1+\delta}Sb$ with various δ values (concentration of interstitial-Fe)

crystal structure ($B31$), which can be viewed as a distorted form of the hexagonal NiAs-type structure. The lattice constants ($a_0 > b_0 > c_0$) are $a_0 = 5.918$ Å, $b_0 = 5.258$ Å, and $c_0 = 3.172$ Å [18]. The unit cell contains four Mn atoms and four P atoms. As shown in Fig. 5.7a, Mn zigzag chains within the ab plane run along the b axis. At zero field, three magnetically ordered states of the Mn spins have been reported [10–12]; two ferromagnetic (F) phases existing between $T_C = 291$ K and $T^* = 282$ K and between T^* and $T_h = 47$ K, and helimagnetic (H) phase below T_h. In the first-emerging F phase ($T^* < T < T_C$), the Mn spins are aligned along the c axis [13], while they slightly reorient toward b axis below T^* [11]. In the second F phase below T^*, the small hysteresis of weak ferromagnetism along b axis has been observed in a low-H region below 1 mT [12], which is so small that this weak ferromagnetism was missed in old reports [10]. In the H phase below T_h, old literature reported that the Mn spins were aligned collinearly within the bc plane, and formed screw rotation along the a axis [14, 15]. The magnetic propagation vector is $(\delta, 0, 0)$ with $\delta = 0.11$–0.12, which indicates the period of the spiral spin structure is about $9a_0$ [14, 15]. Recently, however, tiny modulation of the magnetic structure in zero field has been found also in the H phase; recent neutron diffraction study [12] has found a new magnetic reflection at $(\delta, 1, 0)$, the intensity of which is 70 times smaller than that of $(2 + \delta, 0, 0)$. This reflection indicates some modification of helical spin texture propagating toward a direction. The authors concluded that the helical plane, having been considered to be within bc plane, is slightly rotated ($\theta \sim 2$–$6°$) around the c axis to the a direction by the DM interaction, as shown in Fig. 5.7a [12]. The small a component is antiferromagnetic along the b axis, but ferromagnetic along the c axis. While this slight modulation of helical spin structure has been reported only in zero field, the similar modulation is expected in applied H as well [12]. If so,

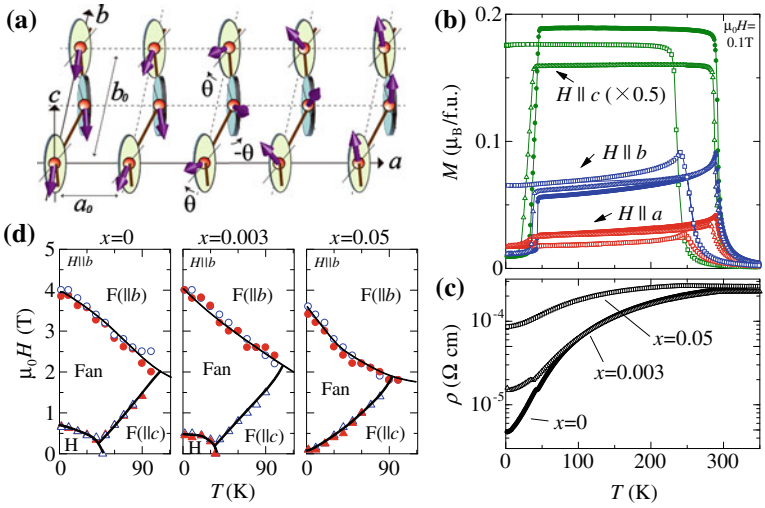

Fig. 5.7 **a** A schematic view of the helical spin structure of MnP in helimagnetic (H) state in zero field [19]. Temperature (T) dependence of (**b**) magnetization (M) at the magnetic field of $\mu_0 H = 0.1$ T along a, b, or c axis, and (**c**) resistivity (ρ) in zero field, for MnP ($x = 0$; *closed circles*), $Mn_{0.997}Co_{0.003}P$ ($x = 0.003$; *open triangles*), and $Mn_{0.95}Co_{0.05}P$ ($x = 0.05$; *open squares*) [19]. **d** Low-temperature magnetic-phase diagrams in $H||b$ for MnP, $Mn_{0.997}Co_{0.003}P$ ($x = 0.003$), and $Mn_{0.95}Co_{0.05}P$ ($x = 0.05$) [19]. *H*, *Fan*, and *F* indicate the helimagnetic, fan, and ferromagnetic phases, respectively. Phase boundaries [*closed* and *open circles* (*triangles*)] are determined by M-H and ρ-H measurements, respectively

it will affect the Hall effect through the scalar-spin-chirality mechanism, as argued below. Conversely, the Hall effect measurement in MnP gives useful information on its veiled magnetism, in addition to recent interest on the topological transport in helimagnets.

The single crystals of $Mn_{1-x}Co_xP$ ($x = 0$, 0.003, and 0.05) were grown by a Bridgman method. We show in Fig. 5.7b the temperature (T) dependence of the magnetization (M) for $Mn_{1-x}Co_xP$ in $\mu_0 H = 0.1$ T applied along the a, b, or c axis. The magnitude of M measured in H applied along each direction decreases in order of increasing magnetic anisotropy for all the samples; the a, b, and c axes are hard, intermediate, and easy axes of magnetization, respectively. For $x = 0$, two sharp transitions are observed at $T_C \approx 290$ K and $T_h \approx 45$ K. (To detect the subtle transition at $T^* \approx 282$ K, the applied field as small as 1–10 Oe is needed [11].) By doping a slight amount of Co ($x = 0.003$), both the transition temperatures become lowered by about 5 K. For the 5 % doped sample, the T_C decreases down to 240 K, and remarkably the helimagnetic transition is no longer observed. The longitudinal resistivity (ρ) in zero field for these samples is shown in Fig. 5.7c. While the magnetic anisotropy is strong, ρ is isotropic, being consistent with a former report [20]. ρ of $x = 0$ shows good metallicity ($d\rho/dT > 0$) below T_C; the residual ρ is as low as 5 μΩcm. An anomaly corresponding to the helimagnetic transition is observed at around 45 K. Also for $x = 0.003$, the similar T-dependence is observed, while the

residual ρ increases up to 20 $\mu\Omega$cm. For $x = 0.05$, ρ is of the order of 100 $\mu\Omega$cm with residual resistance ratio $\sim$3. The anomaly corresponding to the helimagnetic transition is no longer observed in $x = 0.05$, which is in accord with the result of M in $\mu_0 H = 0.1$ T (Fig. 5.7b), indicating the absence of the H phase as shown in Fig. 5.7d.

It has been known that there appear various magnetic phases depending on the H directions for MnP [21], although the possible slight spin-modulation by DM interaction in applied H is still elusive. We investigate the magnetic phase diagrams in $H||b$ for all the samples by measuring the H dependence of M and ρ (Fig. 5.7d). When H is applied along the b axis for MnP, Fan phase, in which the magnetic moments do not show a full rotation but oscillate like a *fan*, appears in the intermediate H region below about 100 K (Fig. 5.7d) [21, 22]. The period of fan structure for MnP determined by the neutron diffraction study is $18a_0$ at 77 K in 1 T [23], and varies with H and T [24]. By doping Co, the H phase region becomes narrower, while the size of Fan phase hardly changes. The magnetic transitions from H or F($||c$) to Fan phase are of the first order, while those from F($||c$) or Fan to F($||b$) ones are of the second order [21].

We show the H-dependence of the Hall conductivity (σ_H) under $H||b$ below 100 K for all the samples in Fig. 5.8. Corresponding to the magnetic transitions by H, σ_H

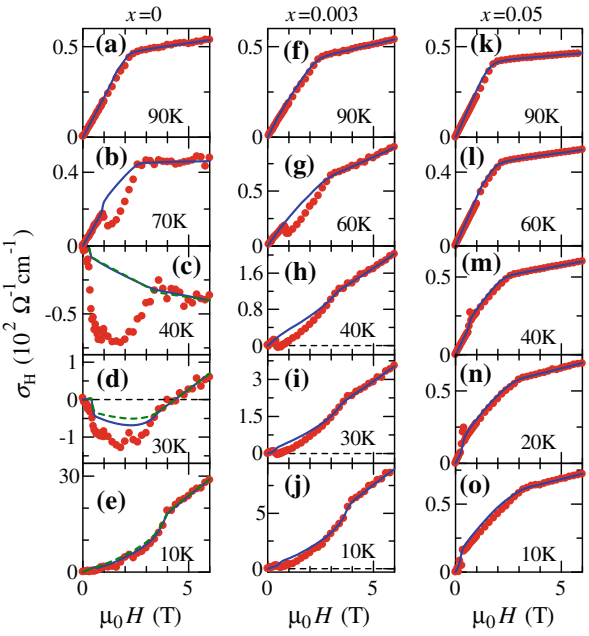

Fig. 5.8 Hall conductivity (σ_H, *dots*) as a function of magnetic field (H) applied along b axis for MnP ($x = 0$), $Mn_{0.997}Co_{0.003}P$ ($x = 0.003$), and $Mn_{0.95}Co_{0.05}P$ ($x = 0.05$) [19]. The *solid lines* are the fitted results assuming $\alpha = 0$ (intrinsic anomalous Hall effect). The *dashed lines* in (**c**)–(**e**) are the fitted results assuming $\alpha = 1$ (skew-scattering induced anomalous Hall effect)

shows nontrivial H-dependence; a dip is observed in Fan phase for $x = 0$ (Fig. 5.8b, c, d and e) and $x = 0.003$ (Fig. 5.8g, h, i and j). This unconventional behavior was missed in previous report [25] probably because of the smallness of the anomaly. As described in the introduction, the H dependence of σ_H is generally explained by the summation of the normal, anomalous, and topological Hall conductivities:

$$\sigma_H(H) = R_0\{\sigma(H)\}^2\mu_0 H + R_s\{\sigma(H)\}^{\alpha} M(H) + \sigma_H^T(H). \tag{5.7}$$

In Fig. 5.8, we estimate the conventional terms (normal plus anomalous Hall terms) by an empirical relation, Eq. (5.7) without the third term. The solid (blue) lines indicate the estimated conventional terms of σ_H assuming the Berry-phase-induced (intrinsic) anomalous Hall effect ($\alpha = 0$), which should be dominant in all-T region for $x = 0.003$ and $x = 0.05$, and in $T \geq 50\,\mathrm{K}$ for $x = 0$ [26]. For $x = 0$, below 50 K, where the resistivity is below $10\,\mu\Omega$cm, we also try to fit σ_H in terms of the skew scattering ($\alpha = 1$, green dashed lines) [26]. As shown in Fig. 5.8, however, the estimates with taking into account both intrinsic (Berry-phase) and extrinsic (skew-scattering) terms cannot explain the H-dependence of σ_H in Fan phase under the assumption of H-independent R_0 and R_s, while these conventional terms can satisfactorily fit the σ_H in the high-T region (Fig. 5.8a, f, and k). As the origin for this deviation from the fitted curves in Fan phase, one may consider possible change of the R_0 and R_s across the first-order transitions from H or F($||c$) to Fan phase. Judging from the well fitted σ_H by the conventional terms in both F($||c$) and F($||b$) phases with the same R_0 and R_s (Fig. 5.8b, g, and h), however, the values of R_0 and R_s are considered to unchange across the first-order transition. Therefore, we cannot explain the observed dip structure in Fan phase by conventional Hall terms, and we need another contribution with negative sign to Hall effect, which is assigned as the THE.

We estimate the possible topological Hall conductivity (σ_H^T) as the difference between the σ_H and the fitted curves, as shown in the form of a contour map for $x = 0$ and $x = 0.003$ (Fig. 5.9). Here, we simulate the conventional, i.e. non-THE, component with $\alpha = 1$ (skew scattering process) in the very low resistive ($\rho < 10\,\mu\Omega$cm) region of $T < 50\,\mathrm{K}$ for $x = 0$ and that with $\alpha = 0$ (intrinsic origin) in $T \geq 50\,\mathrm{K}$ for $x = 0$, while $\alpha = 0$ in all T-region for $x = 0.003$ and 0.05. The negative σ_H^T is observed in Fan and H phases for $x = 0$ (Fig. 5.9a). For $x = 0.003$, the negative σ_H^T is also observed in Fan phase, but its magnitude is smaller than for $x = 0$ (Fig. 5.9b). For $x = 0.05$, $|\sigma_H^T|$ is as small as $\sim 10\,\Omega^{-1}\mathrm{cm}^{-1}$ even at the lowest T (see Fig. 5.8o). In H phase of MnP, large σ_H^T might be merely an artifact because of very low ρ and ρ_H ($\leq 2\,n\Omega$cm); we will focus on σ_H^T in Fan phase hereafter. $|\sigma_H^T|$ decreases almost monotonically with increasing T or Co concentration. Thus, σ_H^T is observed in the state with noncollinear spin structure, and its magnitude decreases with the increase of scattering rate (τ^{-1}).

The Hall effect measurement strongly suggests the noncoplanar spin structure endowed with the scalar spin chirality in Fan phase, although there has been no report on the spin structure modulation by DM interaction in applied H. We illustrate in

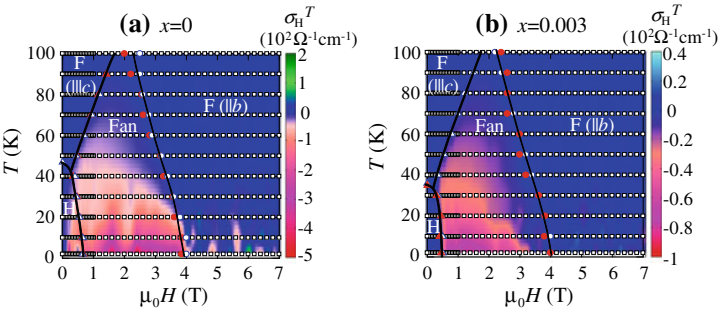

Fig. 5.9 Contour maps of the topological Hall conductivity (σ_H^T) measured in $H||b$ in the plane of T and $\mu_0 H$ for (**a**) MnP ($x = 0$) and (**b**) $Mn_{0.997}Co_{0.003}P$ ($x = 0.003$) [19]. *Open squares* indicate the measured points of Hall conductivity. For $x = 0$, the fitted *curves* with $\alpha = 0$ and $\alpha = 1$ were adopted in $T \geq 50\,\mathrm{K}$ and in $T \leq 40\,\mathrm{K}$, respectively. Abbreviations mean the same as those of Fig. 5.7d. Nonzero σ_H^T in the induced-ferromagnetic region especially at low Ts is not essential but merely an artifact; this is due to the error of estimation of ρ_H^T amplified via very low $\rho(<10\,\mu\Omega\mathrm{cm})$ in calculation of $\sigma_H^T = \rho_H^T/\rho^2$

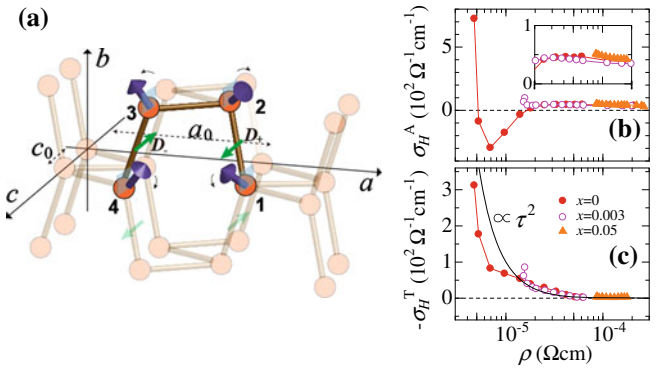

Fig. 5.10 **a** Schematic illustration of the noncoplanar spin structure expected in the presence of DM interaction [19]. Labels (1–4) indicate four Mn sites in a unit cell. The spin modulation by DM interaction [$\boldsymbol{D}_{\pm} = (0, 0, \pm D)$, *green arrows*] between the nearest-neighboring Mn-1 and Mn-2 sites and between the nearest-neighboring Mn-3 and Mn-4 ones is assumed. **b** Anomalous Hall conductivity (σ_H^A) at 7 T ($||b$) and **c** topological Hall conductivity (σ_H^T) at 1.4 T ($||b$) as a function of longitudinal resistivity ρ for $x = 0$ (*close circles*), $x = 0.003$ (*open circles*), and $x = 0.05$ (*closed triangles*) [19]. Inset to (**b**) shows the magnified view of σ_H^A in the region, $2 \times 10^{-5}\,\Omega\mathrm{cm} \leq \rho \leq 2 \times 10^{-4}\,\Omega\mathrm{cm}$

Fig. 5.10a the schematic view of the noncollinear spin structure, which is anticipated to be modulated by DM interaction. Here, the four Mn sites in a unit cell are labeled as Mn-1, Mn-2, Mn-3, and Mn-4 in Fig. 5.10a. Since the tilting toward the a axis by DM interaction is alternating along the both a and b axes, the directions of the spins on the four Mn sites in a unit cell are different from each other, and each three of them form noncoplanar structure. Owing to such a noncoplanar spin structure on these Mn

sites, the total scalar spin chirality should not vanish, and thus contribute to THE. Note that in H phase the existence of oppositely-oriented spins could cancel out the net scalar spin chirality. As described in the introduction, THE is characterized by the spin-chirality induced Berry phase in either $\boldsymbol{r}$- or $\boldsymbol{k}$-space [27]. We investigate the ρ ($\propto \tau^{-1}$) (at zero field) dependence of anomalous Hall conductivity σ_H^A at 7 T and σ_H^T at 1.4 T in $H||b$ in Fig. 5.10b, c, respectively. Below 10 μΩcm, σ_H^A shows complex behavior due to the skew-scattering [28], while it keeps an almost constant value $\sim$50 Ω^{-1}cm^{-1} above that (see the inset to Fig. 5.10b for magnification), as predicted for the intrinsic mechanism. This is the reason why we adopted $\alpha = 0$ and $\alpha = 1$ [see Eq. (1)] to correct the magnetoresistance effect, depending on the temperature region for $x = 0$. On the other hand, $-\sigma_H^T$ ($= |\sigma_H^T|$) for the three samples decreases almost in proportion to ρ^{-2} ($\propto\tau^2$) with increasing ρ, which verifies the validity of the $\boldsymbol{r}$-space picture of THE [27]. According to the theory of THE [27], the $\boldsymbol{r}$-space Berry phase should show primary contribution in $l \ll \lambda_S$. A former experiment of De Haas-van Alphen Effect in MnP [29] reported electron mass (m) and Fermi wavelength (k_F) in Fan phase: $m = 0.2m_0$ and $k_F = 1.0 \times 10^9$ m^{-1}, where m_0 is the free electron mass. The scattering relaxation time τ around the crossover from the intrinsic to extrinsic anomalous Hall effect ($\rho \sim 10\,\mu\Omega$ cm) is estimated as [30, 31] $\tau \approx \hbar/E_{\mathrm{SO}} \approx 2.2 \times 10^{-14}$ s, where $\hbar$ and E_{SO}($\approx$30 meV) are Dirac constant and energy scale of spin-orbit interaction, respectively. Then, we roughly estimate the mean free path $l = v_F\tau = (\hbar k_F/m)\tau$ as 127 Å for $x = 0$ at $\rho \sim 10\,\mu\Omega$cm. On the other hand, the period of fan structure for MnP is 12–15a_0 = 70–89 Å at 1.4 T according to the neutron diffraction measurement [24]. Therefore, l is almost comparable to λ_S around the intrinsic to extrinsic crossover of anomalous Hall effect ($\rho \sim 10\,\mu\Omega$ cm), and becomes well smaller than λ_S by doping Co, which certifies the $\boldsymbol{r}$-space picture of THE. From the fitted curves in Fig. 5.10c, the fictitious magnetic flux of THE at 1.4 T is estimated as $(\sigma_H^T/\rho^{-2})/R_0 \sim 0.5$–1 T, which is as small as that in the skyrmion phase of a long-period (180 Å) helimagnet MnSi [32]. At 3 T, the similar τ^2 dependence of σ_H^T is observed, and the fictitious flux at 3 T is half of that at 1.4 T (not shown). The small fictitious flux is consistent with the scalar spin chirality resulting from the slight spin modulation by DM interaction.

5.3 Topological Hall Effects Induced by Heat Current in a Chiral Helimagnet MnGe

As described in Chap. 1, Hall anomaly reminiscent of topological Hall effect has been observed in MnGe [33]. In this section, we investigate the topological Hall effects induced by heat current, i.e. topological thermal Hall effect and topological Nernst effect, for MnGe. We have succeeded in detecting the topological Hall term whose sign is negative also in thermal Hall and Nernst signals as observed in ρ_{yx}. We will discuss the nature of topological Hall effects driven by heat current.

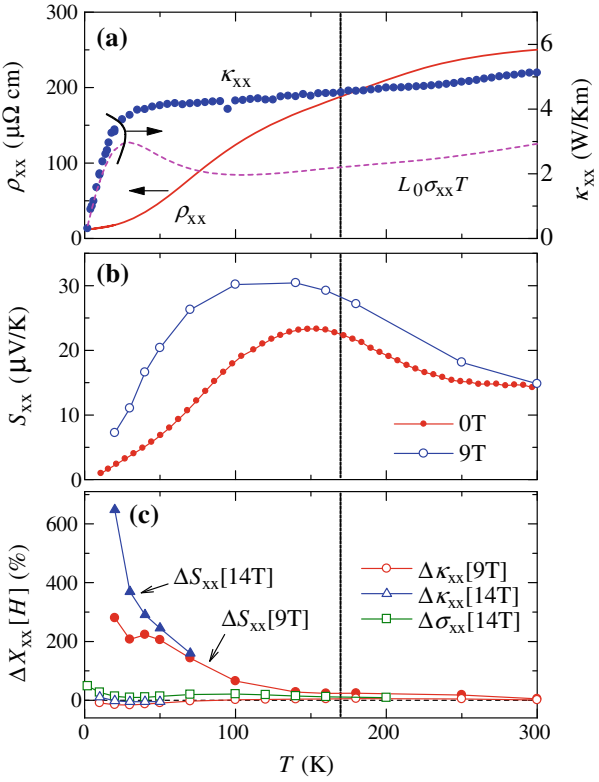

Fig. 5.11 **a** Temperature dependence of resistivity (ρ_{xx}, *solid line*) and thermal conductivity (κ_{xx}, *closed circles*). The electronic contribution to κ_{xx} is estimated by the Widemann-Franz law ($L_0\sigma_{xx}T$, *dashed line*). **b** Temperature dependence of Seebeck coefficient S_{xx} in zero field and 9 T. The data at 9 T is obtained from the H dependence of S_{xx} shown in Fig. 5.12a. **c** The magnitude of magnetic-field effect on X_{xx} (S_{xx}, κ_{xx}, or σ_{xx}), which is defined as $\Delta X_{xx}[H] \equiv X_{xx}[H]/X_{xx}[H=0]-1$. The T_N is ≈170 K [33]

Figure 5.11a shows the temperature (T) dependence of resistivity (ρ_{xx}) and longitudinal thermal conductivity (κ_{xx}) of MnGe. The resistivity exhibits metallic behavior with the residual resistance ratio $\rho_{xx}(300\,\mathrm{K})/\rho_{xx}(2\,\mathrm{K}) \approx 19$. Thermal conductivity decreases monotonically with decreasing temperature below 300 K. The magnitude of κ_{xx} at 300 K (∼5 W/Km) is almost comparable to that of the same $B20$-type CoGe [34]. The maximal value of electronic contribution to thermal conductivity is estimated by $L_0\sigma_{xx}T$ (the Wiedemann-Franz law) in the same figure; above 100 K, the electronic contribution is almost same in magnitude with the phonon one. Shown in Fig. 5.11b is the temperature dependence of Seebeck coefficient S_{xx} in zero field and at 9 T applied perpendicular to the plate-like sample (z-axis). S_{xx} in zero field is positive value in all the T region and shows a broad peak just below T_N. Under applied H, the peak shifts toward the lower-T region and its height dramatically becomes larger. We define the change of S_{xx}, κ_{xx}, or σ_{xx} by external H as

$\Delta X_{xx}[H] \equiv (X_{xx}[H] - X_{xx}[H=0])/X_{xx}[H=0]$, where X denotes S, κ. or σ. $\Delta S_{xx}[H]$ is over 200 % at 20 K in 9 T. such a large magnetic-field dependence is not observed in thermal or electrical conductivity (Fig. 5.11c); $\Delta\kappa_{xx}[9\,\mathrm{T}]$ and $\Delta\sigma_{xx}[9\,\mathrm{T}]$ are at most 16 % in all the T region. The enhancement of Seebeck coefficient by magnetic field could be explained by carrier-compensation effect. In Boltzmann transport theory, S_{xx} is expressed by the sum of electron (S_-) and hole (S_+) contribution:

$$S_{xx} = \frac{\sigma_+ S_+ + \sigma_- S_-}{\sigma_+ + \sigma_-} \tag{5.8}$$

$$S_\pm = \frac{\pi^2 k_B^2 T}{3e}\left[\frac{\partial \ln \sigma_\pm(\varepsilon)}{\partial \varepsilon}\right]_{\varepsilon=\mu}, \tag{5.9}$$

where μ is chemical potential and $\sigma_\pm$ is conductivity of electron or hole. The unusual enhancement of S_{xx} indicates that the energy-derivative term $[\partial \ln \sigma_\pm(\varepsilon)/\partial\varepsilon]_{\varepsilon=\mu}$ changes largely with external H. If the contribution from electrons and holes is almost same in magnitude, the Zeeman splitting of the band structure will largely affect S_{xx} value. Very small normal Hall coefficient in the helimagnetic region (Fig. 1.10a, b) is consistent with this scenario.

In Fig. 5.12, we show the H dependence of the Seebeck coefficient S_{xx} and Nernst signal defined as $e_N \equiv -E_y/\Delta_x T$. As discussed in Fig. 5.11b and c, the $\Delta S_{xx}[H]$ dramatically increases as T is decreased. With increasing H, S_{xx} shows a kink structure at the transition to the induced-ferromagnetic region. Also, an additional structure is observed around 6 T at 20 K. The magnetic field of this structure seems

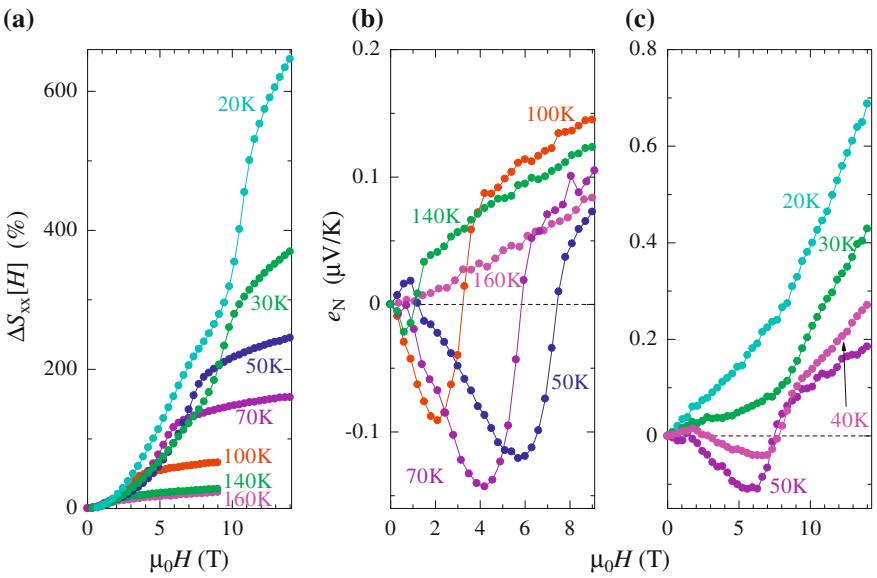

Fig. 5.12 Magnetic-field dependence of (**a**) ΔS_{xx} and (**b**), (**c**) Nersnt signal e_N below T_N

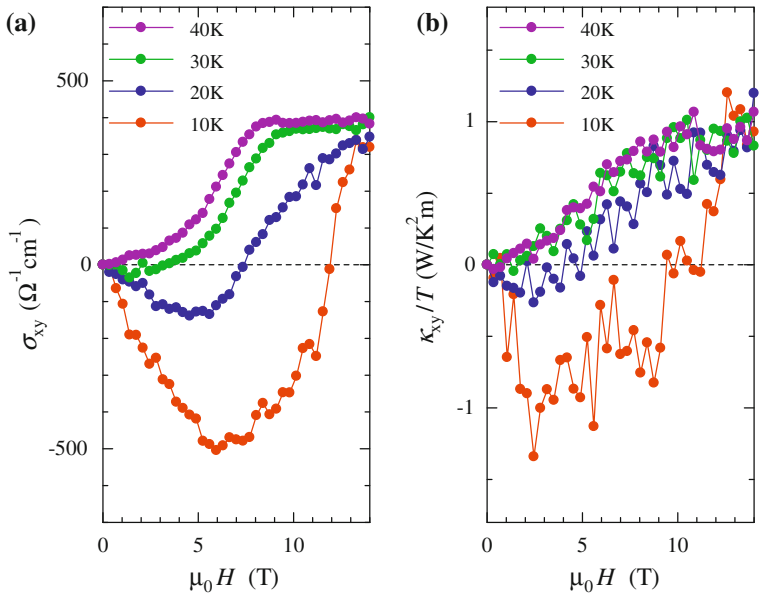

Fig. 5.13 Magnetic field dependence of (**a**) electrical Hall conductivity (σ_{xy}) and (**b**) thermal Hall conductivity divided by temperature (κ_{xy}/T) below 40 K

to correspond to that of the maximal $|\rho_{yx}^{T}|$ (see Fig. 1.10d). As to the Nernst signal e_N, the negative dip has been observed in wide T-range between 30 and 140 K (Fig. 5.12b, c). Since the H region in which the dip structure has been observed seems to correspond to the Skyrmion lattice phase suggested by the Hall effect measurement [33], the fictitious field by the scalar spin chirality of Skyrmion should cause the additional Nernst signal which has opposite sign to the conventional (normal and anomalous) terms. It is to be noted that the change in the electronic structure by magnetic field can not explain the sign change of e_N, since the electrons and holes should generate e_N of the same sign [35]. Since Nernst effect is not affected by the carrier-compensation effect, the conventional positive term tends to become large in the very low-T region below 20 K. One contrast feature of the topological Nernst effect with the topological (electrical) Hall effect is that the topological Hall contribution is discerned in a wider T-range in Nernst effect. In Hall resistivity (Fig. 1.10a, b, and d), the topological Hall term is discerned only below 70 K. By contrast, in Nernst effect, the topological Hall term is clearly discerned up to 140 K. This difference results from the different relative-proportion of the conventional Hall terms to the topological one. Another interesting point in Nernst signal is that a kink undiscerned in the Hall resistivity is observed around 2 T at 30, 40, and 50 K. This kink indicates some magnetic transition, which should be confirmed by neutron diffraction study in magnetic field.

In Fig. 5.13a, b, we show the H dependence of electrical Hall conductivity (σ_{xy}) and thermal Hall conductivity divided by temperature (κ_{xy}/T) below 40 K.

According to a former report [33], σ_{xy} is expressed as

$$\sigma_{xy} = \sigma_{xy}^{N} + \sigma_{xy}^{A} + \sigma_{xy}^{T} = R_0\sigma_{xx}^2(\mu_0 H) + R_s M + \rho_{yx}^{T}\sigma_{xx}^2, \tag{5.10}$$

where the first, second, and third terms are normal, anomalous, topological Hall conductivities. For σ_{xy}, in addition to the conventional Hall terms almost proportional to the magnetization, the negative topological Hall term is recognized below 40 K. Since σ_{xy}^{T} is propotional to $\sigma_{xx}^2 \propto \tau^2$, the magnitude of σ_{xy}^{T} increases with decreasing T. Also for thermal Hall conductivity, large negative topological Hall term is observed at 10 K. With increasing T, however, the topological Hall term seems to be suppressed more rapidly than in σ_{xy}. At 30 and 40 K, the H dependence of κ_{xy}/T seems to be almost proportional to that of magnetization. This rapid suppression of topological Hall term in κ_{xy}/T with increasing temperature is explained by the scattering-rate dependence of topological Hall conductivity. κ_{xy}^{T}/T should be linked with σ_{xy}^{T} through Lorenz ratio L_{xy}^{T}, i.e. $\kappa_{xy}^{T}/T = L_{xy}^{T}\sigma_{xy}^{T}$. As discussed in Chaps. 3 and 4, the thermal Hall conductivity decreases from Lorenz number (L_0) sensitively by the influence from inelastic scattering. Since $\sigma_{xy}^{T}(= \rho_{yx}^{T}\sigma_{xx}^{2} \propto \tau^2)$ is much affected by inelastic scattering in finite T, Lorenz ratio for the topological Hall conductivity decreases from L_0 with increasing T. Thus, κ_{xy}^{T} is suppressed dramatically with increasing T from the lowest T in contrast to topological Hall and Nernst effects.

We can obtain α_{xy} from the above data and show its H dependence in Fig. 5.14a, b. Using the Mott formula and the experimental relation $\sigma_{xy} = R_0\sigma_{xx}^2\mu_0 H + R_s M + \rho_{yx}^{T}\sigma_{xx}^2$ [33], α_{xy} is reduced to

$$\alpha_{xy} = \left\{ 2\sigma_{xx}\alpha_{xx}R_0 + \frac{\pi^2}{3}\frac{k_B^2 T}{e}\sigma_{xx}^2\left(\frac{\partial R_0}{\partial\varepsilon}\right)_{\varepsilon=\mu} \right\}\mu_0 H + \frac{\pi^2}{3}\frac{k_B^2 T}{e}\left(\frac{\partial R_s}{\partial\varepsilon}\right)_{\varepsilon=\mu} M + \alpha_{xy}^{T}. \tag{5.11}$$

The first term proportional to H ($\equiv \tilde{R}_0\mu_0 H$) is normal Nernst term and the second term ($\equiv \tilde{R}_s M$) is anomalous Nernst term which is proportional to M. Since the topological Nernst term does not exist above the saturation field of magnetization, we fit α_{xy} by the H-linear and M-linear conventional terms above the saturation field, as shown by solid lines in Fig. 5.14a, b. Here, the fitting parameters are $(\partial R_0/\partial\varepsilon)_{\varepsilon=\mu}$ and $(\partial R_s/\partial\varepsilon)_{\varepsilon=\mu}$ which are assumed to be constant with H. The deviation in the course of magnetization process is here assigned as α_{xy}^{T} and plotted in Fig. 5.14c. The magnitude of α_{xy}^{T} is almost constant between 20 and 50 K, while it decreases monotonically with increasing T above 70 K. Using the Mott formula, $\sigma_{xy}^{T} = \rho_{yx}^{T}\sigma_{xx}^{2}$, and $\rho_{yx}^{T} \approx R_0 B_{eff}$, α_{xy}^{T} is expressed as

$$\alpha_{xy}^{T} = \frac{\pi^2}{3}\frac{k_B^2 T}{e}\left(\frac{\partial\sigma_{xy}^{T}}{\partial\varepsilon}\right)_{\varepsilon=\mu} = 2S_{xx}\sigma_{xy}^{T} + \frac{\pi^2}{3}\frac{k_B^2 T}{e}\sigma_{xx}^{2}\left(\frac{\partial\rho_{yx}^{T}}{\partial\varepsilon}\right)_{\varepsilon=\mu} \approx \tilde{R}_0 B_{eff}. \tag{5.12}$$

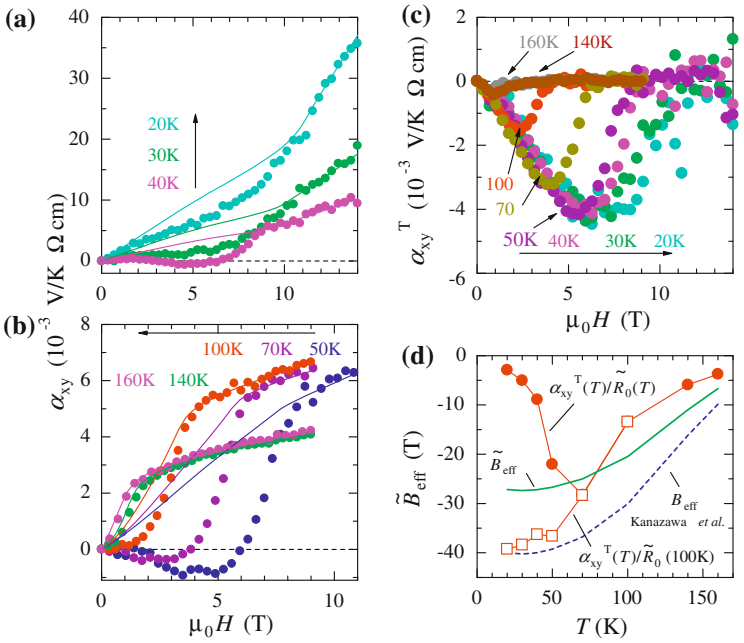

Fig. 5.14 **a**, **b** Magnetic-field dependence of α_{xy} below T_N. *Solid lines* indicate the fitted *curves* (see text). **c** Magnetic-field dependence of the estimated α_{xy}^{T}. **d** T dependence of the fictitious flux in topological Nernst effect ($\tilde{B}_{eff}$). *Closed circles* and *open squares* indicate $\alpha_{xy}^{T}(T)/\tilde{R}_0(T)$ and $\alpha_{xy}^{T}(T)/\tilde{R}_0(T = 100\,\mathrm{K})$, respectively. A *dotted line* indicates the fictitious flux (B_{eff}) estimated from the Hall effect measurement [33]. A *solid line* represents the T dependence of $\tilde{B}_{eff}$ approximated from $\alpha_{xy}^{T}(T)/\tilde{R}_0(T)$ and $\alpha_{xy}^{T}(T)/\tilde{R}_0(T = 100\,\mathrm{K})$

Thus, α_{xy}^{T} should be proportional to B_{eff} obtained from the Hall effect measurement. In Fig. 5.14d, we estimate the fictitious flux induced by scalar spin chirality in Nernst effect ($\tilde{B}_{eff}$) by $\alpha_{xy}^{T}/\tilde{R}_0$ as a function of T, where we use the maximal value of α_{xy}^{T} in its H dependence at each T (Fig. 5.14c). The magnitude of $\alpha_{xy}^{T}(T)/\tilde{R}_0(T)$ first increases with decreasing T from 160 K, but begins to decrease below 70 K (solid circles in Fig. 5.14d). The T dependence of B_{eff} is estimated from the former report on THE [33] as $B_{eff} = -40\,\mathrm{T} \times \{\lambda(T = 20\,\mathrm{K})/\lambda(T)\}^2$, as shown by a broken line in Fig. 5.14d. The magnitude and T profile are similar between $\alpha_{xy}^{T}(T)/\tilde{R}_0(T)$ and $B_{eff}(T)$ above 70 K, while the rapid suppression of $\alpha_{xy}^{T}(T)/\tilde{R}_0(T)$ below 70 K is apparently inconsistent with B_{eff}. This discrepancy should originate in the fitting process where we neglect the H dependence of $(\partial R_0/\partial\varepsilon)_{\varepsilon=\mu}$ and $(\partial R_s/\partial\varepsilon)_{\varepsilon=\mu}$, although large ΔS_{xx} in the low-T region indicates the H dependence of the energy derivative terms should be considered. Since the anomalous Nernst coefficient $\tilde{R}_s = (\pi^2/3)(k_B^2 T/e)(\partial R_s/\partial\varepsilon)_{\varepsilon=\mu}$ was assumed to be constant with H in the fitting process, the large H-dependence of α_{xy} below 50 K

has been all ascribed to $\tilde{R}_0$; $\tilde{R}_0$ should be overestimated. By contrast, if we neglect the T dependence of $\tilde{R}_0$ and if we assume $\tilde{R}_0(T) = \tilde{R}_0(100\,\mathrm{K})$ below 100 K, we can evaluate the upper limit of $|\tilde{B}_{eff}|$ by $\alpha_{xy}^T/\tilde{R}_0(100\,\mathrm{T})$ below 70 K (open squares in Fig. 5.14d). From $\alpha_{xy}^T/\tilde{R}_0(T)$ and $\alpha_{xy}^T/\tilde{R}_0(100\,\mathrm{K})$, $\tilde{B}_{eff}$ whose T dependence is similar with that of B_{eff} in all the T region can be reproduced as shown by a dotted line in Fig. 5.14d. The obtained $\tilde{B}_{eff}$ at 20 K is ~ -27 T which is slightly smaller in magnitude than $B_{eff} \approx -40$ T in THE [33]. These results indicate that the Mott formula is applicable to the topological Nernst effect on Skyrmion lattice and well explains the overall T profile of α_{xy}^T.

5.4 Summary

The major results in this chapter are summarized as follows:

- We have found THE in $Fe_{1.3}Sb$ and MnP. The THE originates from the scalar spin chirality due to the modulation of spin structure by DM interaction.
- For $Fe_{1.3}Sb$, in the relatively-high-T region of the 120° spin ordered structure on the triangular lattice, the Hall resistivity is negative in sign and well described as composed of the conventional normal and anomalous components. In the low-T region below 30 K, however, the significant positive contribution is observed to be added to the Hall resistivity. This novel term is explained in terms of the scalar spin chirality which originates from the spin modulation by DM interaction in the spin heptamer clusters formed around the respective Fe(i) sites.
- For MnP and Co-doped MnP, we have observed the topological Hall effect in Fan phase under $H||b$. The topological Hall conductivity decays in proportion to τ^2 when Co is doped, which is consistent with the $\boldsymbol{r}$-space picture on THE. The fictitious flux is estimated to be $\sim$1 T, suggesting that the THE is caused by scalar spin chirality originating from the slight modulation of spin structures by (local) DM interaction.
- We have investigated the topological Hall effects by heat current, i.e. topological thermal Hall effect and topological Nernst effect, for MnGe. The topological thermal Hall conductivity of MnGe is rapidly suppressed with increasing temperature due to the effect from inelastic scattering. By contrast, in the transverse Pertier conductivity, which is obtained from the measurements of electrical and thermal Hall and Nernst effects, topological contribution has been observed in the wide temperature range ($20 \leq T \leq 140$ K). The T dependence of this topological Pertier conductivity seems to follow the Mott formula, and the fictitious flux at the lowest T is estimated to be -27 T whose magnitude is almost comparable to that in topological Hall effect.

References

1. Y. Akagi, Y. Motome, J. Phys. Soc. Jpn. **79**, 083701 (2010)
2. I. Martin, C.D. Batista, Phys. Rev. Lett. **101**, 156402 (2008)
3. H. Takatsu, S. Yonezawa, S. Fujimoto, Y. Maeno, Phys. Rev. Lett. **105**, 137201 (2010)
4. Y. Shiomi, M. Mochizuki, Y. Kaneko, Y. Tokura, Phys. Rev. Lett. **108**, 056601 (2012)
5. R. Kumar, K.S. Harchand, M. Vishwamittar, K. Chandra, P. Jernberg, T. Ericsson, R. Wäppling, Phys. Rev. B **32**, 69 (1985)
6. T. Yashiro, Y. Yamaguchi, S. Tomiyoshi, N. Kazama, H. Watanabe, J. Phys. Soc. Jpn. **34**, 58 (1973)
7. P. Amornpitoksuk, D. Ravot, A. Mauger, J.C. Tedenac, Phys. Rev. B **77**, 144405 (2008)
8. P.J. Picone, P.E. Clark, J. Magn. Magn. Mater. **25**, 140 (1981)
9. Y. Taguchi, Y. Oohara, H. Yoshizawa, N. Nagaosa, Y. Tokura, Science **291**, 2573 (2001)
10. E.E. Huber Jr, D.H. Ridgley, Phys. Rev. **135**, A1033 (1964)
11. C.C. Becerra, J. Phys.: Condens. Matter **12**, 5889 (2000)
12. T. Yamazaki, Y. Tabata, T. Waki, T.J. Sato, M. Matsuura, K. Ohoyama, M. Yokoyama, H. Nakamura, arXiv:1106.4599 (2011)
13. G. Felcher, J. Appl. Phys. **37**, 1056 (1966)
14. J. Forsyth, S. Pickart, P. Brown, Proc. Phys. Soc. **88**, 333 (1966)
15. R.M. Moon, J. Appl. Phys. **53**, 1956 (1982)
16. E.E. Rodriguez, C. Stock, K.L. Krycka, C.F. Majkrzak, P. Zajdel, K. Kirshenbaum, N.P. Butch, S.R. Saha, J. Paglione, M.A. Green, Phys. Rev. B **83**, 134438 (2011)
17. T. Koyama, S. Yano, Y. Togawa, Y. Kousaka, S. Mori, K. Inoue, J. Kishine, J. Akimitsu, J. Phys. Soc. Jpn. **81**, 043701 (2012)
18. S. Rundqvist, Acta Chem. Scand. **16**, 287 (1962)
19. Y. Shiomi, S. Iguchi, Y. Tokura, Phys. Rev. B **86**, 180404(R) (2012)
20. T. Suzuki, J. Phys. Soc. Jpn. **25**, 646 (1968)
21. A. Zięba, C.C. Bacerra, H. Fjellvåg, N.F. Oliveira Jr, A. Kjekshus, Phys. Rev. B **46**, 3380 (1992)
22. T. Komatsubara, T. Suzuki, E. Hirahara, J. Phys. Soc. Jpn. **28**, 317 (1970)
23. Y. Ishikawa, T. Komatsubara, E. Hirahara, Phys. Rev. Lett. **23**, 532 (1969)
24. H. Obara, Y. Endo, Y. Ishikawa, T. Komatsubara, J. Phys. Soc. Jpn. **49**, 928 (1980)
25. S. Chikazuki, *Jiseitai Handbook* (Asakura Shoten, Tokyo, 1975). (in Japanese)
26. T. Miyasato, N. Abe, T. Fujii, A. Asamitsu, S. Onoda, Y. Onose, N. Nagaosa, Y. Tokura, Phys. Rev. Lett. **99**, 086602 (2007)
27. M. Onoda, G. Tatara, N. Nagaosa, J. Phys. Soc. Jpn. **73**, 2624 (2004)
28. Y. Shiomi, Y. Onose, Y. Tokura, Phys. Rev. B **79**, 100404(R) (2009)
29. M. Ohbayashi, T. Komatsubara, E. Hirahara, J. Phys. Soc. Jpn. **40**, 1088 (1976)
30. S. Onoda, N. Sugimoto, N. Nagaosa, Phys. Rev. Lett. **97**, 126602 (2006)
31. S. Onoda, N. Sugimoto, N. Nagaosa, Phys. Rev. B **77**, 165103 (2008)
32. A. Neubauer, C. Pfleiderer, B. Binz, A. Rosch, R. Ritz, P.G. Niklowitz, P. Böni, Phys. Rev. Lett. **102**, 186602 (2009)
33. N. Kanazawa, Y. Onose, T. Arima, D. Okuyama, K. Ohoyama, S. Wakimoto, K. Kakurai, S. Ishiwata, Y. Tokura, Phys. Rev. Lett. **106**, 156603 (2011)
34. N. Kanazawa, Y. Onose, Y. Shiomi, S. Ishiwata, Y. Tokura, Appl. Phys. Lett. **100**, 093902 (2012)
35. R. Bel, K. Behnia, H. Berger, Phys. Rev. Lett. **91**, 066602 (2003)

Chapter 6
Conclusion

Abstract We have investigated anomalous Hall effect in itinerant ferromagents (pure Fe, Co, and Ni and impurity-doped ones) and topological Hall effect in itinerant helimagnets ($Fe_{1+\delta}$ Sb, MnP, and MnGe) by means of Hall effect, Nernst effect, and thermal Hall effect measurements. Here, we again summarize the major results and comment on their importance.

Keywords Anomalous Hall effect · Topological Hall effect · Berry phase of electrons · Skew-scattering mechanism · Scalar spin chirality

6.1 Anomalous Hall Effect in Itinerant Ferromagents (Chaps. 3 and 4)

- We have investigated the inelastic-scattering dependence of the anomalous Hall current in terms of the Lorenz ratio both in the region where the intrinsic mechanism ($\sigma_{xy}^{A} \propto \tau^{0}$) is dominant (Sects. 3.1 and 3.2) and in the region where the skew-scattering mechanism ($\sigma_{xy}^{A} \propto \tau^{1}$) is dominant (Sect. 4.1).
- The Hall Lorenz ratio for the anomalous component L_{xy}^{A} almost coincides with the free-electron Lorenz number L_0 at the lowest temperature. This confirms the validity of Wiedemann-Franz law for the anomalous Hall current as well.
- The Lorenz ratio for the intrinsic anomalous Hall current L_{xy}^{A} coincides with L_0 when ρ_{xx} is smaller than 3-6 $\times 10^{-6}$ Ωcm. This is an indication of scattering-free nature of Berry-phase-induced intrinsic anomalus Hall effect. When ρ_{xx} exceeds the value of 3-6 $\times 10^{-6}$ Ωcm, by contrast, L_{xy}^{A} decreases and deviates from L_0. The value of ρ_{xx} at the crossover corresponds to $\hbar/\tau \sim 20$ meV, which is comparable to the expected magnitude of the energy gap around the band anticrossing point formed by the spin-orbit interaction.
- In the region where the anomalous Hall effect induced by skew-scattering is dominant, the Lorenz ratio for anomalous Hall current is much smaller than L_0.

Y. Shiomi, *Anomalous and Topological Hall Effects in Itinerant Magnets*,
Springer Theses, DOI: 10.1007/978-4-431-54361-9_6, © Springer Japan 2013

This feature evidences the emergence of the dissipative Hall current induced by the skew scattering in addition to the persistent dissipationless intrinsic anomalous Hall current. For Si0.3 %-doped Fe, around the temperature of intrinsic-extrinsic crossover, the Lorenz ratio for anomalous Hall current shows unusual behavior, i.e. negative value or divergence, due to the competition between intrinsic and extrinsic (skew-scattering-induced) anomalous Hall currents.

- For Fe doped with a 3*d*-transition metal close to Fe, the resonant skew scattering mechanism shows large anomalous Hall effect in the low-T region below 100 K, while it is not feasible for Si-, Ge-, or Sn-doped Fe. For Si-, Ge-, or Sn-doped Fe, the skew-scattering-induced anomalous Hall resistivity seems to depend on residual resistivity instead of total resistivity. The origin of the strong temperature variation of the resonant skew scattering contribution is a future problem.

These results have a significant meaning for the long-standing controversy on the origin of anomalous Hall effect as well as for the future application of dissipationless current in spintronics devices. Since skew scattering mechanism generates larger magnitude of spin current than the intrinsic one, the deep understanding of skew scattering mechanism should be useful in the research field of spintronics. Application of thermal Hall effect measurement to the study of anomalous Hall effect is a distinguished feature of our study. After these results, we have also succeeded in observing magnon Hall effect by means of thermal Hall effect in ferromagnetic insulators [1, 2]. These results have made an impact in "spin caloritronics" [3] (the research on phenomena associated with the coupling between spin and heat currents), which is now a hot topic in the field of spintronics.

6.2 Topological Hall Effect in Itinerant Helimagents (Chap. 5)

- We have found topological Hall effect in $Fe_{1.3}Sb$ and MnP. For these materials, the spin-structure modulation by DM interaction is a key for the nonzero value of net scalar spin chirality.
- For $Fe_{1.3}Sb$, in the low-T region below 30 K, the significant positive contribution of topological Hall effect is observed to be added to the Hall resistivity. The scalar spin chirality originates from the spin modulation by DM interaction in the spin heptamer clusters formed around the respective Fe(i) sites.
- For MnP and Co-doped MnP, we have observed the topological Hall effect in the fan phase under $H||b$. The nonzero scalar spin chirality originates from the slight modulation of fan-like spin structure by DM interaction. The decrease in the magnitude of topological Hall conductivity as observed by doping Co is well explained in terms of the topological Hall effect arising from the spin-chirality induced Berry phase in real space.
- We have investigated the topological Hall effects by heat current, i.e. topological thermal Hall effect and topological Nernst effect, for MnGe. Since the topological Hall current is much affected by inelastic scattering, the topological thermal Hall

conductivity is rapidly suppressed with increasing temperature. By contrast, in the transverse Pertier conductivity which is obtained from the measurements of Hall, thermal Hall, and Nernst effects, topological Hall contribution is observed in the wide temperature range ($20\ \mathrm{K} \leq T \leq 140\ \mathrm{K}$). The topological Nernst effect seems to follow the Mott formula, and the fictitious flux at the lowest T is estimtated to be -27 T, which is of almost similar magnitude to that in electrical Hall effect.

The topological Hall effect mediated by DM interaction as proposed here is a new mechanism, and it is expected to appear in many other helimagnets. Discovery of new materials which show topological Hall effect should contribute to a better understanding of transport phenomena linked with spin chirality. In the latter part of Chap. 5, we have investigated the topological Hall effects induced by heat current in the Skyrmion lattice phase of MnGe. A future theoretical study will more clarify the different nature between electrical and heat-current-induced topological Hall effects.

References

1. Y. Onose, T. Ideue, H. Katsura, Y. Shiomi, N. Nagaosa, Y. Tokura, Science **329**, 297 (2010)
2. T. Ideue, Y. Onose, H. Katsura, Y. Shiomi, S. Ishiwat, N. Nagaosa, Y. Tokura, Phys. Rev. B **85**, 134411 (2012)
3. G.E.W. Bauer, E. Saitoh, B.J. van Wees, Nat. Mat. **11**, 391–399 (2012)